Spectroscopic Characterization of Stationary Inverted Lyman Populations and Free-Free and Bound-Free Emission of Lower-Energy State Hydride Ion Formed by a Catalytic Reaction of Atomic Hydrogen and Certain Group I Catalysts

R. Mills*, P. C. Ray, R. M. Mayo

BlackLight Power, Inc.

493 Old Trenton Road

Cranbury, NJ 08512

ABSTRACT

Rb^+ to Rb^{2+} and $2K^+$ to $K + K^{2+}$ each provide a reaction with a net enthalpy equal to the potential energy of atomic hydrogen. The presence of these gaseous ions with thermally dissociated hydrogen formed a plasma having strong VUV emission with a stationary inverted Lyman population. Significant Balmer α line broadening of 18 and 12 eV was observed from a rt-plasma of hydrogen with KNO_3, and $RbNO_3$, respectively, compared to $3\,eV$ from a hydrogen microwave plasma. We propose an energetic catalytic reaction involving a resonance energy transfer between hydrogen atoms and Rb^+ or $2K^+$ to form a very stable novel hydride ion. Its predicted binding energy of $3.0468\,eV$ with the fine structure was observed at 4071 Å, and its predicted bound-free hyperfine structure lines $E_{HF} = j^2 3.00213 \times 10^{-5} + 3.0563\,eV$ (j is an integer) matched those observed for $j = 1$ to $j = 37$ to within a 1 part per 10^4. Characteristic emission from each catalyst was observed. This catalytic reaction may pump a cw HI laser.

Key Words: inverted H population, cw HI laser, fast H, H catalysis, novel hydride ion

* Phone: 609-490-1090; Fax: 609-490-1066; E-mail: rmills@blacklightpower.com

1. Introduction

The Lyman α, β, and γ lines of atomic hydrogen at $121.6\,nm$, $102.6\,nm$, and $97.3\,nm$ in the vacuum ultraviolet (VUV) region are due to the transitions from $n = 2$, $n = 3$, and $n = 4$ to $n = 1$, respectively. These lines are of great importance in many applications ranging from photochemistry, to laboratory simulations of planetary atmospheres, to astrophysics and plasma physics. In plasma physics, the Lyman series line intensities and their ratios are frequently used in the determination of plasma parameters such as hydrogen number densities and other quantities such as particle fluxes or ion recombination processes [1-2]. For the last four decades, scientist from academia and industry have been searching for lasers using hydrogen plasma [3-6]. Developed sources that provide a usefully intense hydrogen plasma are high powered lasers, arcs and high voltage DC and RF discharges, synchrotron devices, inductively coupled plasma generators, and magnetically confined plasmas. However, the generation of population inversion is very difficult. Recombining expanding plasmas jets formed by methods such as arcs or pulsed discharges is considered one of the most promising methods of realizing an HI laser.

It was reported previously that a new plasma source has been developed that operates by incandescently heating a hydrogen dissociator to provide atomic hydrogen and heats a catalyst such that it becomes gaseous and reacts with the atomic hydrogen to produce a plasma called a resonance transfer or rt-plasma. It was extraordinary, that intense VUV emission was observed at low temperatures (e.g. $\approx 10^3\,K$) and an extraordinary low field strength of about 1-2 V/cm from atomic hydrogen and certain atomized elements or certain gaseous ions which singly or multiply ionize at integer multiples of the potential energy of atomic hydrogen, $27.2\,eV$ [7-8].

The theory of the chemically generated or assisted plasma source was given previously [7-11] and is based on applying Maxwell's equations to the Schrödinger equation. The familiar Rydberg equation (Eq. (1)) arises for the hydrogen excited states for $n > 1$ of Eq. (2).

$$E_n = -\frac{e^2}{n^2 8\pi\varepsilon_o a_H} = -\frac{13.598\ eV}{n^2} \tag{1}$$

2

$$n = 1,2,3,... \tag{2}$$

An additional result is that atomic hydrogen may undergo a catalytic reaction with certain atoms and ions which singly or multiply ionize at integer multiples of the potential energy of atomic hydrogen, $m \cdot 27.2 \, eV$ wherein m is an integer. The reaction involves a nonradiative energy transfer to form a hydrogen atom that is lower in energy than unreacted atomic hydrogen that corresponds to a fractional principal quantum number. That is

$$n = \frac{1}{2}, \frac{1}{3}, \frac{1}{4}, ..., \frac{1}{p}; \quad p \text{ is an integer} \tag{3}$$

replaces the well known parameter n = integer in the Rydberg equation for hydrogen excited states. The $n = 1$ state of hydrogen and the $n = \dfrac{1}{\text{integer}}$ states of hydrogen are nonradiative, but a transition between two nonradiative states, say $n = 1$ to $n = 1/2$, is possible via a nonradiative energy transfer. Thus, a catalyst provides a net positive enthalpy of reaction of $m \cdot 27.2 \, eV$ (i.e. it resonantly accepts the nonradiative energy transfer from hydrogen atoms and releases the energy to the surroundings to affect electronic transitions to fractional quantum energy levels). As a consequence of the nonradiative energy transfer, the hydrogen atom becomes unstable and emits further energy until it achieves a lower-energy nonradiative state having a principal energy level given by Eqs. (1) and (3). Processes such as hydrogen molecular bond formation that occur without photons and that require collisions are common [12]. Also, some commercial phosphors are based on resonant nonradiative energy transfer involving multipole coupling [13].

A catalytic system involves helium ions because the second ionization energy of helium is $54.417 \, eV$, which is equivalent to $2 \cdot 27.2 \, eV$. In this case, $54.417 \, eV$ is transferred nonradiatively from atomic hydrogen to He^+ which is resonantly ionized. It was reported that vacuum ultraviolet (VUV) spectroscopy was recorded on microwave discharges of helium with 2% hydrogen. Novel emission lines were observed with energies of $q \cdot 13.6 \, eV$ where $q = 1,2,3,4,6,7,8,9,11$ or these lines inelastically scattered by helium wherein $21.2 \, eV$ was absorbed in the excitation of $He \, (1s^2)$ to $He \, (1s^1 2p^1)$ [14-16].

The Group I and as well as Group VIII elements are unique in that,

with the exception of krypton and xenon, atoms and or ions from these groups provide a reaction with a net enthalpy that is a close match to an integer multiple of the potential energy of atomic hydrogen, $m \cdot 27.2 \, eV$ where m is an integer and the reaction involves the ionization of ≤ 3 electrons. The corresponding reactions of Group I elements with a net enthalpy of $m \cdot 27.2 \, eV$ which are proposed to form an rt-plasma follow:

The first and second ionization energies of lithium are $5.39172 \, eV$ and $75.6402 \, eV$, respectively [17]. The double ionization reaction of Li to Li^{2+}, then, has a net enthalpy of reaction of $81.032 \, eV$, which is equivalent to $m = 3$.

The second, third, and fourth ionization energies of sodium are $47.2864 \, eV$, $71.6200 \, eV$, and $98.91 \, eV$, respectively [17]. The triple ionization reaction of Na^+ to Na^{4+}, then, has a net enthalpy of reaction of $217.8164 \, eV$, which is equivalent to $m = 8$.

The second ionization energy of potassium is $31.63 \, eV$, and K^+ releases $4.34 \, eV$ when it is reduced to K [17]. The combination of reactions K^+ to K^{2+} and K^+ to K, then, has a net enthalpy of reaction of $27.28 \, eV$, which is equivalent to $m = 1$. Also, the first, second, and third ionization energies of potassium are $4.34066 \, eV$, $31.63 \, eV$, and $45.806 \, eV$, respectively [17]. The triple ionization reaction of K to K^{3+}, then, has a net enthalpy of reaction of $81.7766 \, eV$, which is equivalent to $m = 3$.

The second ionization energy of rubidium is $27.28 \, eV$ [17]; thus, the reaction Rb^+ to Rb^{2+} has a net enthalpy of reaction of $27.28 \, eV$, which is equivalent to $m = 1$.

The first and second ionization energies of cesium are $3.89390 \, eV$ and $23.15745 \, eV$, respectively [17]. The double ionization reaction of Cs to Cs^{2+}, then, has a net enthalpy of reaction of $27.05135 \, eV$, which is equivalent to $m = 1$.

In this paper, we report the observation of rt-plasmas with the combination of hydrogen and certain gaseous ions which singly or multiply ionize at integer multiples of the potential energy of atomic hydrogen, $27.2 \, eV$; whereas controls of hydrogen, the test materials alone, and control materials which can not provide a reaction with a net enthalpy of $27.2 \, eV$ did not form a plasma. The plasma emission was characterized by VUV spectroscopy, high resolution visible spectroscopy, the measurement of the energetic hydrogen atom densities and energies

from the absolute intensity and width of the Balmer α line, and measurement of the electron temperature T_e using a Langmuir probe. T_e was also measured from intensity ratios of alkali lines. Intense hydrogen Lyman emission was observed, highly energetic hydrogen atoms, and a novel series of spectral lines were observed from the rt-plasmas. The plasma observations could not be explained by known mechanisms, and the novel spectral lines could not be assigned to known species present in the cell or contaminants. However, the data is explained by a catalytic reaction of atomic hydrogen to form a more stable hydride ion designated $H^-(1/2)$.

2. Experimental

V.UV spectra, 6563 Å Balmer α line width measurements, and high resolution visible spectra were recorded on light emitted from rt-plasmas of hydrogen with KNO_3, $RbNO_3$, and $CsNO_3$. High resolution visible spectra were also recorded on the cell emission with $LiNO_3$ and $NaNO_3$ replacing KNO_3, $RbNO_3$, and $CsNO_3$. The former nitrates served as controls since each generates an rt-plasma but is not predicted to form $H^-(1/2)$ [7]. In addition, $Al(NO_3)_3$ and $Mg(NO_3)_2$ served as noncatalyst controls [7]. The experimental set up shown in Figure 1 comprised a quartz cell which was 500 mm in length and 50 mm in diameter. A VUV spectrometer which was differentially pumped recorded Lyman series emission and characteristic emission from catalyst ions that indicated the presence of an rt-plasma. The entire quartz cell was enclosed in an Alumina insulation package. Several K-type thermocouples were located in the insulation that were monitored with a multichannel computer data acquisition system. A Pyrex cap sealed to the quartz cell with a Viton O ring and a C-clamp incorporated ports for gas inlet, outlet, and photon detection. A tungsten filament (0.508 mm in diameter and 800 cm in length, total resistance ~2.5 ohm) heater and hydrogen dissociator were in the quartz tube as well as a cylindrical titanium screen (300 mm long and 40 mm in diameter) that served as a second hydrogen dissociator. The filament was coiled on a grooved ceramic tube support to maintain its shape when heated. The return lead passed through the inside of the ceramic tube.

The nitrate test materials were coated on a titanium screen dissociator by the method of wet impregnation. The screen was coated by dipping it in a 0.6 M MNO_3/10% H_2O_2 (M was K, Rb, Cs, Li, or Na), 0.6 M $Mg(NO_3)_2$/10% H_2O_2, or 0.6 M $Al(NO_3)_3$/10% H_2O_2 aqueous solution, and about 0.1 g of the crystalline material was dried on the surface by heating for 12 hours in a drying oven at 130 °C. A new dissociator was used for each experiment.

The titanium screen was electrically floated with power applied to the filament. In each test, power was applied to the filament by a DC power supply which was controlled by a constant power controller. The power applied to the filament was 300 W. The voltage across the filament was about 40 V and the current was about 6.25 A at 250 W. The temperature of the tungsten filament was estimated to be in the range 1200 to 1500 °C with an optical pyrometer and independently based on its electrical resistance. The external cell wall temperature was about 700 °C.

The rt-plasma phenomena was also studied for cesium metal with hydrogen versus additional controls. The quartz cell was operated under the same conditions as for the Group I nitrates with 1.) hydrogen, argon, neon, and helium alone; 2.) sodium, magnesium, barium, and cesium metals alone, and 3.) sodium, magnesium, barium, and cesium with hydrogen. The pure elements of sodium, magnesium, barium, and cesium were placed in the bottom of the cell and vaporized by filament heating.

The cell was then operated under gas flow conditions while maintaining a constant gas pressure in the cell. As part of the preparation procedure, the cell was maintained at 50 °C for four hours with helium flowing at 30 sccm at a pressure of 0.1 Torr. The cell was then operated with an ultrapure hydrogen flow rate of 5.5 sccm maintained at 300 mTorr controlled by a mass flow controller and the spectra were recorded. In addition, spectra were obtained with hydrogen alone and on the test materials alone with the cell under vacuum rather than with flowing hydrogen.

The light emission was introduced to an VUV spectrometer for spectral measurement in the short wavelength region using a windowless configuration. The spectrometer was a McPherson 0.2 meter monochromator (Model 302, Seya-Namioka type) equipped with a 1200

lines/mm holographic grating with a platinum coating. The wavelength region covered by the monochromator was $50-5600$ Å. A channel electron multiplier (CEM) was used to detect the VUV light. The wavelength resolution was about 2 Å (FWHM) with an entrance and exit slit width of $10\,\mu m$. The vacuum inside the monochromator was maintained below $5\,X\,10^{-4}$ Torr by a turbo pump. The Lyman α emission was recorded as a function of time after the filament was turned on. In each case, the VUV spectrum ($900-1300$ Å) of the rt-plasma cell emission was recorded at about the point of the maximum Lyman α emission to confirm the rt-plasma before the line broadening and the high resolution visible spectrum were recorded. The VUV control spectra were also recorded on light emitted from hydrogen glow discharge and hydrogen and nitrogen microwave discharge plasmas maintained according to methods reported previously [14] at an input power of 200 W and 100 W, respectively.

The spectrometer was calibrated between 400-2000 Å with a standard discharge light source using He, Ne, Ar, Kr, and Xe lines: He I (584 Å), He II (304 Å), Ne I (735 Å), Ne II (460.7 Å), Ar I (1048 Å), Ar II (932 Å), Kr II (964 Å), Xe I (1295.6 Å), Xe II (1041.3 Å), Xe II (1100.43 Å). The wavelength and intensity ratios matched those given by NIST [18]. The spectrometer response was determined to be approximately flat in the 1000-1300 Å region. The calculation of the number density of the $n=2$, 3, and 4 states was corrected for the minor variation of the sensitivity with wavelength in this region.

In addition, regions of the VUV, ultraviolet (UV) and visible (VIS) spectra ($400-5600$ Å) were recorded with the normal incidence VUV spectrometer using a PMT and a sodium salicylate scintillator to record emission from the atoms and ions of rt-plasma catalysts. The emission was compared with a standard VUV emission spectrum that was obtained with a gas discharge cell comprised a five-way stainless steel cross that served as the anode with a hollow stainless steel cathode that was coated with KNO_3, $RbNO_3$, or $CsNO_3$ by the same procedure used to coat the titanium dissociator. The five-way cross was pressurized with 1 torr of hydrogen to initiate the discharge. The hydrogen was then evacuated so that only catalyst lines were observed. The DC voltage at the time the spectra were recorded was 300 V.

7

The light was also introduced into a visible spectrometer to record in this wavelength region. The width of the 6563 Å Balmer α line and a high resolution visible spectrum (3990 - 4100 Å) were recorded on light emitted from each of the control hydrogen glow discharge and microwave discharge plasmas [14, 19] and each rt-plasma maintained in the filament heated cell. The plasma emission was fiber-optically coupled through a 220F matching fiber adapter positioned 2 cm from the cell wall to a high resolution visible spectrometer with a resolution of ±0.06 Å over the spectral range 1900 - 8600 Å. The spectrometer was a Jobin Yvon Horiba 1250 M with 2400 groves/mm ion-etched holographic diffraction grating. The entrance and exit slits were set to 20 μm. The spectrometer was scanned between 6555 - 6570 Å using a 0.1 Å step size. The signal was recorded by a PMT with a stand alone high voltage power supply (950 V) and an acquisition controller. The data was obtained in a single accumulation with a 1 second integration time. High resolution visible spectra (3825 - 4200 Å) were also recorded on light emitted from air and nitrogen microwave plasmas maintained according to methods reported previously [14] at 300 mTorr with a gas flow rate of 5.5 sccm controlled by a mass flow controller and an input power of 100 W. As further controls, high resolution visible spectra (3890 - 4060 Å) were recorded on KNO_3 and $RbNO_3$ rt-plasmas of air-hydrogen (10-30/90-70%) mixtures.

The light was recorded in air, and the data is presented in air wavelengths. To calibrate the wavelengths and to measure the absolute intensity, the high resolution visible spectrometer and detection system were calibrated [20] with 6965.4 Å, 5460.8 Å, 5799.6 Å, 4358.4 Å, 4077.8 Å, 4046.6 Å, and 3650.1 Å light from a Hg-Ar lamp (Ocean Optics, model HG-1) that was calibrated with a NIST certified silicon photodiode. The intensity was determined to be essentially flat over the region of interest 3825-7000 Å. The population density of the n=3 hydrogen excited state N_3 was determined from the absolute intensity of the Balmer α (6562.8 Å) line measured using the calibrated spectrometer. The absolute intensities of Balmer β, γ, and δ were determined from the absolute intensity of Balmer α and the relative intensity ratios. Other reference peaks in the spectra such as the K I peaks at 4044.142 Å and 4047.213 Å and $N_2^+ \, B^2\Sigma_u^+ - X^2\Sigma_u^+ \, (\upsilon' = 0 - \upsilon'' = 0)$, $N_2 \, C^3\Pi_u - B^3\Pi_g \, (\upsilon' = 2 - \upsilon'' = 5)$, $N_2 \, C^3\Pi_u - B^3\Pi_g \, (\upsilon' = 1 - \upsilon'' = 4)$, $N_2 \, C^3\Pi_u - B^3\Pi_g \, (\upsilon' = 0 - \upsilon'' = 3)$, and

N_2 $(C^3\Pi_u - B^3\Pi_g$ $(\upsilon' = 4 - \upsilon'' = 8)$ band heads at 3914.4, 3943.0, 3998.4, 4059.4 Å and 4094.8 verified the calibration. Since the spectra were obtained in air, the reference peaks from the literature were air wavelengths. Theoretical vacuum wavelengths were converted to air wavelength after Linde [21].

The electron density and temperature T_e of the rt-plasma was determined using a Langmuir probe according to the method given previously [22]. T_e of the $RbNO_3$ and KNO_3 cells were also measured from the ratio of the intensity of the Rb^+ 741.4Å line to that of the Rb^{2+} 815.3Å line and the ratio of the K^+ 612.6 Å line to that of the K^{2+} 546.1 Å line, respectively, as described by Griem [23].

3. Results and discussion

A. Measurement of hydrogen atom temperature and number density from Balmer line broadening

No plasma and no emission except blackbody radiation at long wavelengths was observed for 1.) hydrogen, argon, neon, and helium alone; 2.) sodium, magnesium, barium, and cesium metals alone, and 3.) sodium, magnesium, and barium, with hydrogen; whereas, a plasma with VUV emission was observed from incandescently heated hydrogen and each of KNO_3, $RbNO_3$, $CsNO_3$, $LiNO_3$ and $NaNO_3$. No conventional mechanism can explain the formation of a plasma by incandescently heating hydrogen gas with the presence of trace amounts of these of inorganic compounds as discussed previously [24]. No emission was observed from hydrogen alone or each test material alone. No plasma formed with incandescently heated hydrogen and each of $Al(NO_3)_3$ and $Mg(NO_3)_2$.

The method of Videnovic et al. [25] was used to calculate the energetic hydrogen atom densities and energies from the width of the 6563 Å Balmer α line emitted from microwave and rt-plasmas. The full half-width $\Delta\lambda_G$ of each Gaussian results from the Doppler ($\Delta\lambda_D$) and instrumental ($\Delta\lambda_I$) half-widths:

$$\Delta\lambda_G = \sqrt{\Delta\lambda_D^2 + \Delta\lambda_I^2} \qquad (5)$$

$\Delta\lambda_I$ in our experiments was 0.06 Å. The temperature was calculated from

9

the Doppler half-width using the formula:

$$\Delta \lambda_D = 7.16 \, X \, 10^{-6} \lambda_0 \left(\frac{T}{\mu} \right)^{1/2} \quad (\text{Å})$$

(6)

where λ_0 is the line wavelength in Å, T is the temperature in K ($1 \, eV = 11,605 \, K$), and μ is the molecular weight ($=1$ for hydrogen). In each case, the average Doppler half-width that was not appreciably changed with pressure varied by $\pm 5\%$ corresponding to an error in the energy of $\pm 5\%$. The corresponding number densities varied by $\pm 20\%$ depending on the pressure.

The results of the 6563 Å Balmer α line width measured with the high resolution (± 0.06 Å) visible spectrometer on light emitted from rt-plasmas of hydrogen with KNO_3, $RbNO_3$, and $CsNO_3$ are shown in Figures 2-4, respectively. Significant line broadening of 18, 12, and 12 eV and atom densities of $4 \, X \, 10^{11}$, $6 \, X \, 10^{11}$, and $4 \, X \, 10^{11}$ atoms/cm^3 were observed from a rt-plasma of hydrogen with KNO_3, $RbNO_3$, and $CsNO_3$, respectively, as shown in Table 1. A hydrogen microwave plasma maintained at the same total pressure showed no excessive broadening corresponding to an average hydrogen atom temperature of $\approx 3 \, eV$ and a density of $2 \, X \, 10^{11}$ atoms/cm^3. The line broadening results could not be explained by Stark or thermal broadening or electric field acceleration of charged species since the electron density was low, the gas temperature was about 700 °C, and the measured field of the incandescent heater was extremely weak, 1 V/cm, corresponding to a broadening of much less than 1 eV. We propose that the Doppler broadening was caused by the energetic reaction which formed the rt-plasma.

Prior studies that reported fast H attributed the observation to acceleration of ions in a high electric fields at the cathode fall region and an external field Stark effect [25-28]. The authors have reported observations with a microwave plasma having no high field present [19, 29]. Microwave helium-hydrogen and argon-hydrogen plasmas showed extraordinary broadening corresponding to an average hydrogen atom temperature of 180-210 eV and 110-130 eV, respectively. Whereas, pure hydrogen and xenon-hydrogen microwave plasmas showed no excessive broadening corresponding to an average hydrogen atom temperature of $\approx 4 \, eV$ [19].

No hydrogen species, H^+, H_2^+, H_3^+, H^-, H, or H_2, responds to the

10

microwave field; rather, only the electrons respond. But, the measured electron temperature in the argon-hydrogen microwave plasmas was about 1 eV; whereas, the measured neutral hydrogen temperature was 110-130 eV [19, 29]. This requires that $T_i >>> T_e$. This result can not be explained by electric field acceleration of charged species. In microwave driven plasmas, there is no high electric field in a cathode fall region ($> 1kV/cm$) to accelerate positive ions as proposed previously [25-28] to explain significant broadening in hydrogen containing plasmas driven at a high voltage electrodes. It is impossible for H or any H-containing ion which may give rise to H to have a higher temperature than the electrons in a microwave plasma. The microwave field couples to electrons, not ions. And, the H atom temperature can not be attributed to the mechanisms proposed previously [25-28]. In fact, in the argon microwave case, the argon atoms and ions would have the highest energies since they have the largest cross section for electron collisions. No broadening of argon lines is observed. Only the hydrogen lines are broadened. The observation of excessive Balmer line broadening in a microwave driven plasma requires a source of free energy. Sources other than that provided by the electric field or known chemical reactions must be considered. We propose that the source is the energy released by the reaction which formed the rt-plasma.

We have assumed that Doppler broadening due to thermal motion was the dominant source in rt-plasmas to the extent that other sources may be neglected. To confirm this assumption, each source is now considered. In general, the experimental profile is a convolution of two Doppler profiles, an instrumental profile, the natural (lifetime) profile, Stark profiles, van der Waal's profiles, a resonance profile, and fine structure. The instrumental half-width is measured to be ±0.06 Å. The natural half-width of the Balmer α line given by Djurovic and Roberts [28] is 1.4×10^{-3} Å which is negligible. The fine structure splitting is also negligible.

Stark broadening of hydrogen lines in plasmas can not be measured at low electron densities using conventional emission or absorption spectroscopy because it is hidden by Doppler broadening. In the case of the Lyman α line, the Stark width exceeds the Doppler width only at $n_e > 10^{17} cm^{-3}$ for temperatures of about 10^4 K [30].

11

The relationship between the Stark broadening $\Delta\lambda_s$ of the Balmer β line in nm, the electron density n_e in m^{-3}, and the electron temperature T_e in K is

$$\log n_e = C_0 + C_1 \log(\Delta\lambda_s) + C_2 [\log(\Delta\lambda_s)]^2 + C_3 \log(T_e) \tag{7}$$

where $C_0 = 22.578$, $C_1 = 1.478$, $C_2 = -0.144$, and $C_3 = 0.1265$ [31]. From Eq. (7), to get a Stark broadening of only 1 Å with $T_e = 9000\,K$, an electron density of about $n_e \sim 3\,X10^{15}\,cm^{-3}$ is required compared to that of the rt-plasma of $n_e = 2\,X10^9\,cm^{-3}$ determined using a Langmuir probe as shown in Figure 5, over six orders of magnitude less. In fact, the charged species requirement was greater than the total gas concentration. Gigosos and Cardenoso [32] give the observed Balmer α Stark broadening for plasmas of hydrogen with helium or argon as a function of the electron temperature and density. For example, the Stark broadening of the Balmer α line recorded on a $H + He^+$ plasma is only 0.33 Å with $T_e = 20,000\,K$ and $n_e = 1.4\,X10^{14}\,cm^{-3}$. Thus, the Stark broadening was also insignificant.

The statistical curve fit of the $RbNO_3$ rt-plasma and hydrogen microwave plasma emission are shown in Figure 3. In each case, the data matched a Gaussian profile having the X^2 and R^2 values given in Figure 3. The absence of Stark broadening in the $RbNO_3$ rt-plasma is also evident by the good fit to a Gaussian profile rather than a Voigt profile as shown in Figure 3.

A linear Stark effect arises from an applied electric field that splits the energy level with principal quantum number n into $(2n-1)$ equidistant sublevels. The magnitude of this effect given by Videnovic et al. [25] is about $2\,X10^{-1}$ Å $/kV \cdot cm^{-1}$. The applied electric field was present in our study was extremely weak, 1 V/cm; thus, the linear Stark effect should be negligible.

To investigate whether the rt-plasmas of this study were optically thin or thick at a given frequency ω, the effective path length $\tau_\omega(L)$ was calculated from

$$\tau_\omega(L) = \kappa_\omega L \tag{8}$$

where L is the path length and κ_ω is the absorption coefficient given by

$$\kappa_\omega = \sigma_\omega\,X\,N_H \tag{9}$$

where σ_ω is the absorption cross section and N_H is the number density of the absorber. For optically thin plasmas $\tau_\omega(L) < 1$, and for optically thick

12

plasmas $\tau_\omega(L) > 1$. The absorption cross section for Balmer α emission is $\sigma = 1 \times 10^{-15} \, cm^2$ [33]. As discussed *infra.*, an estimate of the n=2 H atom density based on Lyman line intensity is $\sim 1 \times 10^8 \, cm^{-3}$. Thus, for a plasma length of 50 cm, $\tau_\omega(50 \, cm)$ for Balmer α is

$$\tau_\omega(50 \, cm) = \kappa_\omega L = \left(1 \times 10^{-15} \, cm^2\right)\left(1 \times 10^8 \, cm^{-3}\right)\left(50 \, cm\right) = 5 \times 10^{-7} \qquad (10)$$

Since $\tau_\omega(50) <<< 1$, the rt-plasmas were optically thin; so, the self absorption of 6563 Å emission by n=2 state atomic hydrogen may be neglected as a source of the observed broadening.

As discussed above, an estimate based on emission line profiles places the total H atom density of the rt-hydrogen plasma at $\sim 5 \times 10^{11} \, cm^{-3}$. Since this is overwhelmingly dominated by the ground state, $N_H = 5 \times 10^{11} \, cm^{-3}$ will be used. Usually, the atomic hydrogen collisional cross section in plasmas is on the order of $10^{-18} \, cm^2$ [34]. Thus, for $N_H = 5 \times 10^{11} \, cm^{-3}$, collisional or pressure broadening is negligible.

Since the line broadening was measured with sufficient resolution (± 0.06 Å) to clearly separate the RbII and KII peaks at 6555 Å and 6595 Å, respectively, from the 6563 Å Balmer α line, the possibility of a contribution of the alkali ion lines to the hydrogen line broadening was eliminated.

B. rt-plasma catalyst emission

The VUV spectrum (450 – 800 Å) of the emission of the KNO_3- H_2 gas cell is shown in Figure 6. The lines of K^+, K^{2+}, and K^{3+} corresponding to the two possible catalytic reactions were observed as reported previously [35] with the assignments confirmed by a standard potassium plasma spectrum and NIST tables [18, 36]. Line emission corresponding to K^{3+} was observed at 650-670 Å and 740-760 Å. K^{2+} was observed at 510 Å and 550 Å, and K^+ was observed at 620 Å. A large K^{3+} peak was also observed at 892 Å. K was observed at 3447 Å, 4965 Å, and 5084 Å.

The VUV spectrum (500 – 900 Å) of the emission of the $RbNO_3$- H_2 gas cell (top curve) and the standard rubidium discharge plasma (bottom curve) are shown in Figure 7. The standard rubidium discharge spectrum according to Sec. 2 is exemplary of the light source used to confirm the line assignments of each of the Group I nitrates studied. Line emission

corresponding to Rb^{2+} was observed at 815.9 Å, 591 Å, 581 Å, 556 Å, and 533 Å. Rb^+ was observed at 741.5 Å, 711 Å, 697 Å, and 643.8 Å. The assignments of the Rb^{2+} and Rb^+ lines were confirmed by the NIST tables [36].

The UV spectrum (3400 – 4150 Å) of the emission of the $CsNO_3$-H_2 gas cell is shown in Figure 8. Line emission corresponding to Cs^{2+} was observed at 3477 Å, 3618 Å, and 4001 Å. Cs^+ was observed at 3680 Å, 3806 Å, and 4069 Å. Cs was observed at 3888 Å. The assignments of the Cs^{2+}, Cs^+, and Cs lines were confirmed by a standard cesium plasma spectrum and the NIST tables [18].

A bright plasma with strong VUV emission was observed in the case of cesium metal with flowing hydrogen. The VUV spectrum (400 – 800 Å) of the emission of the $CsNO_3$-H_2 gas cell is shown in Figure 9. Line emission corresponding to the second ionization energy of cesium, 23.15745 eV [17], for the decay transition Cs^{2+} to Cs^+ was observed at 533 Å. (The 533 Å emission shown in Figure 9 is actually significantly larger than shown due to the low grating efficiency at the short wavelengths.) The only cesium lines observed for the standard cesium microwave plasma were in the visible region, and no lines were observed at wavelengths shorter than 800 Å in the case of the standard hydrogen microwave plasma.

The resonance lines of Cs II were observed with a sliding spark on the 10.7 m normal incidence vacuum spectrometer at the National Bureau of Standards (NBS) [37] as given in Table 2. The 533 Å emission of the hydrogen catalysis reaction with cesium shown in Figure 9 is dramatically different from the NBS standard cesium spectrum wherein a series of lines of Cs^+ was observed that vanished at the limit of the ionization energy of Cs^+ to Cs^{2+}. In fact, the ionization limit was not observed; rather, it was derived by NBS to be 23.17(4) eV [37]. Furthermore, I. S. Aleksakhin et al. recorded the emission of cesium in the 450-750 Å region during electron-atom collisions [38]. The ionization energy limit at 533 Å was not observed by I. S. Aleksakhin et al. either.

Atomic hydrogen may resonantly transfer energy to cesium to cause its double ionization to Cs^{2+}. Considering broadening by the thermal energies, the net enthalpy may be 27.2 eV, a match with the potential energy of atomic hydrogen; thus, it forms an rt-plasma. Cs^{2+}

14

may then decay and emit the radiation. The vacuum reaction is

$$Cs^{2+} + e^- \rightarrow Cs^+ + 23.2\ eV \tag{11}$$

Following the resonant transfer, the decay energy for the transition Cs^{2+} to Cs^+ is predicted to give $23.2\ eV$ (533 Å) line emission corresponding to the second ionization energy of cesium, $23.15745\ eV$. This line emission was observed as shown in Figure 9 without the Rydberg series of lines of Cs^+ as observed by NBS with a sliding spark method [37] as shown in Table 2. The observed Cs^{2+} single line emission at 533 Å supports the resonant energy transfer of $27.2\ eV$ from atomic hydrogen to atomic cesium to form an rt-plasma.

C. Hydrogen Lyman and Balmer series emission

The VUV spectra (900 – 1300 Å) of the cell emission recorded at about the point of the maximum Lyman α emission from the KNO_3, $RbNO_3$, and $CsNO_3$ gas cells are shown in Figures 10-12, respectively, with the superimposed spectrum from the hydrogen microwave plasma. Strong Lyman series VUV emission was observed with KNO_3, $RbNO_3$, or $CsNO_3$ (or cesium metal) and hydrogen. The $CsNO_3$ emission was similar to that of the hydrogen microwave plasma; whereas, the Lyman series lines of the KNO_3 and $RbNO_3$ rt-plasmas showed population inversion with much greater intensity of atomic hydrogen versus molecular hydrogen compared to the microwave plasma emission. The population inversion was also consistent with the relative Balmer α, β, γ, and δ line intensities. The relative intensities of the corresponding emission from the n=3, n=4, n=5, and n=6 state to the n=2 state recorded on a hydrogen microwave plasma, a KNO_3 rt-plasma, and a $RbNO_3$ rt-plasma are shown in Figure 13, 14, and 15, respectively.

The Lyman population density of the excited hydrogen atoms N_α, N_β, and N_γ with principal quantum numbers $n = 2, 3,$ and 4, respectively, were obtained from their intensity integrated over the spectral peaks corrected by their Einstein coefficients. The population ratios, $\dfrac{N_\beta}{N_\alpha}$ and $\dfrac{N_\gamma}{N_\alpha}$, for pure H_2 and H_2 with KNO_3 or $RbNO_3$ are given in Table 3.

The important parameter for a lasing medium is the reduced

15

population density $\dfrac{N}{g}$ given by the population density N divided by the statistical weight g as discussed by Akatsuka et al. [6]. The ratio of $\dfrac{N}{g}$ for L_β to L_α and L_γ to L_α given in Table 4 demonstrate that with appropriate cavity length and mirror reflection coefficient cw laser oscillations may be obtained between $n=3$ and $n=2$ since the corresponding $\dfrac{N_\beta\, g_\alpha}{N_\alpha\, g_\beta} > 1$ [6].

Lasing further requires an overpopulation which may be determined from the absolute intensity of the Balmer α line.

From the population ratios, $\dfrac{N_\beta}{N_\alpha}$ ($\dfrac{N_3}{N_2}$) and $\dfrac{N_\gamma}{N_\alpha}$ ($\dfrac{N_4}{N_2}$), shown in Table 3, the corresponding $\dfrac{N_4}{N_3}$ was determined to be 0.78, 0.74, and 0.29 for the hydrogen microwave plasma, KNO_3 rt-plasma, and $RbNO_3$ rt-plasma, respectively. Whereas, from the Balmer line intensities, $\dfrac{N_4}{N_3}$ was determined to be 0.78, 0.76, and 0.29 for the hydrogen microwave plasma, KNO_3 rt-plasma, and $RbNO_3$ rt-plasma, respectively. Since $\dfrac{N_4}{N_3}$ determined from the Lyman series and the Balmer series was the same, and the Balmer α line was absolutely measured, the absolute reduced number densities for n=2 to n=6 were determined from the absolute Balmer α line intensity (i. e. using the experimental $N_3 \sim 1.25 \, X\, 10^8 \, cm^{-3}$) and the relative ratio of the Lyman and Balmer series lines). A plot of the absolute reduced population density $\dfrac{N_n}{g_n}$ versus quantum number n recorded on a hydrogen microwave plasma, a KNO_3 rt-plasma, and a $RbNO_3$ rt-plasma is shown in Figure 16. An inverted population was only observed for n=3 in the case of KNO_3 and $RbNO_3$ rt-plasmas.

For the plasma conditions of this experiment ($T_e \approx 0.7-0.8\,eV$, $n_e \approx 10^9\,cm^{-3}$), a threshold reduced overpopulation of $4.4\,X\,10^6\,cm^{-3}$ is required for lasing assuming a cavity length of 100 cm and a mirror reflection coefficient of 0.99. Modeling results based on the collisional-radiative model [6] given in Sec. 3D show that the threshold condition is achievable for these plasmas.

Other explanations of the over population were ruled out. The

spectrometer response was determined to be approximately flat in the 1000-1300 Å region. To investigate whether the rt-plasmas of this study were optically thin or thick at 1216 Å, the effective path length $\tau_\omega(50\,cm)$ was calculated from Eq. (10) using the absorption cross section for Lyman α emission, $\sigma = 4\,X\,10^{-16}\,cm^2$ [33], and $N_H = 5\,X\,10^{11}\,cm^{-3}$.

$$\tau_\omega(50\,cm) = \kappa_\omega L = \left(4\,X\,10^{-16}\,cm^2\right)\left(5\,X\,10^{11}\,cm^{-3}\right)(50\,cm) = 1\,X\,10^{-2} \qquad (12)$$

Since $\tau_\omega(50) <<< 1$, the rt-plasmas were optically thin; so, the self absorption of 1216 Å emission by n=1 state atomic hydrogen may be neglected as the cause of the inverted ratio. Furthermore, the L_α / L_β intensity ratios of the control hydrogen plasmas closely matched the NIST intensity ratio using the NIST Einstein A coefficients [18]. Since the hydrogen pressure was the same in the rt-plasmas and the control hydrogen plasma, the same Einstein A coefficients were used to calculate the number density ratio in both cases.

In a non-recombining plasma [6], thermal electron collisional mechanisms can not produce the conditions necessary for population inversion. The highly ionized alkali ions observed in the plasma may ionize atomic hydrogen which may recombine in an excited state; yet, no such reaction has ever been observed which gives rise to an inverted Lyman population. Neither electrical ionization nor chemical ionization is known to form an inverted Lyman population. All known sources of excitation were exhausted [24]. The observation, then, of population inversion indicates the presence of free energy in the system. This is further evidence that a new chemical source of energy, greater than 12 eV/atom was present as is the observation of ions such as K^{3+} which requires an energy source of at least $81.7766\,eV$. The only possibility known to the authors is the proposed rt-plasma reaction [7].

T_e was determined to be $0.84\,eV$ and $0.76\,eV$ for the K^+ and Rb^+ rt-plasma respectively. Similarly, $k_B T_e = (0.30 - 0.43)\,eV$ was determined for a K^+ rt-plasma as reported by Conrads et al. [24] with the assumption of a Maxwell Boltzmann distribution of the level population, and a slightly higher temperature of $k_B T_e = (0.32 - 0.48)\,eV$ was found when a corona model was applied. The data indicated that the electron temperature was not higher than $k_B T_e = 0.5\,eV$. On this basis, it was astonishing that a strong Lyman beta transition appeared in the spectra since an excitation energy of $12.1\,eV$ is required. This energy is a factor of about 25 above the

measured thermal energy. The amount of electrons in the Maxwell tail that had enough energy to enhance the Lyman transition was 11 orders of magnitude lower than the total number of electrons. Longer range fields (of the order of mm) were only about a 1 V/cm. In addition to electron collisional excitation, known chemical reactions, resonant photon transfer, and multiphoton absorption, and the lowering of the ionization and excitation energies by the state of "non ideality" in dense plasmas were also rejected as the source of ionization or excitation to form the hydrogen plasma.

A source of energy other than that provided by the electric field or known chemical reactions must be considered. We propose that the plasma formed chemically rather than electrically and that the product of the energetic chemical reaction of atomic hydrogen with potassium or rubidium ions which serve as catalysts as well as reactants are compounds having novel hydride ions reported previously [39] and in Sec. 3E. Prior related studies that support the possibility of a novel reaction of atomic hydrogen which produces a chemically generated or assisted plasma (rt-plasma) and produces novel hydride compounds include VUV spectroscopy [7,8, 14-16, 19, 24, 29, 35, 39, 40-45], characteristic emission from catalysts and the hydride ion products [35, 39, 41, 42], lower-energy hydrogen emission [14-16, 40, 43], chemically formed plasmas [7, 8, 24, 35, 39, 41, 42, 45], Balmer α line broadening [8, 15, 16, 19, 29, 39, 43, 44], population inversion of H lines [44], elevated electron temperature [15, 19, 29, 39, 43], anomalous plasma afterglow duration [45], power generation [8, 15, 16, 29, 43], and analysis of novel chemical compounds [46, 47].

The predicted catalyst ion emission was observed from rt-plasmas as presented in Sec. 3B. For example, characteristic emission was observed from K^{2+} as well as K^{3+} which confirmed the resonant energy transfer of $27.2\,eV$ and $3 \cdot 27.2\,eV$, respectively, from atomic hydrogen to the catalyst K^+ / K^- and K, respectively. With a highly conductive plasma, the voltage of the cell was about 20 V, and the field strength was about 1-2 V/cm which was too low to ionize potassium to K^{3+} which requires at least $81.7766\,eV$. Similarly, the ionization of K^+ to K^{2+} requires $31.63\,eV$ which could not have been due to the weak electric field. Known chemical reactions are also of too low an energy by at least an order of

magnitude to form K^{2+} and K^{3+}. The K^{3+} lines generated in the incandescently heated cell and due to the catalyst reaction of atomic hydrogen were confirmed by a high voltage discharge and NIST tables [18, 36].

The energy of the catalysis reaction may be transferred nonradiatively to hydrogen which serves as a third body to form fast $H(n = 1)$ atoms. Then the inverted population is explained by a collisional excitation of fast H. The emission of $H(n = 3)$ from fast $H(n = 1)$ atoms excited by collisions with the background H_2 has been discussed by Radovanov et al. [48]. Formation of H^+ is also predicted which is far from thermal equilibrium in terms of the hydrogen atom temperature as discussed in Sec. 3A and modeled in Sec. 3D. Akatsuka et al. [6] show that it is characteristic of cold recombining plasmas to have the high lying levels in local thermodynamic equilibrium (LTE); whereas, for the low lying levels, population inversion is obtained when T_e becomes low with an appropriate electron density as shown by the Saha-Boltzmann equation.

D. Level Population Model and Lasing Ability

In order to estimate hydrogen excited state level populations and assess lasing ability, the collisional radiative model [6, 49] is applied to the plasma conditions obtained herein ($T_e \sim 0.8\,eV$, $n_e \sim 10^9\,cm^{-3}$). The collisional radiative model explicitly includes all level population and de-population mechanisms for each excited level from every other excited level in the hydrogen atom. Excited level n is, then, populated by collisional excitation from all lower excited states, and collisional and radiative de-excitation from all higher excited states. De-population explicitly includes collisional and radiative de-excitation to all lower states, and collisional excitation to all higher levels. Independent ionization loss, radiative recombination, and dielectronic recombination are included for all levels as well. A separate balance equation is prescribed for each individual level and is coupled to all other level equations through the population and de-population terms described above.

In order to close the set of equations, truncation was chosen at n=5.

This is justified by both the experimental observation of very low measurable emission from higher lying states and *a posteriori* via the model results indicating a progression of negligibly smaller level densities beyond n=3. The ground state (n=1) level population cannot be determined by this method since the important affects of dissociation, molecular recombination, and transport are not included. As discussed earlier (Sec. 3A), however, an estimate based on emission line profiles places the total H atom density $\sim 5 \times 10^{11} \, cm^{-3}$. Since this is overwhelmingly dominated by the ground state, the assignment $N_1 = 5 \times 10^{11} \, cm^{-3}$ will be made throughout.

Solution to the n=2 − 5 level equations under these conditions shows no inversion in any of the level populations. This is an expected result for a steady, thermal plasma. Also, as expected, the dominant mechanisms are found to be population by collisional excitation and de-population by radiative decay.

The results of this calculation ($N_{2-5} < 10^4 \, cm^{-3}$) are inconsistent with the spectroscopic observations. Absolutely calibrating the monochromator near H_α however yields, $N_3 \sim 1.25 \times 10^8 \, cm^{-3}$. There is, then, a heretofore undetermined mechanism providing direct excited state population, *i.e.* pumping. To help quantify the affects of this mechanism, the level equations are once again evaluated with N_3 fixed to $1.25 \times 10^8 \, cm^{-3}$ and the inclusion of an independent pumping rate. Since spectroscopic results indicate n=3 − 2 inversion, pumping is prescribed to the n=3 state from the ground state, n=1. The results from this calculation for n=1 − 5 are summarized in Table 5.

Now collisional mechanisms from the n=3 state as well as ground state collisional excitation and radiative decay significantly contribute to population and de-population rates. In addition, a demonstrated inversion in the population between the n=3 and 2 states is predicted. The reduced overpopulation density for this case is $\Delta(N/g) \sim 4.7 \times 10^6 \, cm^{-3}$, slightly above the threshold of $4.4 \times 10^6 \, cm^{-3}$. The pumping rate is also determined in this analysis yielding a rate of $\sim 6.44 \times 10^{16} \, cm^{-3} s^{-1}$. Since the n=3 state has a excitation energy of $12.08 \, eV$, the pumping mechanism consumes energy at a rate of $\sim 0.124 \, W \cdot cm^{-3}$, which is returned as H_α and H_β radiation.

E. High resolution visible spectroscopy recorded on hydrogen microwave discharge and KNO_3 and $RbNO_3$ rt-plasmas

a. Free-free and bound-free emission of lower-energy state hydride ion formed by KNO_3 and $RbNO_3$ catalysts

The hydrogen microwave spectrum in the region 4000-4090 Å is shown in Figures 17 and 18. The same region of a KNO_3 rt-plasma is shown in Figure 19 with expanded views of the 4000-4060 and 4060-4090 Å shown in Figure 20 and 21, respectively. By comparison of the rt-plasma emission to that of control hydrogen, a novel series of lines was observed in the region 4065-4090 as shown by the wavelength-label peaks in Figures 19 and 21 and given in Table 6. A second novel series of spectra lines was observed in the region of 3995-4060 that are partially shown in Figures 19 and 20 and given in Table 7. The two novel series of spectral lines in the region 3995-4090 Å were observed from the $RbNO_3$ as well as the KNO_3 rt-plasmas. They were also observed from the $CsNO_3$ rt-plasmas, but the intensity was much lower. These peaks could not be assigned to known species present in the cell or contaminants. However, the data is explained by a catalytic reaction of atomic hydrogen to form a more stable hydride ion designated $H^-(1/2)$.

The $2K^+$ and Rb^+ catalyst product $H(1/2)$ was predicted to be a highly reactive intermediate which further reacts to form a novel hydride ion $H^-(1/2)$ with a predicted binding energy of $3.0468\,eV$ given by the following formula [9, 39] for the hydride binding energies E_B:

$$E_B = \frac{\hbar^2 \sqrt{s(s+1)}}{8\mu_e a_0^2 \left[\dfrac{1+\sqrt{s(s+1)}}{p}\right]^2} - \frac{\pi\mu_0 e^2 \hbar^2}{m_e^2 a_0^3}\left(1+\frac{2^2}{\left[\dfrac{1+\sqrt{s(s+1)}}{p}\right]^3}\right) \tag{13}$$

where p is an integer greater than one (1/2 in this case), $s = 1/2$, $\hbar$ is Planck's constant bar, μ_0 is the permeability of vacuum, m_e is the mass of the electron, μ_e is the reduced electron mass, a_0 is the Bohr radius, and e is the elementary charge. The ionic radius is

$$r_1 = \frac{a_0}{p}\left(1 + \sqrt{s(s+1)}\right); \; s = \frac{1}{2} \tag{14}$$

Hydride ions form by the reaction of hydrogen or $H(1/p)$ atoms with

free electrons which have a kinetic energy distribution. The release of the electron kinetic energies and the hydride ion binding energy gives rise to the bound-free emission band to shorter wavelengths than the ionization or binding energy of the corresponding hydride ion. Due to the requirement that flux is linked by the hydrogen or $H(1/p)$ in integer units of the magnetic flux quantum, the energy is quantized, and the emission due to hydride ion formation comprises a series of hyperfine lines in the corresponding bound-free band. The derivation of the bound-free hyperfine lines due to interactions of the free and bound electrons was given previously [39]. From the electron g factor, bound-free hyperfine structure lines of $H^-(1/2)$ were predicted with energies E_{HF} given by the sum of the binding energy peak E_B^* (Eqs. (13) and (14) with the fine structure), the spin-pairing or spin-spin energy E_{ss}, and the fluxon energy E_Φ that were derived previously [39].

$$E_{HF} = E_\Phi + E_{ss} + E_B^* = j^2 2(g-2)\frac{\mu_B}{\sqrt{s(s+1)}}\frac{\mu_0}{r^3}\left(\frac{e\hbar}{2m_e}\right) + g\frac{\mu_0}{r^3}\left(\frac{e\hbar}{2m_e}\right)^2 + E_B^* \qquad (15)$$

where j is an integer.

In this section we show that the novel lines are assigned to emission during the binding of a free electron with the catalysis product $H(1/2)$, to form a novel hydride ion $H^-(1/2)$. The energy level diagram for the free-free and bound-free transitions corresponding to $H(1/2)[2P_{3/2}] + e^- \rightarrow H^-(1/2)[1S_0]$ given in Tables 6 and 7, respectively, is shown in Figure 22. The spectrometer had a sufficiently high resolution (± 0.06 Å) to resolve free-free and bound-free hydride ion transitions corresponding to fine structure and hyperfine structure energies, respectively. The assignments were established based on the analysis of a number of control plasmas, and the possible alternatives comprising species and contaminants in this reaction were also considered and eliminated as the source of the peaks assigned to $H^-(1/2)$ as described previously [39].

b. assignments of $H^-(1/2)$ free-free hyperfine lines recorded on KNO_3 and $RbNO_3$ rt-plasmas

We show in this section that the predicted binding energy of

2 2

3.0468 eV was observed as a continuum threshold at 4068.2 Å, and a structured, strong emission peak at 4071 Å corresponding to the fine structure and hyperfine structure of $H(1/2)$. Other elements which have emission in this region of 4071 Å such oxygen and carbon were eliminated based on the absence of corresponding lines as discussed previously [39]. Hydrogen, the most likely candidate, was also eliminated.

Hydrogen alone does not form an rt-plasma [7, 8, 24, 35, 39, 41, 42, 45]. The brightest hydrogen plasma that was used for line assignment was the hydrogen microwave plasma. The high resolution visible spectra (4000-4060 Å) and (4060-4090 Å) recorded on the emission of a control hydrogen microwave discharge plasma are shown in Figures 17 and 18, respectively. The high resolution visible spectrum in the region of 4000 Å to 4090 Å recorded on the emission of a rt-plasma formed with K^+/K^- catalyst from vaporized KNO_3 is shown in Figure 19 with the expanded views of the 4000-4060 Å and 4060-4090 Å regions shown in Figures 20 and 21, respectively. A broad peak was observed at 4071 Å with a FWHM of 1.2 Å. The strong 4071 Å peak was not observed in the hydrogen glow or microwave discharge plasmas as shown for the microwave plasma in Figures 17 and 18.

A comparison of the rt-plasma peaks with the $^3\Pi_{v=0}\rightarrow^3\Sigma_{v=2}$ ($4D\,0\rightarrow2B\,2$), $^3\Pi_{v=1}\rightarrow^3\Pi_{v=0}$ ($4e\,1\rightarrow2C\,0$), and $^3\Delta_{v=3}\rightarrow^3\Pi_{v=2}$ ($4f3\rightarrow2C\,2$) molecular hydrogen peaks reported in the literature [50] (both in air wavelengths) is given in Tables 8A, 8B, and 8C, respectively. The known transitions of molecular hydrogen that have peaks in the region of interest, 4071.5 ±1 Å, are the $^3\Pi_{v=0}\rightarrow^3\Sigma_{v=2}$ (R_1 and R_3 branches), $^3\Pi_{v=1}\rightarrow^3\Pi_{v=0}$ (Q_4 branch), and $^3\Delta_{v=3}\rightarrow^3\Pi_{v=2}$ (R_2 branch) transitions. In each case, none of the other peaks belonging to these same transitions were observed in the rt-plasma. Thus, based on the known transitions, the peak at 4071 Å could not be assigned to molecular hydrogen. $H^-(1/2)$ is a possible source of the 4071 Å peak shown in Figure 23.

The ionization profile of the ordinary hydride ion exhibits a continuum and has an low intensity ionization threshold at shorter wavelengths. Lykke et al. have measured the threshold for photodetachment of H^- [51]. According to the authors, "This very small cross section near threshold makes precise measurements of the

photodetachment threshold energy particularly difficult. Moreover, the difficulties are compounded by the presence of the hydrogen hyperfine structure, giving rise to two photodetachment thresholds within $0.05\,cm^{-1}$." The H^- photodetachment cross section rises with a $\Delta E^{3/2}$ dependence and has zero slope at threshold. Thus, the cross section is zero at threshold and rises slowly above threshold. The calculated absolute photodetachment cross section at $1\,cm^{-1}$ above the threshold is $10^{-21}\,cm^2$ [51]. For H^-, the Lykke data followed the $\Delta E^{3/2}$ threshold law to at least $60\,cm^{-1}$ above the photodetachment threshold where the cross section was observed to be zero.

As shown in Figure 23 a continuum was observed with a threshold at the predicted ionization energy of 3.04683 eV ($\lambda_{air} = 4068.2$ Å). However, the most intense emission was observed on the continuum at 4071.47 Å with a peak width of 1.2 Å. The peak energy was a close match to that of the $H^-(1/2)$ binding energy with the fine structure splitting of $H(1/2)$ given in Appendix II. The predicted energy difference between the $H(1/2)[^2P_{1/2}]$, $H(1/2)[^2S_{1/2}]$, and $H(1/2)[^2P_{3/2}]$ levels of the hydrogen atom, the fine structure splitting, given previously [9, 39] is

$$E_{s/o} = 8\alpha^5(2\pi)^2 m_e c^2 \sqrt{\frac{3}{4}} = 2.8922\,X\,10^{-3}\ eV \qquad (16)$$

The $H(1/2)[^2P_{3/2}]$, $H(1/2)[^2P_{1/2}]$, and $H(1/2)[^2S_{1/2}]$ levels are also split by spin-nuclear coupling, and the $H(1/2)[^2P_{3/2}]$ and $H(1/2)[^2P_{1/2}]$ levels are further split by orbital-nuclear coupling. $H(1/2)[^2S_{1/2}]$—$H(1/2)[^2P_{3/2}]$ and $H(1/2)[^2P_{1/2}]$—$H(1/2)[^2P_{3/2}]$ transitions occur between hyperfine levels; thus, the transition energy is the sum of the fine structure and the corresponding hyperfine energy. In addition to a continuum, the binding of an electron to $H(1/2)$ has a resonance emission with excitation of transitions between hyperfine levels of the fine structure levels.

$H(n = 1)$ does not have a fine structure transition since $\ell = 0$; thus, it shows only a hydride binding energy continuum [51, 52]. Whereas, ℓ may equal one for $H(1/2)$. The existence of the fine and hyperfine structure transitions in $H(1/2)$ provides a mechanism to observe a peak corresponding to the formation of a hydride ion. As an example, the binding of a highly excited state electron by its excitation of a fine structure transition of the corresponding atom is followed by the reaction

24

$H(1\cdot2p)\left[\,^2P_{3/2}\right]+e^- \rightarrow H\left(1/2s^2\right)\left[\,^1S_0\right]$. The corresponding emission is at a longer wavelength having an energy of the binding energy minus the fine structure energy. Since the hydride ion has a vanishing emission cross section in the region of its binding energy, but the fine structure transition has a significant cross section, the coupling of the electron binding to the fine structure transition may greatly increase the emission at this energy. An analogous process that results in strong absorption in transition metal complexes, for example, is well known as vibronic coupling. In this case, forbidden electronic transitions couple to vibrational transitions with a dramatic increase in the absorption cross section.

The peak due to the binding energy (Eqs. (6) and (7))) with excitation of the fine structure splitting (Eq. (16)) is given by

$$E_{slo} = E_B - E_{slo} = 3.04682 \; eV - 2.8922 \; X \; 10^{-3} \; eV = 3.0439 \; eV \; \; (\lambda_{air} = 4072.0 \; \text{Å}) \quad (17)$$

A peak was observed at this position as shown in Figures 21 and 23. The fine structure transitions occur between different hyperfine levels. The hyperfine splittings of $H(1/2)$ given in Appendix II are $1.197 \; X \; 10^{-4} \; eV$ and $3.153 \; X \; 10^{-4} \; eV$ for $\ell = 0$ and $\ell = 1$, respectively. The results of the deconvolution analysis of the peak at 4071 Å fit three peaks very well as shown in Figure 23. The deconvolved peaks were separated by energies that were comparable to the hyperfine splitting of the $H(1/2)$. The peak position, energies and adjacent peak separations are given in Table 9.

In addition to the absence of emission from the necessary accompanying hydrogen transitions corresponding to the $^3\Pi_{\upsilon=0} \rightarrow ^3\Sigma_{\upsilon=2}$ (R_1 and R_3 branches), $^3\Pi_{\upsilon=1} \rightarrow ^3\Pi_{\upsilon=0}$ (Q_4 branch), and $^3\Delta_{\upsilon=3} \rightarrow ^3\Pi_{\upsilon=2}$ (R_2 branch) transitions, the 4071 Å peak may not be due to molecular hydrogen based on the observed intensity and its relationship to other novel peaks in this region. It is interesting that the tops of the peaks at 4075.9, 4078.9, 4079.8, and 4081.7 Å shown in Figures 19 and 21 could be reproducibly connected by a line which indicates a relationship between these lines. The overlay of the high resolution visible spectrum in the region of 3900 Å to 4090 Å recorded on the emission of the KNO_3 rt-plasma and the control hydrogen microwave discharge plasma is shown

in Figure 24. The peaks at 4071 Å, 4075.9 Å, 4078.9 Å, and 4083.6 Å could not be assigned to hydrogen based on intensity. Other molecular hydrogen peaks in the region of interest, 4000-4090 Å, of the rt-plasmas were very small, even for the most intense hydrogen peaks observed in the controls. Only the accompanying peaks at 4079.8 and 4081.7 Å could be reproduced in any control hydrogen plasma source studied, and the peaks at 4075.9 Å, 4078.9 Å, and 4083.6 Å could not be assigned to hydrogen due to the absence of matching peaks in the hydrogen spectrum. The peaks shown in Figures 21 and 24 at 4075.9, 4078.9, and 4083.6 were also novel based on the absence of required corresponding branches of the known transitions at these wavelengths according to Crosswhite [51]. The unique intensity profile of the set of peaks shown in Figures 19, 21, and 24 may indicate an energy transfer process from the free-free transitions of the hydride ion. Furthermore, the intensity profile of the rt-plasma in the region of 4000-4060 Å was extraordinary in that it was absolutely flat as discussed previously [39]. These issues are being further investigated.

One possible explanation of the series in the region 4071-4084 Å is that the binding of an electron to $H(1/2)$ has a resonance emission with excitation of transitions between hyperfine levels of the fine structure levels. In this case, the free-free spectrum of $H^-(1/2)$ has a series of peaks separated from the binding energy by an integer multiple of the fine structure. The emission may be observed directly, or a resonance transfer may occur with molecular hydrogen. From Eqs. (6), (7), and (16), the predicted energies are given by

$$E_{s/o} = E_B - qE_{s/o} = 3.04682\ eV - q2.8922\ X\ 10^{-3}\ eV \tag{18}$$

were q is an integer. The calculated energies and air wavelengths of the peaks corresponding to the $H^-(1/2)$ binding energy coupled to an integer multiple of the fine structure energy compared to the experimental air wavelengths in the region of 4071-4084 Å are given in Table 6. The peaks at 4071.0, 4075.9, 4079.8, and 4083.6 were an excellent match for $q = 1$, 2, 3, and 4, respectively. The peaks observed at 4078.9 and 4081.7 Å which are adjacent to the peaks at 4079.8 and 4083.6 Å may correspond to hyperfine transitions within the fine structure transition as

26

observed for the 4071.0 Å peak and proposed for an inverse Rydberg series of peaks observed in the region 3995-4060 Å as discussed in Sec. 3Ec.

It was an additional objective of the present paper to identify the bound-free hyperfine peaks corresponding to the 4071 Å $H^-(1/2)$ peak having energies given by Eq. (15). According to Eq. (15), the predicted electron interactions for $H^-(1/2)$ are 8 times more energetic than those of ordinary hydride ion. The spectrometer had a sufficiently high resolution (± 0.06 Å) so that $H^-(1/2)$ bound-free hyperfine lines could be observed. As discussed in Sec. 3Ec, these peaks were observed as an inverse Rydberg series, and each of these peaks could also be deconvolved into at least three peaks that were comparable to the hyperfine splitting observed for the 4071 Å peak assigned to $H^-(1/2)$. A future study will address the details of the fine structure and hyperfine structure transition assignments and predicted intensities.

c. assignments of $H^-(1/2)$ bound-free hyperfine lines recorded on KNO_3 and $RbNO_3$ rt-plasmas

From the electron g factor, bound-free hyperfine structure lines of $H^-(1/2)$ were predicted previously [39] with energies E_{HF} given by $E_{HF} = j^2 3.00213 \, X \, 10^{-5} + 3.0563 \, eV$ (j is an integer) as an inverse Rydberg-type series from 3.0563 eV to 3.1012 eV—the hydride binding energy peak with the fine structure plus one and five times the spin-pairing energy, respectively. We shown in this section that high resolution visible rt-plasma emission spectra in the region of 3995 Å to 4060 Å, such as that recorded on a KNO_3 rt-plasma shown in Figures 91-20, matched the predicted emission lines for $j = 1$ to $j = 39$ with the series edge at 3996.3 Å up to 1 part in 10^4. The structure of these peaks also matched that of $H^-(1/2)$.

All species present in the rt-plasma reaction or possible contaminants were eliminated as the source of the series of 39 lines as described previously [39]. In particular, nitrogen, air, and hydrogen were dispositively eliminated based on precise comparisons of the wavelengths, intensity profiles, peak widths, and peak shapes. For example, the novel lines were only observed in the case of the rt-plasmas

27

of KNO_3 and $RbNO_3$. They were not observed in any of the plasmas which were controls for the rt-plasmas and run identically. No emission or only hydrogen and alkali emission was observed in the case of the controls. Thus, the peaks were clearly not air or nitrogen peaks. If they were contaminant peaks, then they would have been present in the control plasmas as well.

Of the possible molecules, N_2, NO, NO_2 , NH_3, O_2, and H_2O, only N_2 is a candidate for the source of the 39 observed lines since the emission due to a branch of the $v' = 0 - v'' = 3$ vibration-rotational band of the N_2 $^3\Pi_u$ (denoted by C) to $^3\Pi_g$ (denoted by B) electronic excited state transition (denoted C-B emission band) is in this region. The gold standard for the assignment of a spectrum to a particular source is to compare the unknown spectrum to that of the spectrum of the known species wherein the wavelengths are calibrated in both spectra. The overlay of the wavelength-calibrated spectra (3900-4090 Å) of the KNO_3 rt-plasma and the nitrogen microwave plasma is shown in Figure 25. The wavelengths of the spectral lines do not match, and the additional vibration-rotational band heads of nitrogen recorded on control nitrogen plasma and given in Table 10 are not observed in the rt-plasma which eliminates nitrogen as the source of the emission recorded on the rt-plasma.

The emission in the spectral regions outside of the inverse Rydberg series of lines was due to hydrogen—not nitrogen. The inverse Rydberg series of lines observed from the rt-plasma was not observed from hydrogen as well as air or nitrogen microwave plasmas in the region 3995-4056 Å. The emission of either rt-plasma with the addition of air showed nitrogen vibration-rotational features in this region rather than the novel series of lines [39]. The overlay of the high resolution visible spectrum in the region of 3900 Å to 4090 Å recorded on the emission of the KNO_3 rt-plasma and a control hydrogen microwave discharge plasma is shown in Figure 26. The hydrogen molecular peaks matched those of the rt-plasma in the region 3900 to 3995 wherein the rt-plasma peaks were broadened due to excitation by the hydride ion continuum emission. However, the inverse Rydberg series of lines was absent from the control hydrogen spectrum. Thus, hydrogen was eliminated as the source of the novel series of lines recorded on the rt-plasma.

The inverse Rydberg series of peaks shown in Figures 19 and 20

appeared on a flat continuum which may have been due to the continuum nature of the binding energy of the hydride ion $H^-(1/2)$. As discussed in Sec. 3Eb, the observation of hydride ion peaks requires an electron binding threshold with a large cross section. The experimental threshold of the $H^-(1/2)$ peak at 4070.6 Å (air wavelength) which was in agreement with theory was used to calculate the peak positions of the series of 39 bound-free hyperfine lines given in Table 7 in air wavelengths [21].

Substitution of the energy of 3.0451 eV, corresponding to the air wavelength of the observed threshold of the hydride peak, 4070.6 Å, into Eq. (15) for E_B gives

$$E_{HF} = E_{\Phi} + E_{ss} + E_B = j^2 3.00213 \, X \, 10^{-5} + 0.011223 + 3.0451 \, eV$$

$$(j \text{ is an integer}) \quad (19)$$

$$= j^2 3.00213 \, X \, 10^{-5} + 3.0563 \, eV$$

The predicted inverse Rydberg-type series that converges at increasing wavelengths and terminates at 3.0563 eV was observed as shown in Figures 19 and 20 for $j = 1$ to $j = 37$ as given in Table 7.

The high resolution visible plasma emission spectra in the region of 3995 Å to 4060 Å shown in Figure 27 matched the predicted emission lines given by Eq. (19) for $j = 1$ to $j = 39$ with the series edge at 3996.3 Å. As shown in Figure 27, the Rydberg-type series extended from 3.0563 eV to 3.1012 eV. Other peaks in the rt-plasma that partially covered some of the bound-free hyperfine peaks were assigned to molecular hydrogen and K I. In addition, K II was observed outside this region at 4829.23 Å which confirmed the presence of the catalyst K^+/K^+.

It was shown previously [39] that the maximum energy due to flux for both electrons $E_{\Phi max}$ is given by

$$E_{\Phi max} = g \frac{\mu_0}{r^3} \left(\frac{e\hbar}{m_e} \right)^2 \quad (20)$$

With the radius given by Eq. (14), the maximum fluxon energy $E_{\Phi max}$ of $H^-(1/2)$ in Eq. (19) is given by

$$E_{\Phi max} = 4E_{ss} = 4(0.011223) \, eV = 0.044892 \, eV \quad (21)$$

The predicted cutoff of the bound-free hyperfine series is at 3.1012 eV (3996.8 Å). A final broad peak is observed at this position as shown in Figure 27. It is assigned to the partially cutoff $j = 39$ member of the

series predicted to be at 3995.9 Å. The peak observed at 3997.9 Å may be a hydrogen peak. The bound-free hyperfine peak corresponding to $j = 38$ occurs just before the cutoff at 3996.3 Å. The peaks at 3998.5 Å, 3999.6Å, and 3999.1 Å are at positions consistent with a set comprising three peaks that follow the same hyperfine structure pattern observed with other peaks of the series as shown by deconvolution analysis in Figure 36. The preceding $j = 37$ peak, for example, overlays these three peaks very well. However, the intensity of the shorter wavelength transitions are diminished relative to those at longer wavelengths possibly due to the cutoff as the edge at 3996.3 Å is approached.

The high resolution visible spectrum in the region of 4000 Å to 4090 Å recorded on the emission of a rt-plasma formed with Rb^+ catalyst from vaporized $RbNO_3$ is shown in Figure 28 with the expanded views of the 4000-4060 Å and 4060-4090 Å regions are shown in Figures 29 and 30, respectively. The $H^-(1/2)$ hydride ion peak was observed at 4071 Å as shown in Figures 28 and 30. An inverse Rydberg-type series of broad emission lines shown in Figures 28 and 29 that converged at increasing wavelengths and terminated at about 3.0563 eV—the hydride binding energy with the fine structure plus the spin-pairing energy—matched the theoretical bound-free hyperfine energies E_{HF} given by Eq. (19) for $j = 1$ to $j = 37$. The results are presented in Table 7. Other peaks in the rt-plasma that partially covered some of the bound-free hyperfine peaks were assigned to molecular hydrogen. In addition to hydrogen molecular lines, a Rb II peak was observed in Figure 29 which confirmed the presence of the catalyst Rb^+.

The emission spectra of the $H^-(1/2)$ hydride ion and the corresponding bound-free hyperfine lines were very reproducible. The good match of the emission spectra of the $H^-(1/2)$ hydride ion and the corresponding bound-free hyperfine lines recorded on the KNO_3 and $RbNO_3$ rt-plasmas are shown in Figures 31 and 32 and which also confirmed the wavelength calibration. Three matching high resolution visible spectra (4000-4100 Å) of Rb^+ rt-plasmas that were equivalent to the spectrum of the K^+/K^+ and the Rb^+ rt-plasmas shown in Figures 19 and 28, respectively, are shown in Figure 33. The expanded view of the 4000-4060 Å region of Figure 33 is shown in Figure 34. The theoretical bound-free hyperfine energies, theoretical air wavelengths, observed air

30

wavelengths, and the difference between the two are given in Table 7. The remarkable agreement is further evident in Figure 35 which shows the wavelengths of the observed peaks overlaid on the plot of the theoretical wavelengths calculated from Eq. (19).

In addition to the $H^-(1/2)$ peak shown in Figure 23, the hydride bound-free hyperfine lines also had structure that could be deconvolved into at least three peaks as discussed in Sec 3Eb. As shown for the representative bound-free hyperfine peaks shown in Figure 36, the results of each deconvolution analysis fit three peaks very well. The reproducible structure of the bound-free hyperfine peaks is evident from the three matching spectra of Rb^+ rt-plasmas shown in Figures 33 and 34. This splitting can not be due to an isotope splitting of any hypothetical rotational transitional lines based on natural abundance, corresponding vibrational energy shifts, and the dependency on J.

Rather, $H^-(1/2)$ is formed by the reaction of an electron with $H(1/2)$. Thus, the $H^-(1/2)$ bound-free hyperfine lines are predicted to be split by the spin and orbital-nuclear coupling of $H(1/2)$ called the $H(1/2)$ hyperfine structure as discussed in Sec. 3Eb. The theory is given in the Refs. 67 and 33. The hyperfine structure $\Delta E_{total}^{S/N\,O/N}$ comprises spin-nuclear and orbital-nuclear coupling energies. The result of the derivation given previously by Mills [9] is

$$\Delta E_{total}^{S/N\,O/N} = \frac{pe^2}{8\pi\varepsilon_o}\left[\frac{1}{r_-} - \frac{1}{r_+}\right] - \left(\sqrt{\ell(\ell+1)} + \sqrt{\frac{3}{4}}\right)2\mu_P \frac{p^3\mu_0 e\hbar}{m_e a_H^3} \tag{22}$$

where

$$r_{1\pm} = \frac{a_H + \sqrt{a_H^2 \pm \dfrac{6\mu_0 e\left(\sqrt{\ell(\ell+1)} + \sqrt{\frac{3}{4}}\right)\mu_P a_o}{\hbar}}}{2p} \tag{23}$$

Evaluation of Eq. (22) using Eq. (23) with $p=2$ (corresponding to $H^-(1/2)$) and $\ell=0$ gives the hyperfine structure as $28.95\,GHz\,(1.197\,X\,10^{-4}\,eV)$. With $\ell=1$, the hyperfine structure is $76.23\,GHz\,(3.153\,X\,10^{-4}\,eV)$ (See Table 2.3 of Refs. 67 and 113). The deconvolved peaks were separated by energies that were comparable to the hyperfine splitting of the $H(1/2)$. The peak position, energies, and adjacent peak separations for the representative peak shown in Figure 36 are given in Table 11. A future study will

31

address the details of the fine structure and hyperfine structure transition assignments and predicted intensities.

4. Conclusion

$2K^+$ to $K + K^{2+}$, Rb^+ to Rb^{2+}, and Cs to Cs^{2+} each provide a reaction with a net enthalpy equal to the potential energy of atomic hydrogen, $27.2\,eV$, and K to K^{3+} provides a reaction with a net enthalpy equal to $3 \cdot 27.2\,eV$. The presence of these gaseous atoms and ions with thermally dissociated hydrogen formed a plasma having strong VUV emission. Emission was observed from Rb^+, Rb^{2+}, K, K^+, K^{2+}, K^{3+}, Cs, Cs^-, and Cs^{2+} that confirmed the resonant energy transfer with the formation of the corresponding rt-plasma. Emission was also observed from a continuum state of Cs^{2+} at 533 Å. The single emission feature with the absence of the other corresponding Rydberg series of lines from species confirmed the resonant energy transfer of $27.2\,eV$ from atomic hydrogen to atomic cesium.

A stationary inverted Lyman population was observed with potassium and rubidium catalysts. The ionization and population of excited atomic hydrogen levels was attributed to energy provided by the rt-plasma reactions. The high hydrogen atom temperature of the KNO_3 and $RbNO_3$ rt-plasmas of 18 eV and 12 eV, respectively, with a relatively low electron temperature, $T_e \sim 1\,eV$, were characteristic of cold recombining plasmas [6]. These conditions of the rt-plasmas favored an inverted population in the lower levels. Thus, the catalysis of atomic hydrogen may pump a cw HI laser. From our results, laser oscillations are expected between $n = 3$ and $n = 2$.

The K^+ / K^+ and Rb^+ catalysis product, $H(1/2)$, was predicted to form hydride ion $H^-(1/2)$. This hydride ion with a predicted binding energy of $3.0468\,eV$ was observed by high resolution visible spectroscopy as a continuum threshold at 4068.2 Å. A structured, strong emission peak was observed at 4071 Å corresponding to the formation of $H^-(1/2)$ from $H(1/2)$ with coupling of the electron binding to the fine structure of $2.8922 \times 10^{-3}\,eV$ and spin and orbital-nuclear hyperfine splitting of $1.197 \times 10^{-4}\,eV$ and $3.153 \times 10^{-4}\,eV$. From the electron g factor, bound-free hyperfine structure lines of $H^-(1/2)$ were predicted with energies E_{HF}

32

given by $E_{HF} = j^2 3.00213 \, X \, 10^{-5} + 3.0563 \, eV$ (j is an integer) as an inverse Rydberg-type series from 3.0563 eV to 3.1012 eV—the hydride binding energy peak plus one and five times the spin-pairing energy, respectively. The match of the rt-plasma spectra in the region of 3995 Å to 4060 Å with the predicted inverse Rydberg series of emission lines for $j = 1$ to $j = 39$ up to 1 part in 10^4, the edge at 3996.3 Å, as well the hyperfine structure due to spin and orbital-nuclear splitting all shown in Figure 27 is very convincing evidence for the identification of $H^-(1/2)$ formed from $H(1/2)$. All other possibilities for the assignments were eliminated. Hydrogen could not account for the lines in the region of interest, but did account for all lines outside of the region of interest.

No fine structure coupling is possible for $H(n = 1)$, and the bound-free hyperfine lines of ordinary hydride ion may not be sufficiently energetic to be resolved. But, these limitations do not exist in the case of $H(1/2)$ and $H^-(1/2)$, respectively. We report the observation of bound-free hyperfine energy levels of a hydride ion and well as fine structure and hyperfine structure of the corresponding reactant atom having a fractional principal quantum number.

References

1. C. Zimmermann, R. Kallenbach, T. W. Hansch, Phys. Rev. Lett., Vol. 65, (1990), p. 571.
2. T. Ibuki, Chem. Phys. Lett., Vol. 94, (1990), p. 169.
3. L. I. Gudzenko, L. A. Shelepin, Sov. Phys. JEPT, Vol. 18, (1963), p. 998.
4. S. Suckewer, H. Fishman, J. Appl. Phys., Vol. 51, (1980), p. 1922.
5. W. T. Silfvast, O. R. Wood, J. Opt. Soc. Am. B, Vol. 4, (1987), p. 609.
6. H. Akatsuka, M. Suzuki, "Stationary population inversion of hydrogen in arc-heated magnetically trapped expanding hydrogen-helium plasma jet", Phys. Rev. E, Vol. 49, (1994), pp. 1534-1544.
7. R. Mills, J. Dong, Y. Lu, "Observation of Extreme Ultraviolet Hydrogen Emission from Incandescently Heated Hydrogen Gas with Certain Catalysts", Int. J. Hydrogen Energy, Vol. 25, (2000), pp. 919-943.
8. R. Mills and M. Nansteel, P. Ray, "Argon-Hydrogen-Strontium Discharge Light Source", IEEE Transactions on Plasma Science, April, (2002).
9. R. Mills, *The Grand Unified Theory of Classical Quantum Mechanics*,

September 2001 Edition, BlackLight Power, Inc., Cranbury, New Jersey, Distributed by Amazon.com; posted at www.blacklightpower.com; July 2002 Edition posted at www.blacklightpower.com.

10. R. Mills, "The Grand Unified Theory of Classical Quantum Mechanics", Int. J. Hydrogen Energy, Vol. 27, No. 5, (2002), pp. 565-590.

11. R. Mills, "The Nature of Free Electrons in Superfluid Helium--a Test of Quantum Mechanics and a Basis to Review its Foundations and Make a Comparison to Classical Theory", Int. J. Hydrogen Energy, Vol. 26, No. 10, (2001), pp. 1059-1096.

12. N. V. Sidgwick, *The Chemical Elements and Their Compounds*, Volume I, Oxford, Clarendon Press, (1950), p.17.

13. M. D. Lamb, *Luminescence Spectroscopy*, Academic Press, London, (1978), p. 68.

14. R. Mills, P. Ray, "Spectral Emission of Fractional Quantum Energy Levels of Atomic Hydrogen from a Helium-Hydrogen Plasma and the Implications for Dark Matter", Int. J. Hydrogen Energy, Vol. 27, No. 3, pp. 301-322.

15. R. L. Mills, P. Ray, B. Dhandapani, M. Nansteel, X. Chen, J. He, "Spectroscopic Identification of Transitions of Fractional Rydberg States of Atomic Hydrogen", J. of Quantitative Spectroscopy and Radiative Transfer, in press.

16. R. L. Mills, P. Ray, B. Dhandapani, M. Nansteel, X. Chen, J. He, "New Power Source from Fractional Quantum Energy Levels of Atomic Hydrogen that Surpasses Internal Combustion", J Mol. Struct., in press.

17. David R. Linde, *CRC Handbook of Chemistry and Physics*, 79 th Edition, CRC Press, Boca Raton, Florida, (1998-9), p. 10-175 to p. 10-177.

18. NIST Atomic Spectra Database, www.physics.nist.gov/cgi-bin/AtData/display.ksh.

19. R. L. Mills, P. Ray, B. Dhandapani, J. He, "Comparison of Excessive Balmer α Line Broadening of Glow Discharge and Microwave Hydrogen Plasmas with Certain Catalysts", J. of Applied Physics, submitted.

20. J. Tadic, I. Juranic, G. K. Moortgat, "Pressure dependence of the photooxidation of selected carbonyl compounds in air: n-butanal and n-pentanal", J. Photochemistry and Photobiology A: Chemistry, Vol. 143, (2000), 169-179.

21. David R. Linde, *CRC Handbook of Chemistry and Physics*, 76 th Edition,

CRC Press. Boca Raton. Florida, (1995-1996), p. 10-304.

22. D. Barton, J. W. Bradley, D. A. Steele, and R. D. Short, "Investigating radio frequency plasmas used for the modification of polymer surfaces," J. Phys. Chem. B, Vol. 103, (1999), pp. 4423-4430.

23. H. R. Griem, *Principle of Plasma Spectroscopy*, Cambridge University Press. (1987).

24. H. Conrads, R. Mills, Th. Wrubel, "Emission in the Deep Vacuum Ultraviolet from an Incandescently Driven Plasma in a Potassium Carbonate Cell", Plasma Sources Science and Technology, submitted.

25. I. R. Videnovic, N. Konjevic, M. M. Kuraica, "Spectroscopic investigations of a cathode fall region of the Grimm-type glow discharge", Spectrochimica Acta, Part B, Vol. 51, (1996), pp. 1707-1731.

26. M. Kuraica, N. Konjevic, "Line shapes of atomic hydrogen in a plane-cathode abnormal glow discharge", Physical Review A, Volume 46, No. 7, October (1992), pp. 4429-4432.

27. S. B. Radovanov, K. Dzierzega, J. R. Roberts, J. K. Olthoff, "Time-resolved Balmer-alpha emission from fast hydrogen atoms in low pressure, radio-frequency discharges in hydrogen", Appl. Phys. Letts., Vol. 66, No. 20, (1995), pp. 2637-2639.

28. S. Djurovic, J. R. Roberts, "Hydrogen Balmer alpha line shapes for hydrogen-argon mixtures in a low-pressure rf discharge", J. Appl. Phys., Vol. 74, No. 11, (1993), pp. 6558-6565.

29. R. L. Mills, P. Ray, "Substantial Changes in the Characteristics of a Microwave Plasma Due to Combining Argon and Hydrogen", New Journal of Physics, www.njp.org, Vol. 4, (2002), pp. 22.1-22.17.

30. J. Seidel, "Theory of two-photon polarization spectroscopy of plasma-broadened hydrogen L_α line", Phys. Rev. Letts., Vol. 57, No. 17, (1986), p. 2154.

31. A. Czernikpwski, J. Chapelle, Acta Phys. Pol. A., Vol. 63, (1983), p. 67.

32 M. A. Gigosos, V. Cardenoso, "New plasma diagnosis tables of hydrogen Stark broadening including ion dynamics", J. Phys. B: At. Mol. Opt. Phys., Vol. 29, (1996), pp. 4795-4838.

33. H. Okabe, *Photochemistry of Small Molecules*, John Wiley & Sons, New York, (1978).

34. A. Corney, Atomic and Laser Spectroscopy, Clarendon Press, Oxford,

(1977).

35. R. Mills, P. Ray, "Spectroscopic Identification of a Novel Catalytic Reaction of Potassium and Atomic Hydrogen and the Hydride Ion Product", Int. J. Hydrogen Energy, Vol. 27, No. 2, (2002), pp. 183-192.

36. R. Kelly, Journal of Physical and Chemical Reference Data, "Atomic and Ionic Spectrum Lines below 2000 Angstroms: Hydrogen through Krypton", Part I (H-Cr), Volume 16, (1987), Supplement No. 1, Published by the American Chemical Society and the American Institute of Physics for the National Bureau of Standards, pp. 418-422.

37. J. Reader, G. L. Epstein, "Resonance lines of Cs II, Ba III, and La IV", Journal of the Optical Society of America, Vol. 65, No. 6, June, (1975), pp. 638-641.

38. I. S. Aleksakhin, G. G. Bogachev, A. I. Zapesochnyi, "Study of the emission of potassium, rubidium, and cesium in the 45-75 nm region during electron-atom collisions", J. Applied Spectroscopy, Vol. 23, No. 6, December, (1975), pp. 1666-1668. Translated from Zh. Prikl. Spektrosk. (USSR), Vol. 23, No. 6, December (1975), pp. 1103-1105.

39. R. L. Mills, P. Ray, "A Comprehensive Study of Spectra of the Bound-Free Hyperfine Levels of Novel Hydride Ion $H^-(1/2)$, Hydrogen, Nitrogen, and Air", Int. J. Hydrogen Energy, in press.

40. R. Mills, P. Ray, "Vibrational Spectral Emission of Fractional-Principal-Quantum-Energy-Level Hydrogen Molecular Ion", Int. J. Hydrogen Energy, Vol. 27, No. 5, (2002), pp. 533-564.

41. R. Mills, "Spectroscopic Identification of a Novel Catalytic Reaction of Atomic Hydrogen and the Hydride Ion Product", Int. J. Hydrogen Energy, Vol. 26, No. 10, (2001), pp. 1041-1058.

42. R. L. Mills, P. Ray, "Spectroscopic Identification of a Novel Catalytic Reaction of Rubidium Ion with Atomic Hydrogen and the Hydride Ion Product", Int. J. Hydrogen Energy, Vol. 27, No. 9, (2002), pp. 927-935.

43. R. L. Mills, X. Chen, P. Ray, J. He, B. Dhandapani, "Plasma Power Source Based on a Catalytic Reaction of Atomic Hydrogen Measured by Water Bath Calorimetry", Thermochimica Acta, submitted.

44. R. Mills, P. Ray, R. M. Mayo, "The Potential for a Hydrogen Water-Plasma Laser", Applied Physics Letters, submitted.

45. R. Mills, T. Onuma, and Y. Lu, "Formation of a Hydrogen Plasma from an Incandescently Heated Hydrogen-Catalyst Gas Mixture with an

Anomalous Afterglow Duration", Int. J. Hydrogen Energy, Vol. 26, No. 7, July, (2001), pp. 749-762.

46. R. Mills, B. Dhandapani, M. Nansteel, J. He, T. Shannon, A. Echezuria, "Synthesis and Characterization of Novel Hydride Compounds", Int. J. of Hydrogen Energy, Vol. 26, No. 4, (2001), pp. 339-367.

47. R. Mills, B. Dhandapani, N. Greenig, J. He, "Synthesis and Characterization of Potassium Iodo Hydride", Int. J. of Hydrogen Energy, Vol. 25, Issue 12, December, (2000), pp. 1185-1203.

48. S. B. Radovanov, K. Dzierzega, J. R. Roberts, J. K. Olthoff, "Time-resolved Balmer-alpha emission from fast hydrogen atoms in low pressure, radio-frequency discharges in hydrogen", Appl. Phys. Lett., Vol. 66, No. 20, (1995), pp. 2637-2639.

49. T. Fujimoto, J. Phys. Soc. Jpn., Vol. 47, (1979). p. 265.

50. H. M. Crosswhite, Editor, "The Hydrogen Molecule Wavelength Tables of Gerard Heinrich Dieke", Wiley-Interscience, New York, (1972), T66-T70.

51. K. R. Lykke, K. K. Murray, W. C. Lineberger, "Threshold photodetachment of H^-", Phys. Rev. A, Vol. 43, No. 11, (1991), pp. 6104-6107.

52. M. Stix, The Sun, Springer-Verlag, Berlin, (1991), p. 136.

53. A. Lofthus, P. H. Krupenie, "The spectrum of molecular nitrogen", J. Phys. Chem. Ref. Data, Vol. 6, No. 1, (1977), pp. 113-312.

54. D. Blois, P. Supiot, M. Barj, A. Chapput, C. Foissac, O. Dessaux, P. Goudmand, "The microwave source's influence of the vibrational energy carried by in a nitrogen afterglow", J. Phys. D: Appl. Phys., Vol. 31, (1998), pp. 2521-2531.

55. A. R. Striganov, N. S. Sventitskii, Tables of Spectral Lines of Neutral and Ionized Atoms, IFI/Plenum, New York, (1968), p. 893.

Table 1. Energetic hydrogen atom densities and energies for rt-plasmas determined from the 6563 Å Balmer α line width.

Plasma Gas	Hydrogen Atom Density[a] (10^{11} $atoms/cm^3$)	Hydrogen Atom Energy[b] (eV)
H_2	2	2-3[c]
$K; K^+ / K^- / H_2$	4	15-18
Rb^+ / H_2	6	9-12
Cs / H_2	4	10-12

[a] Approximate Calculated after [25].
[b] Calculated after [25].
[c] Measured on a microwave discharge after [14].

Table 2. Resonance lines of Cs II observed with a sliding spark on the 10.7 m normal incidence vacuum spectrometer at NBS [37]. The uncertainty of the wavelengths is ±0.005 Å.

λ (Å)	Intensity	σ (cm^{-1})	Upper Level
926.657	40000	107914.8	$6p^6 5d\ ^3P_1$
901.270	35000	110954.5	$6s3/2[3/2]_1$
813.837	15000	122874.7	$6s1/2[1/2]_1$
808.761	15000	123645.9	$5d\ ^3D_1$
718.138	15000	139249.0	$5d\ ^1P_1$
668.386	500	149614	$7s3/2[3/2]_1$
657.112	100	152181	$6d\ ^3P_1$
639.356	2000	156407	$6d\ ^3D_1$
612.756	35	163189	$7s1/2[1/2]_1$
591.044	250	169192	$6d\ ^1P_1$
607.291	50	164666	$8s3/2[3/2]_1$
575.320	10	173816	$6d\ ^3D_1$
564.158	1	177256	$7d\ ^1P_1$

Table 3. The population density ratios $\frac{N_\beta}{N_\alpha}$ and $\frac{N_\gamma}{N_\alpha}$ for pure H_2, KNO_3, and $RbNO_3$.

Plasma Gas	$\dfrac{N_\beta}{N_\alpha}$	$\dfrac{N_\gamma}{N_\alpha}$
Pure H_2 [a]	0.664	0.521
KNO_3	4.72	3.48
$RbNO_3$	4.30	1.26

[a] Measured on microwave discharge maintained after [14].

Table 4. The reduced population density ratios $\dfrac{N}{g}$ for pure H_2, KNO_3, and $RbNO_3$.

Plasma Gas	$\dfrac{N_\beta}{N_\alpha}\dfrac{g_\alpha}{g_\beta}$ a	$\dfrac{N_\gamma}{N_\alpha}\dfrac{g_\alpha}{g_\gamma}$ b
Pure H_2 [c]	0.292	0.130[c]
KNO_3	2.07	0.870
$RbNO_3$	1.89	0.314

[a] $\dfrac{g_\alpha}{g_\beta} = 0.444$ where $g = 2n^2$ and n is the principal quantum number

[b] $\dfrac{g_\alpha}{g_\gamma} = 0.250$

[c] Measured on microwave discharge after [14].

Table 5. Level densities N_n for excited states n=1 – 5 with an n=3 pumping mechanism.

n	$N_n(10^3\ cm^{-3})$
1	5000
2	0.18
3	1.25
4	0.000229
5	0.000138

Table 6. The calculated energies and air wavelengths of the peaks corresponding to the $H^-(1/2)$ binding energy coupled to an integer multiple of the fine structure energy compared to the experimental air wavelengths in the region of 4071-4084 Å.

Integer Multiple	Calculated Energy (eV) Eq. (18)	Calculated Wavelength (Å)	Observed Wavelength (Å)
1	3.0439	4071.0	4071.0
2	3.0410	4075.9	4075.9
			4078.9
3	3.0381	4079.8	4079.8
			4081.7
4	3.0353	4083.7	4083.6

Table 7. Calculated hyperfine emission lines of bound-free plasma emission of H^- (1/2) and the observed lines (both in air wavelengths).

Hyperfine Quantum Number j	Calculated Emission (eV) Eq. (19)	Calculated Emission (Å) Eq. (19)	Observed Lines (Å)	Difference between Experimental and Calculated (Å)	Relative Difference between Experimental and Calculated (Å)
1	3.0563	4055.6	4055.6	-0.06	-1.4E-05
2	3.0564	4055.4	4055.5	-0.04	-8.9E-06
3	3.0566	4055.2	4055.4	-0.12	-2.8E-05
4	3.0568	4055.0	4055.2	-0.20	-5.0E-05
5	3.0571	4054.6	4054.7	-0.10	-2.5E-05
6	3.0574	4054.2	4054.4	-0.19	-4.7E-05
7	3.0578	4053.7	4054.0	-0.33	-8.1E-05
8	3.0582	4053.1	4053.5	-0.46	-1.1E-04
9	3.0587	4052.4	4053.0	-0.62	-1.5E-04
10	3.0593	4051.6	4052.2	-0.58	-1.4E-04
11	3.0599	4050.8	4051.2	-0.41	-1.0E-04
12	3.0606	4049.9	4050.1	-0.24	-5.8E-05
13	3.0614	4048.9	4048.9	-0.02	-4.5E-06
14	3.0622	4047.8	4047.9	-0.09	-2.2E-05
15	3.0631	4046.7	4046.6	0.06	1.5E-05
16	3.0640	4045.4	4045.1	0.33	8.2E-05
17	3.0650	4044.1	4043.5	0.62	1.5E-04
18	3.0660	4042.7	4042.1	0.64	1.6E-04
19	3.0671	4041.3	4040.7	0.57	1.4E-04
20	3.0683	4039.7	4038.8	0.93	2.3E-04
21	3.0695	4038.1	4037.9	0.21	5.2E-05
22	3.0708	4036.4	4036.5	-0.09	-2.2E-05
23	3.0722	4034.6	4034.9	-0.30	-7.4E-05
24	3.0736	4032.8	4033.1	-0.32	-7.8E-05
25	3.0751	4030.9	4031.3	-0.49	-1.2E-04
26	3.0766	4028.9	4029.2	-0.35	-8.6E-05
27	3.0782	4026.8	4027.1	-0.35	-8.7E-05
28	3.0798	4024.6	4024.9	-0.28	-7.1E-05
29	3.0815	4022.4	4022.6	-0.21	-5.1E-05
30	3.0833	4020.1	4020.2	-0.12	-3.1E-05
31	3.0852	4017.7	4017.8	-0.09	-2.1E-05
32	3.0870	4015.2	4015.2	0.04	9.8E-06
33	3.0890	4012.7	4012.5	0.16	4.0E-05
34	3.0910	4010.1	4009.9	0.21	5.1E-05
35	3.0931	4007.4	4007.2	0.18	4.5E-05
36	3.0952	4004.6	4004.5	0.15	3.7E-05
37	3.0974	4001.8	4001.7	0.13	3.2E-05
38	3.0997	3998.9	3998.5	0.38	9.6E-05
39	3.1020	3995.9	3996.3	-0.40	-9.9E-05

Table 8A. A comparison of the rt-plasma peaks with the $^3\Pi_{\upsilon=0} \rightarrow {}^3\Sigma_{\upsilon=2}$ $(4D\,0 \rightarrow 2B\,2)$ molecular hydrogen peaks reported in the literature [50] (both in air wavelengths).

Branch	Literature Wavelength (Å)	Reported Intensity	Observed KNO_3 rt-plasma Intensity	Hydrogen Microwave Plasma Intensity
R_0	4062.600	1.0	no peak	observed
R_1	4071.666	1.07	strong peak assigned to $H^-(1/2)$	observed
R_2	4072.963	1.71	no peak	observed (most intense peak in this region in agreement with Crosswhite [56])
R_3	4071.414	0.7	inside $H^-(1/2)$ peak	observed
R_4	4066.141	0.9	no peak	observed
R_5	4057.156	0.53	no peak	observed
R_6	4044.610	0.3	covered by K line	observed

Table 8B. A comparison of the rt-plasma peaks with the $^3\Pi_{v=1}\to{}^3\Pi_{v=0}$ ($4e1\to2C0$) molecular hydrogen peaks reported in the literature [50] (both in air wavelengths).

Branch	Literature Wavelength (Å)	Reported Intensity	Observed KNO_3 rt-plasma Intensity	Hydrogen Microwave Plasma Intensity
Q_1	4027.789	0.3	no peak	observed
Q_2	4046.201	0.4	no peak	observed (weak)
Q_3	4058.854	0	no peak	
Q_4	4071.666	1.07	strong peak assigned to $H^-(1/2)$	observed
Q_5	4085.336	0.7	no peak	observed (most intense peak in this region)
Q_6	4099.481	0.2	no peak	observed

Table 8C. A comparison of the rt-plasma peaks with the $^3\Delta_{v=3}\rightarrow{}^3\Pi_{v=2}$ $(4f3\rightarrow2C2)$ molecular hydrogen peaks reported in the literature [50] (both in air wavelengths).

Branch	Literature Wavelength ($\mathring{A}$)	Reported Intensity	Observed KNO_3 rt-plasma Intensity	Hydrogen Microwave Plasma Intensity
R_1	4087.281	0.4	no peak	observed
R_2	4071.565	0.2	strong peak assigned to $H^-(1/2)$	observed

Table 9. The numerical results of the deconvolution analysis of the hyperfine $H^-(1/2)$ peak at 4071 Å.

Air Wavelength of Curve Fit Peak (Å)	Energy of Curve Fit Peak (eV)	Energy Difference Between Adjacent Peaks
4071.06	3.044666	3.07E-04
4071.47	3.044360	3.66E-04
4071.96	3.043993	

Table 10. The experimental (air wavelengths) and literature (air wavelengths) of nitrogen [53] and nitrogen molecular ion [54-55] vibration-rotational band heads in the region of 3850-4100 Å.

Band Head	Observed Wavelength (Å)	Literature Wavelength (Å)	Difference Between Observed and Literature (Å)
$N_2^+\ B^2\Sigma_u^+ - X^2\Sigma_u^+\ (\upsilon' = 0 - \upsilon'' = 0)$	3914.4	3914.4	0.0
$N_2\ C^3\Pi_u - B^3\Pi_g\ (\upsilon' = 2 - \upsilon'' = 5)$	3943.0	3943.0	0.0
$N_2\ C^3\Pi_u - B^3\Pi_g\ (\upsilon' = 1 - \upsilon'' = 4)$	3998.4	3998.4	0.0
$N_2\ C^3\Pi_u - B^3\Pi_g\ (\upsilon' = 0 - \upsilon'' = 3)$	4059.4	4059.4	0.0
$N_2\ C^3\Pi_u - B^3\Pi_g\ (\upsilon' = 4 - \upsilon'' = 8)$	4094.8	4094.8	0.0

Table 11. The numerical results of the deconvolution analysis of the $j = 34$ $H^-(1/2)$ bound-free hyperfine peak recorded on the $RbNO_3$ rt-plasma.

Air Wavelength of Curve Fit Peak (Å)	Energy of Curve Fit Peak (eV)	Energy Difference Between Adjacent Peaks
4006.99	3.093346	3.50E-04
4007.45	3.092996	2.18E-04
4007.73	3.092777	

Figure Captions

Figure 1. The experimental set up comprising a filament gas cell to form an rt-plasma light source and an VUV spectrometer which was differentially pumped.

Figure 2. The 6563 Å Balmer α line width recorded with a high resolution (± 0.06 Å) visible spectrometer on an rt-plasma formed with K and K^+/K^+ catalysts. Significant broadening was observed corresponding to an average hydrogen atom temperature of 18 eV compared $\approx 3\,eV$ for a hydrogen microwave discharge plasma.

Figure 3. The statistical curve fits of the 6563 Å Balmer α line width recorded with a high resolution (± 0.06 Å) visible spectrometer on an rt-plasma formed with Rb^+ catalyst and a hydrogen microwave plasma. The $RbNO_3$ rt-plasma data matched a Gaussian profile having the

$$X^2 = \sum \frac{(\text{Calculated} - \text{Measured})^2}{\text{Calculated}}$$ and R^2 (correlation coefficient squared) values of 0.00023 and 0.99908, respectively. Significant broadening was observed corresponding to an average hydrogen atom temperature of 12 eV. The data of the hydrogen microwave plasma matched a Gaussian profile having the X^2 and R^2 values of 0.00092 and 0.98937, respectively. No broadening was observed corresponding to an average hydrogen atom temperature of 3 eV.

Figure 4. The 6563 Å Balmer α line width recorded with a high resolution (± 0.06 Å) visible spectrometer on an rt-plasma formed with Cs catalyst. Significant broadening was observed corresponding to an average hydrogen atom temperature of 12 eV.

Figure 5. The probe current versus voltage trace of the Langmuir probe of the $RbNO_3$ rt-plasma. The electron density and temperature were measured to be $n_e = 2 \times 10^9\,cm^{-3}$ and $T_e = 1 - 2\,eV$. The electron density was over six orders of magnitude less than that required to achieve 1 Å electron Stark broadening.

Figure 6. The VUV spectrum (450 – 800 Å) of the cell emission recorded at about the point of the maximum Lyman α emission from a gas cell at a cell temperature of 700 °C comprising a tungsten filament, a titanium dissociator, 300 mtorr hydrogen, and vaporized K and K^+ from KNO_3 that was recorded with a CEM. Line emission corresponding to K^{3-}

1

was observed at 650-670 Å and 740-760 Å. K^{2+} was observed at 510 Å and 550 Å, and K^+ was observed at 620 Å.

Figure 7. The VUV spectrum (500-900 Å) of the emission of the $RbNO_3-H_2$ gas cell (top curve) and the standard rubidium plasma (bottom curve). The $RbNO_3-H_2$ gas cell comprised a tungsten filament, a titanium dissociator, 300 mTorr hydrogen, and vaporized Rb^+ from $RbNO_3$. The emission was recorded with a CEM at about the point of the maximum Lyman α at a cell temperature of 700 °C. Line emission corresponding to Rb^{2+} was observed at 815.9 Å, 591 Å, 581 Å, 556 Å, and 533 Å. Rb^+ was observed at 741.5 Å, 711 Å, 697 Å, and 643.8 Å.

Figure 8. The UV spectrum (3400-4150 Å) the cell emission recorded at about the point of the maximum Lyman α emission from a gas cell at a cell temperature of 700 °C comprising a tungsten filament, a titanium dissociator, 300 mtorr hydrogen, and vaporized Cs from $CsNO_3$ that was recorded with a photomultiplier tube (PMT) and a sodium salicylate scintillator. Line emission corresponding to Cs^{2+} was observed at 3477 Å, 3618 Å, and 4001 Å. Cs^+ was observed at 3680 Å, 3806 Å, and 4069 Å. Cs was observed at 3888 Å.

Figure 9. The VUV spectrum (400-800 Å) of the cell emission from the gas cell at a cell temperature of 700 °C comprising a tungsten filament, vaporized cesium metal, and 300 mtorr hydrogen that was recorded with a PMT and a sodium salicylate scintillator. Emission was observed from a continuum state of Cs^{2+} at 533 Å. The single emission feature with the absence of the other corresponding Rydberg series of lines from Cs^+ confirmed the resonant energy transfer of $27.2\,eV$ from atomic hydrogen to atomic cesium.

Figure 10. The VUV spectra (900-1300 Å) of the cell emission from hydrogen microwave plasma (dotted line) and the KNO_3-H_2 rt-plasma (solid line) with an inverted Lyman population.

Figure 11. The VUV spectra (900-1300 Å) of the cell emission from hydrogen microwave plasma (dotted line) and the $RbNO_3-H_2$ rt-plasma (solid line) with an inverted Lyman population.

Figure 12. The VUV spectra (900-1300 Å) of the cell emission from hydrogen microwave plasma (dotted line) and the $CsNO_3-H_2$ rt-plasma (solid line) with no inverted Lyman population.

Figure 13. The relative Balmer α, β, γ, and δ line intensities

2

corresponding to n=3, n=4, n=5, and n=6 recorded on a hydrogen microwave plasma.

Figure 14. The relative Balmer α, β, γ, and δ line intensities corresponding to n=3, n=4, n=5, and n=6 recorded on a KNO_3 rt-plasma.

Figure 15. The relative Balmer α, β, γ, and δ line intensities corresponding to n=3, n=4, n=5, and n=6 recorded on a $RbNO_3$ rt-plasma.

Figure 16. A plot of the absolute reduced population density $\dfrac{N_n}{g_n}$ versus quantum number n recorded on a hydrogen microwave plasma, a $RbNO_3$ rt-plasma, and a KNO_3 rt-plasma. In the case of KNO_3 and $RbNO_3$ rt-plasmas, population inversion was observed for n=3. From standard laser cavity equations and a collisional-radiative model, an overpopulation was achieved for n=3 .

Figure 17. The high resolution visible spectrum in the region of 4000 Å to 4060 Å recorded on the emission of a control hydrogen microwave discharge plasma.

Figure 18. The high resolution visible spectrum in the region of 4060 Å to 4090 Å recorded on the emission of a control hydrogen microwave discharge plasma.

Figure 19. The high resolution visible spectrum in the region of 4000 Å to 4090 Å recorded on the emission of a rt-plasma formed with K^- / K^+ catalyst from vaporized KNO_3. The $H^-(1/2)$ hydride ion with a predicted binding energy of $3.0468\,eV$ was observed with the fine structure transition as a structured peak at 4071 Å. An observed inverse Rydberg-type series of broad emission lines that converged at increasing wavelengths and terminated at about $3.0563\,eV$—the hydride binding energy with the fine structure plus the spin-pairing energy—matched the theoretical bound-free hyperfine energies E_{HF} given by $E_{HF} = j^2 3.00213 \, X \, 10^{-5} + 3.0563\,eV$ for $j = 1$ to $j = 37$ as given in Table 7. Other peaks in the rt-plasma that partially covered some of the bound-free hyperfine peaks were assigned to K I and molecular hydrogen.

Figure 20. The 4000 Å to 4060 Å region of the Figure 19 spectrum to show an expanded view of the $H^-(1/2)$ emission bound-free hyperfine lines. Other peaks in the rt-plasma that partially covered some of the bound-free hyperfine peaks were assigned to K I and molecular hydrogen.

3

Figure 21. The 4060 Å to 4090 Å region of the Figure 19 spectrum to show an expanded view of the $H^-(1/2)$ binding energy emission. Other peaks in the rt-plasma were assigned to molecular hydrogen. The rt-plasma peaks which matched hydrogen were broadened due to excitation by the hydride ion continuum emission. A unique linear intensity profile was reproducibly observed.

Figure 22. The energy level diagram for the free-free and bound-free transitions corresponding to $H(1/2p)\left[^2P_{3/2}\right] + e^- \rightarrow H^-\left(1/2s^2\right)\left[^1S_0\right]$ given in Tables 6 and 7, respectively. E_B is the binding energy of $H(1/2) + e^- \rightarrow H^-(1/2)$ given by Eqs. (13) and (14). Compared to the typical continuum emission of the free-free and bound-free transitions, the coupling of the binding electron with the $\ell = 1$ state of $H(1/2)$ to excite the state $H(1/2)\left[^2P_{3/2}\right]$ lowers the binding electron's free-free levels by $\left(qE_{s/o} + \Delta E_{total}^{S/N O/N}\right)$ (Eqs. (16), (18), (22), and (23)) and bound-free levels by $\left(E_{s/o} + \Delta E_{total}^{S/N O/N}\right)$ with an increase in the emission cross section. Hyperfine transitions due to $\Delta E_{total}^{S/N O/N}$ split the upper levels, but the magnitude is relatively small. The bound-free levels are $E_{ss} + E_\Phi$ above the first free-free level where E_{ss} and E_Φ are given by Eqs. (15) and (14).

Figure 23. The 4068 Å to 4073 Å region of the Figure 21 spectrum to show an expanded view of the hyperfine structure of the $H^-(1/2)$ peak. The results of the deconvolution analysis of the 4071 Å peak fit three peaks very well. The deconvolved peaks were separated by energies that were a good match to the hyperfine splitting of $H(1/2)$.

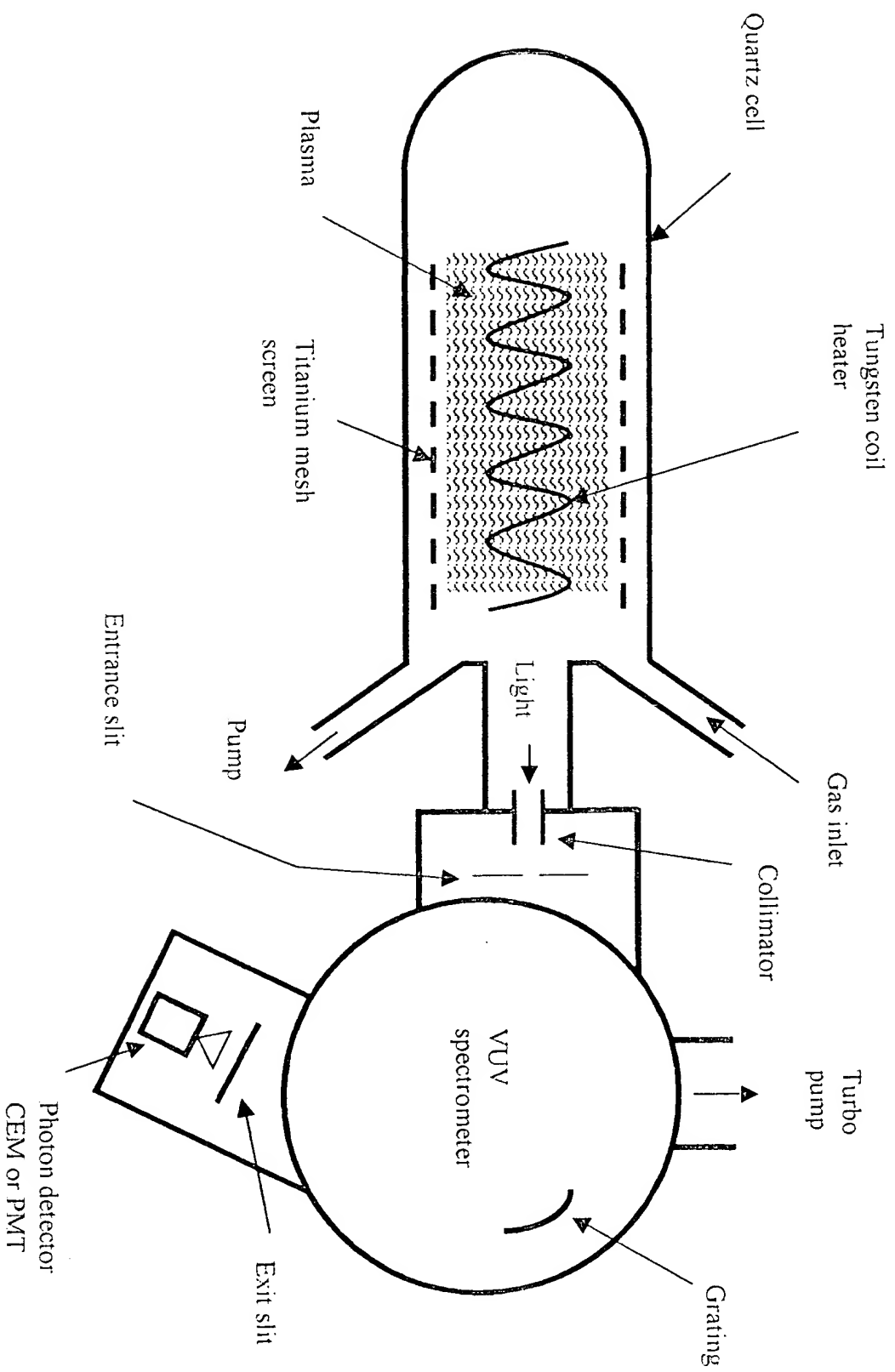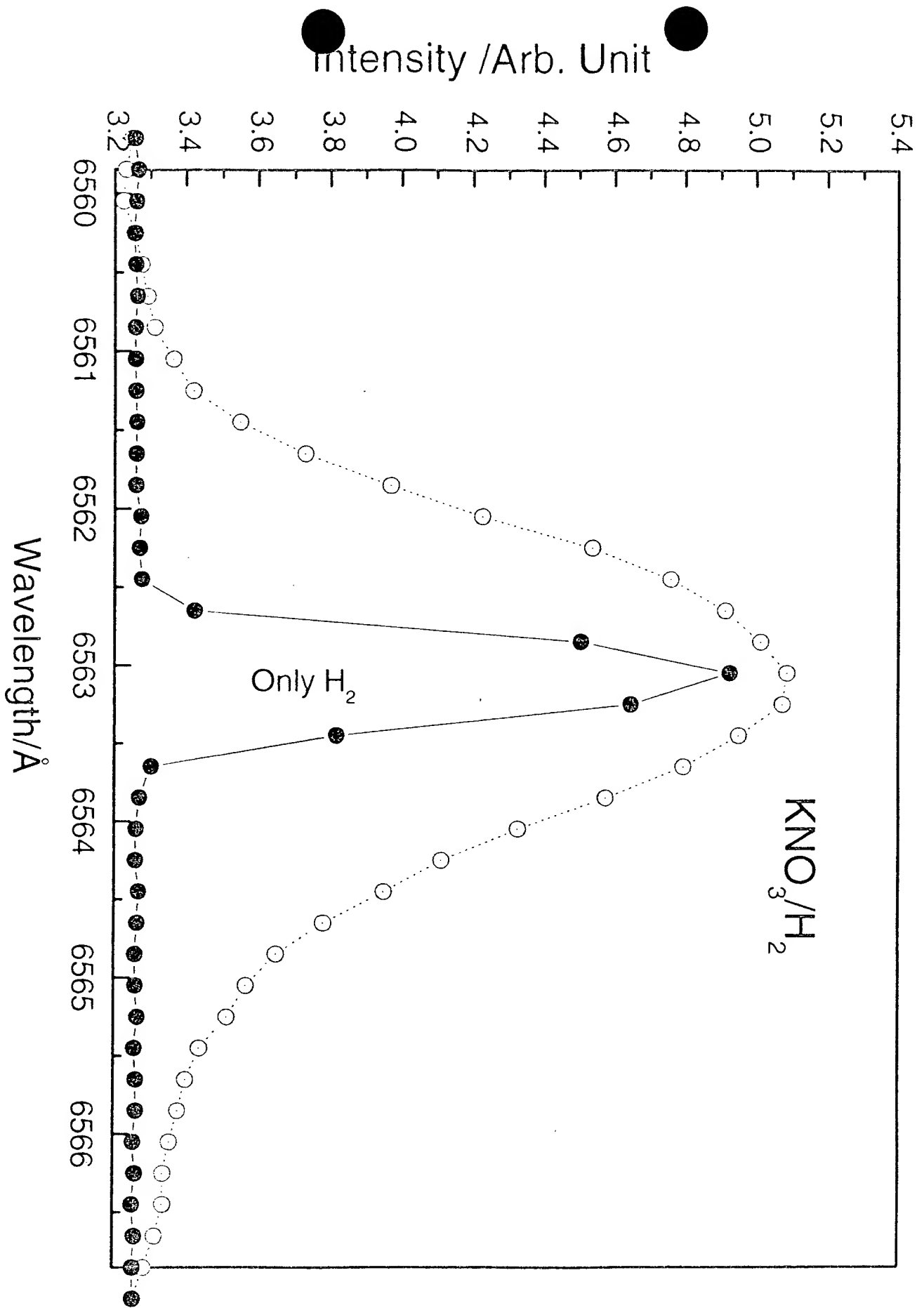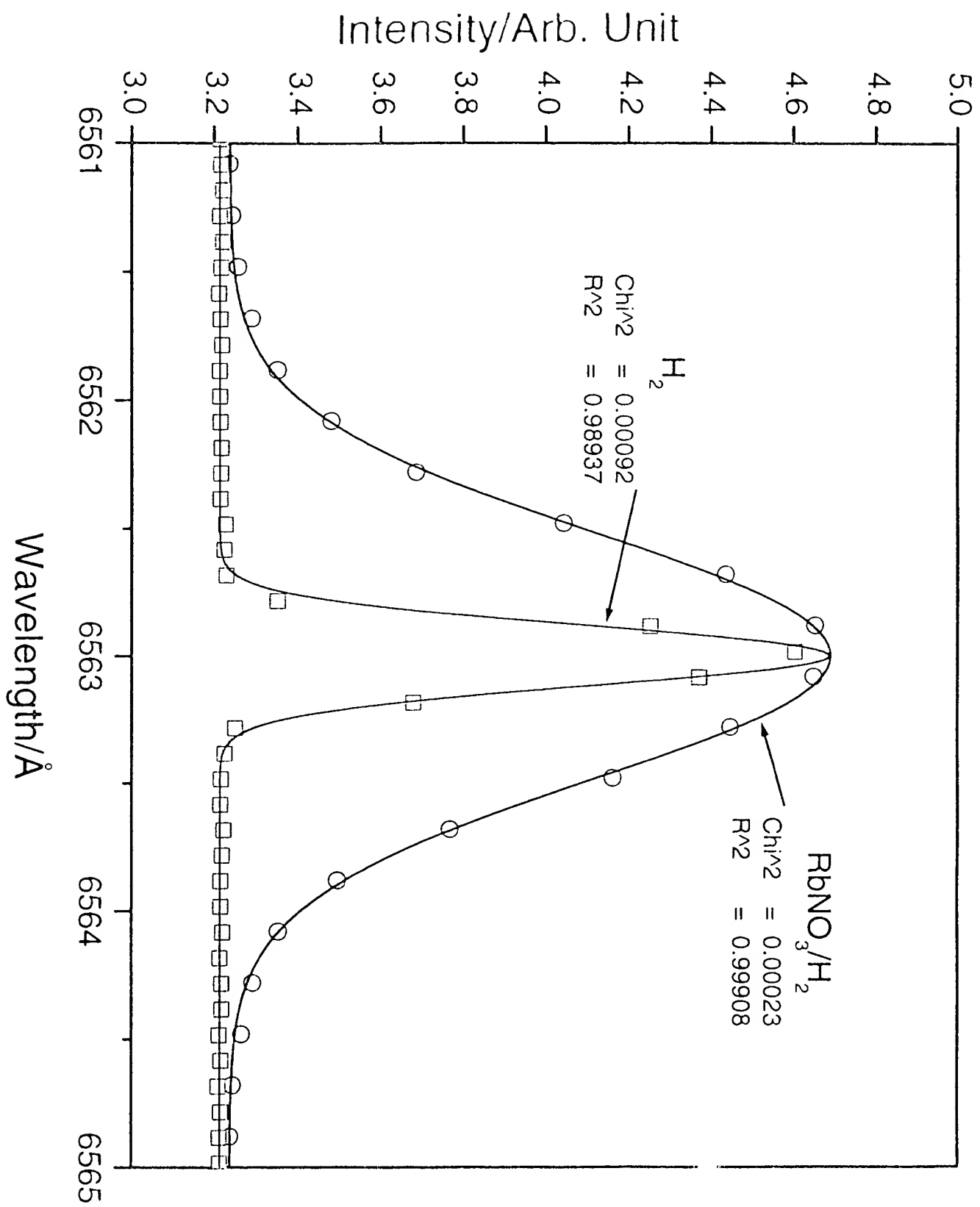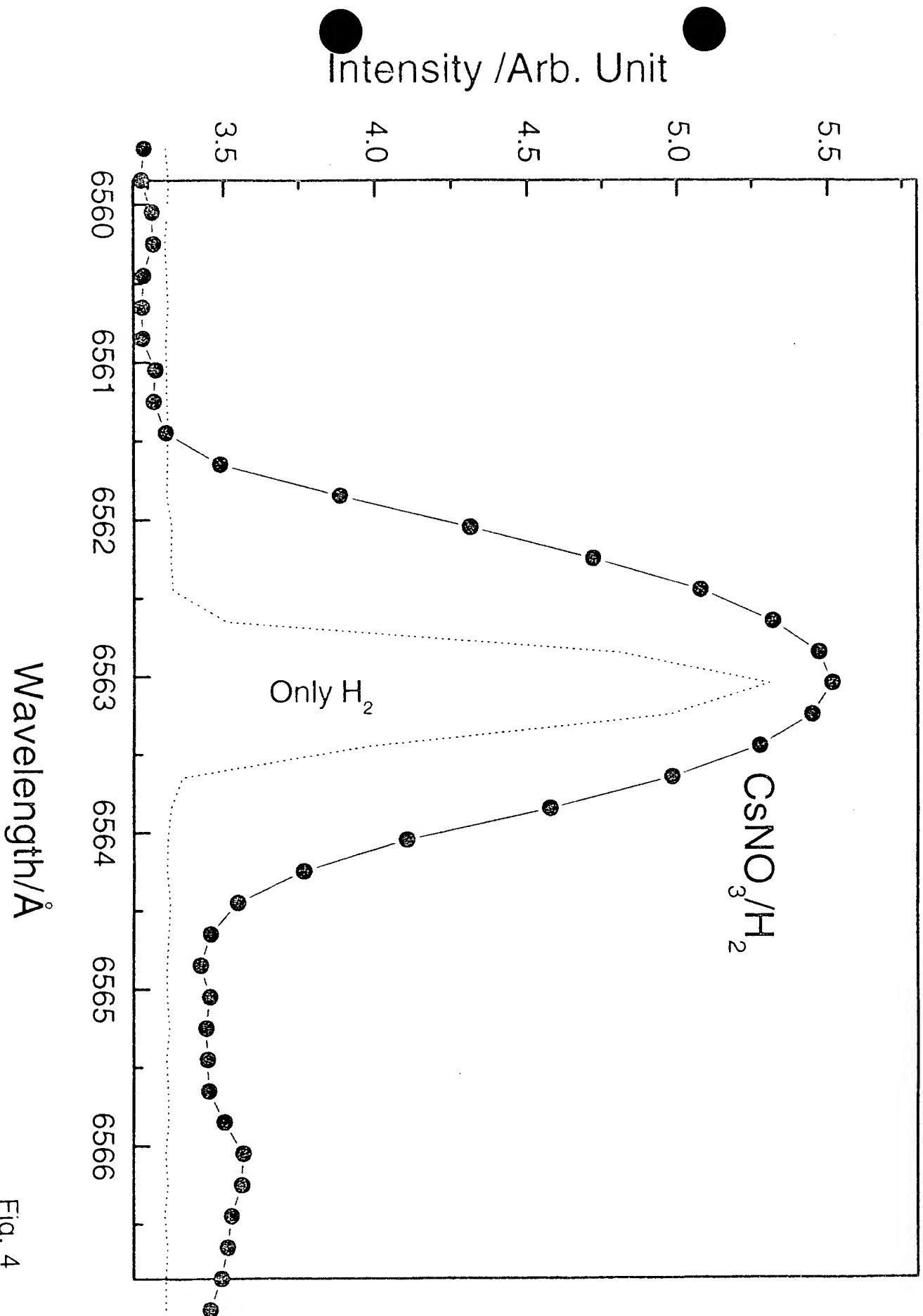Figure 24. The overlay of the high resolution visible spectrum in the region of 4060 Å to 4090 Å recorded on the emission of the KNO_3 rt-plasma and the control hydrogen microwave discharge plasma. The peaks at 4071 Å, 4075.9 Å, 4078.9 Å, and 4083.6 Å could not be assigned to hydrogen based on intensity and the absence of required corresponding branches of the known transitions at these wavelengths according to Crosswhite [77].

Figure 25. The overlay of the wavelength-calibrated spectra (3900-4090 Å) of the KNO_3 rt-plasma and a nitrogen microwave plasma. The wavelengths of the spectral lines do not match, and the additional vibration-rotational band heads of nitrogen are not observed in the rt-plasma which eliminates nitrogen as the source of the emission recorded

4

on the rt-plasma.

Figure 26. The overlay of the high resolution visible spectrum in the region of 3900 Å to 4090 Å recorded on the emission of the KNO_3 rt-plasma and a control hydrogen microwave discharge plasma. The hydrogen molecular peaks matched those of the rt-plasma in the region 3900 to 3995 wherein the rt-plasma peaks were broadened due to excitation by the hydride ion continuum emission. The novel series of 39 lines was not observed in the hydrogen spectrum.

Figure 27. The high resolution visible spectrum in the region of 3995 Å to 4060 Å recorded on the emission of a rt-plasma formed with K^-/K^+ catalyst from vaporized KNO_3 with the K I peaks at 4044.142 Å and 4047.213 Å which confirmed the calibration. An observed inverse Rydberg-type series from 3.0563 eV to 3.1012 eV—the hydride binding energy with the fine structure plus one and five times the spin-pairing energy, respectively—matched the theoretical bound-free hyperfine energies E_{HF} given by $E_{HF} = j^2 3.00213 \times 10^{-5} + 3.0563\,eV$ for $j = 1$ to $j = 39$ as given in Table 7.

Figure 28. The high resolution visible spectrum in the region of 4000 Å to 4090 Å recorded on the emission of a rt-plasma formed with Rb^- catalyst from vaporized $RbNO_3$. The $H^-(1/2)$ hydride ion with a predicted binding energy of $3.0468\,eV$ was observed with the fine structure transition as a structured peak at 4071 Å. An observed inverse Rydberg-type series of broad emission lines that converged at increasing wavelengths and terminated at about $3.0563\,eV$—the hydride binding energy with the fine structure plus the spin-pairing energy—matched the theoretical bound-free hyperfine energies E_{HF} given by $E_{HF} = j^2 3.00213 \times 10^{-5} + 3.0563\,eV$ for $j = 1$ to $j = 37$ as given in Table 7. Other peaks in the rt-plasma were assigned to molecular hydrogen.

Figure 29. The 4000 Å to 4060 Å region of the Figure 28 spectrum to show an expanded view of the $H^-(1/2)$ emission bound-free hyperfine lines. Other peaks in the rt-plasma were assigned to molecular hydrogen.

Figure 30. The 4060 Å to 4090 Å region of the Figure 28 spectrum to show an expanded view of the $H^-(1/2)$ binding energy emission. Other peaks in the rt-plasma were assigned to Rb II and molecular hydrogen.

Figure 31. The overlay of the 4000 Å to 4060 Å region of the KNO_3 and $RbNO_3$ rt-plasmas which shows the good match between the $H^-(1/2)$

bound-free hyperfine lines from the two sources.

Figure 32. The overlay of the 4060 Å to 4090 Å region of the KNO_3 and $RbNO_3$ rt-plasmas which shows the good match between the $H^-(1/2)$ peak and the peaks at 4072.0, 4075.9, 4078.9, 4079.8, 4081.7, and 4083.6 Å from the two sources.

Figure 33. The three matching VUV spectra (4000-4090 Å) of Rb^+ rt-plasmas that were equivalent to the spectrum shown in Figure 28.

Figure 34. The 4000 Å to 4060 Å region of the Figure 33 spectrum to show an expanded view of the split $H^-(1/2)$ bound-free hyperfine lines. Other peaks in the rt-plasma were assigned to molecular hydrogen.

Figure 35. The plot of the theoretical bound-free hyperfine air wavelengths corresponding to energies E_{HF} given by $E_{HF} = j^2 3.00213 \, X \, 10^{-5} + 3.0563 \, eV$ (Eq. (19)) for $j = 1$ to $j = 38$ and the wavelengths observed for the inverse Rydberg-type series of broad emission lines shown in Figures 19, 27, and 28 and given in Table 7. The agreement was remarkable.

Figure 36. The 4009 Å to 4011 Å region of the Figure 28 spectrum to show an expanded view of the $j = 34$ $H^-(1/2)$ bound-free hyperfine peak. The results of the deconvolution analysis fit three peaks very well. The deconvolved peaks were separated by energies that were a good match to the hyperfine splitting of $H(1/2)$.

6

Quartz cell

Plasma

Titanium mesh screen

Tungsten coil heater

Entrance slit

Light

Pump

Gas inlet

Collimator

VUV spectrometer

Turbo pump

Photon detector CEM or PMT

Exit slit

Grating

Fig. 1
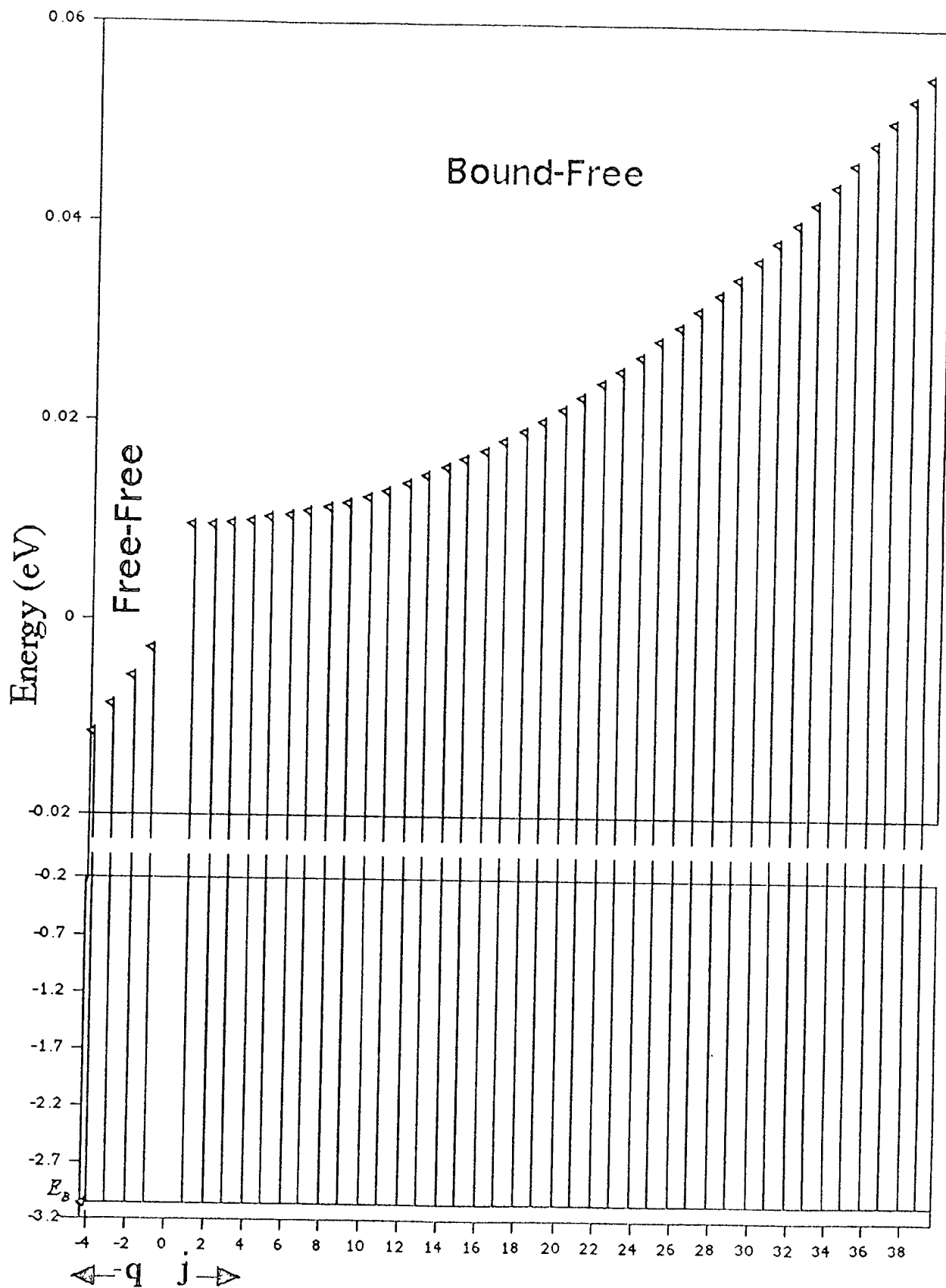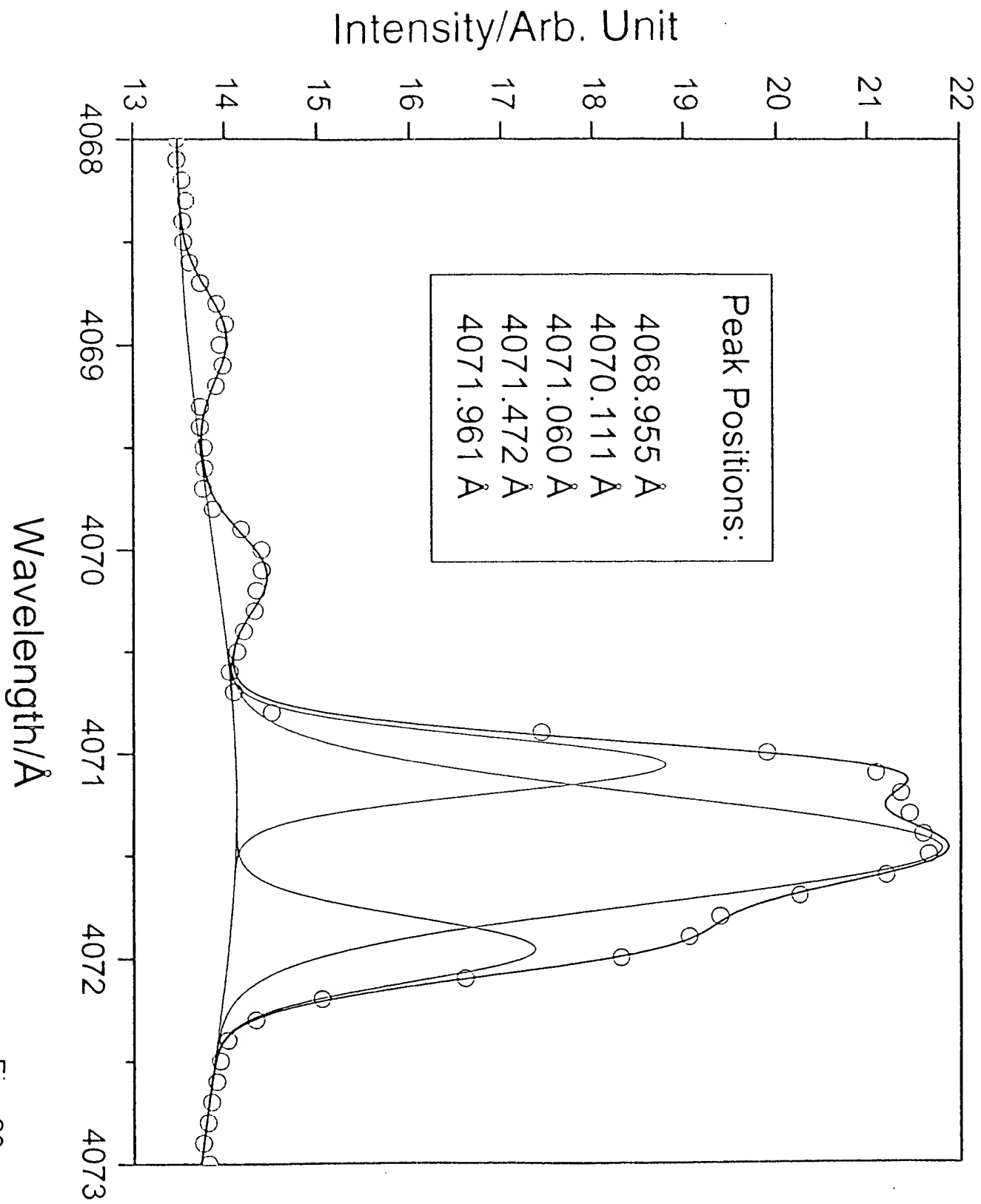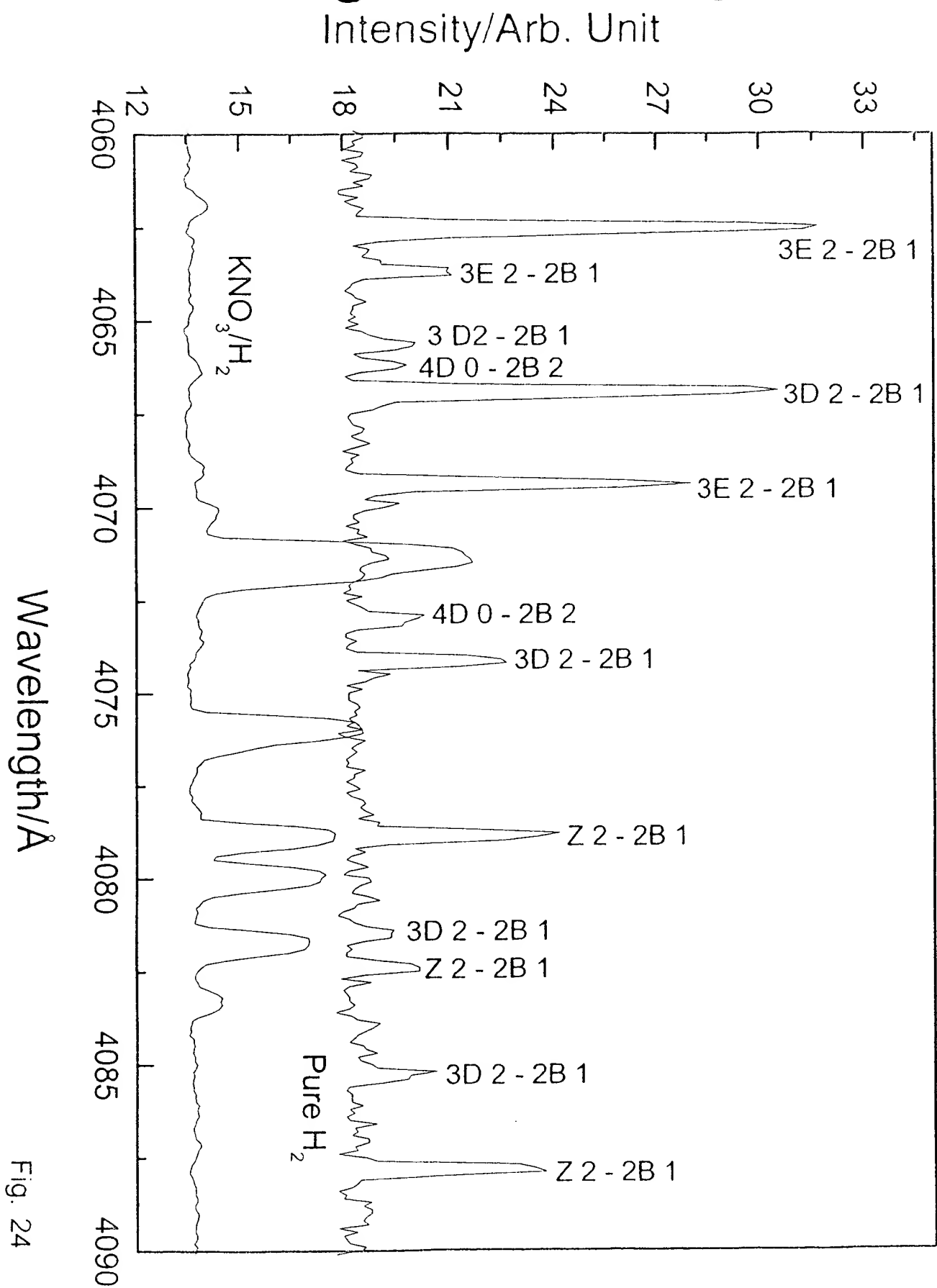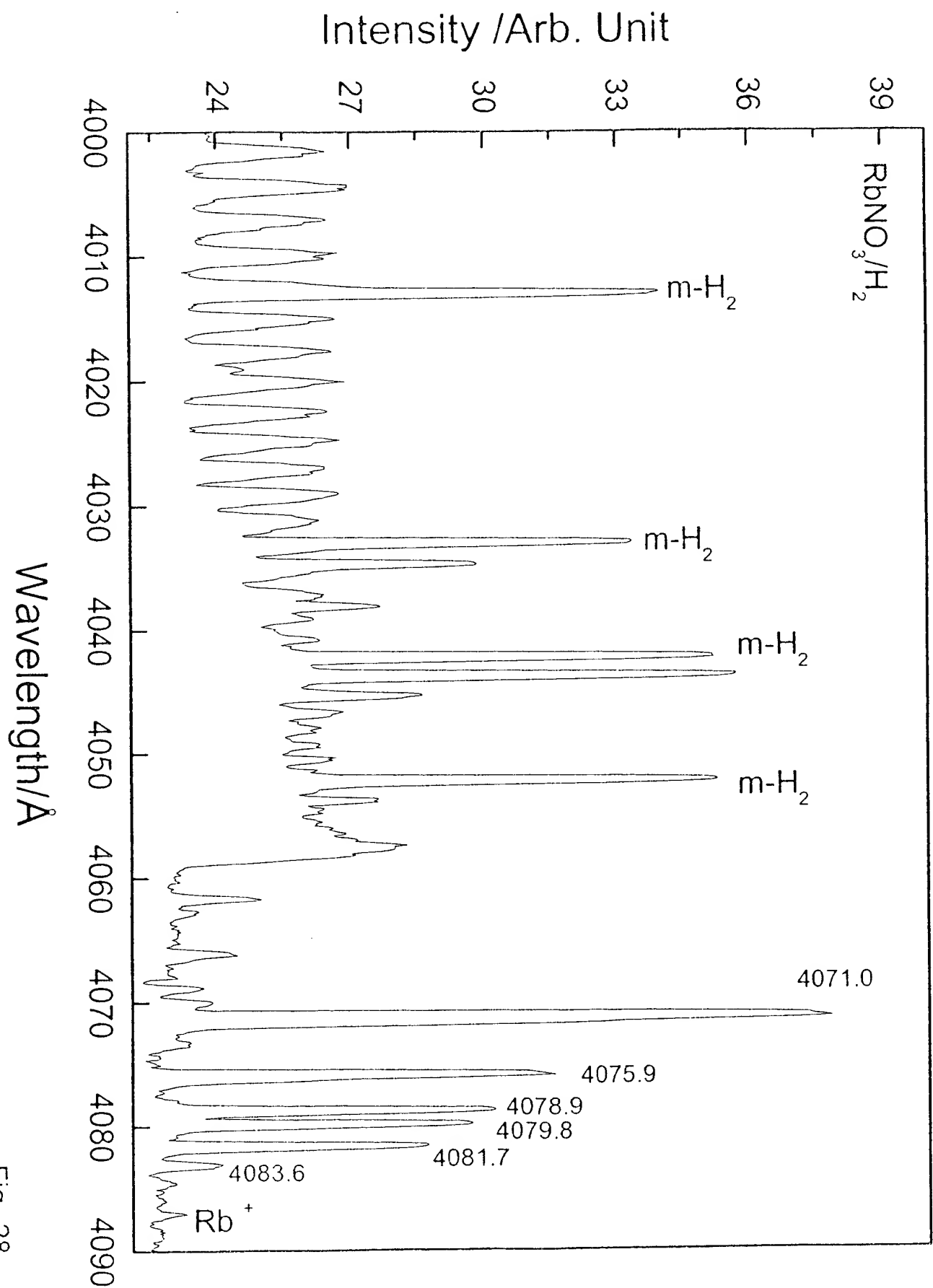
Fig. 2

Fig. 3

Fig. 4

Fig. 5

Fig. 6

Fig. 7

Photon Counts/sec

RbNO$_3$/H$_2$
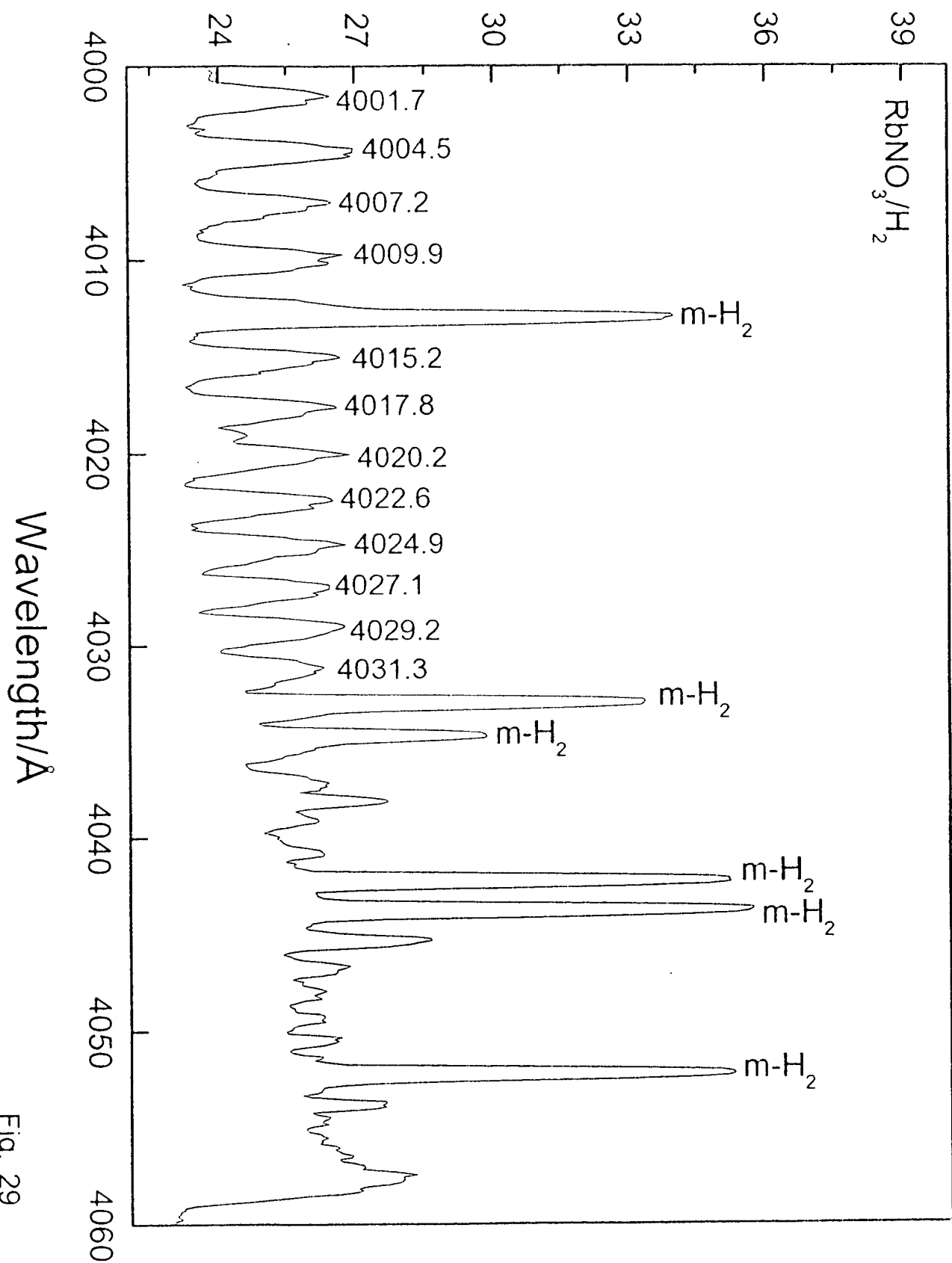
Rb^{2+}
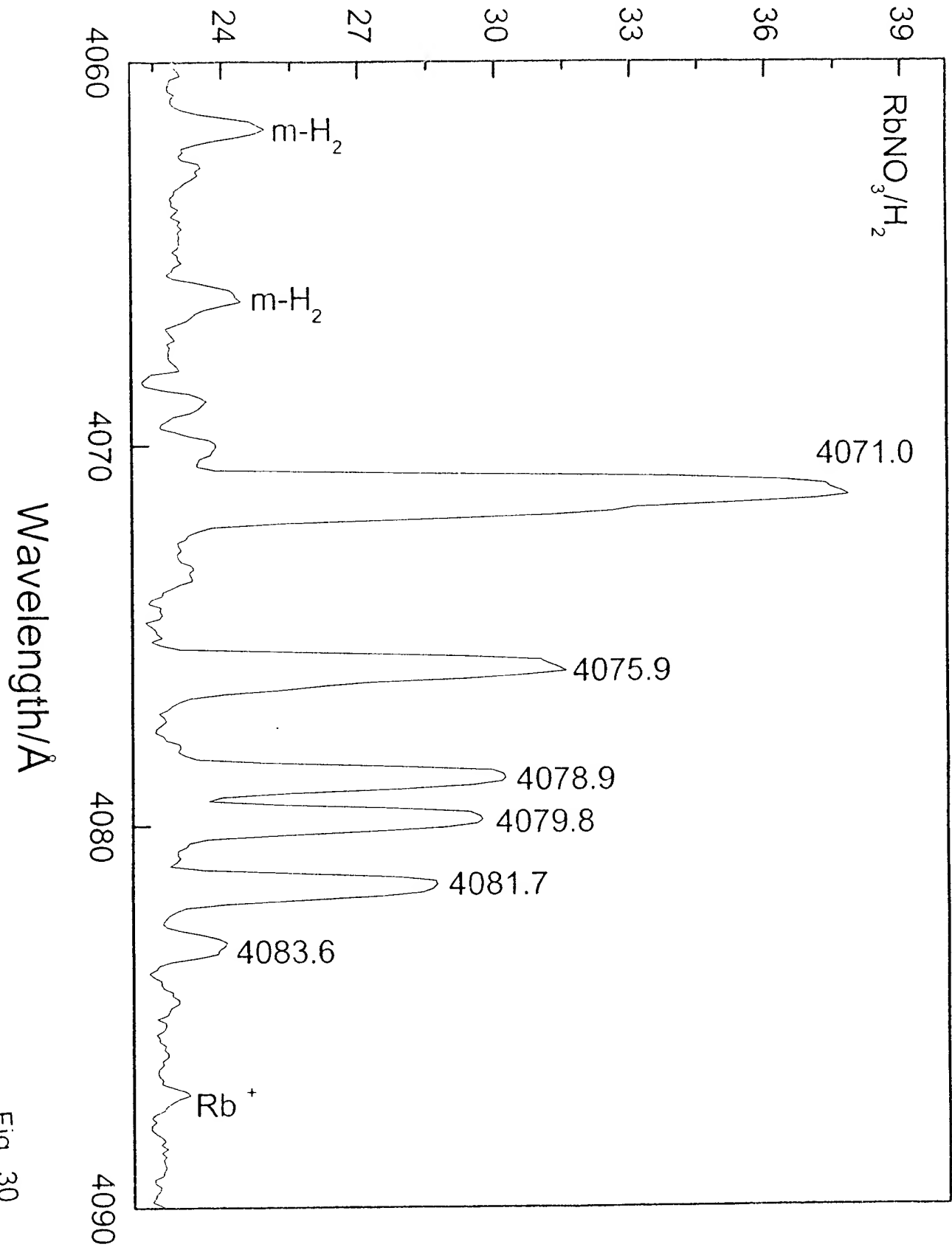Rb$^+$
Rb^{2+}
Rb^{2+}
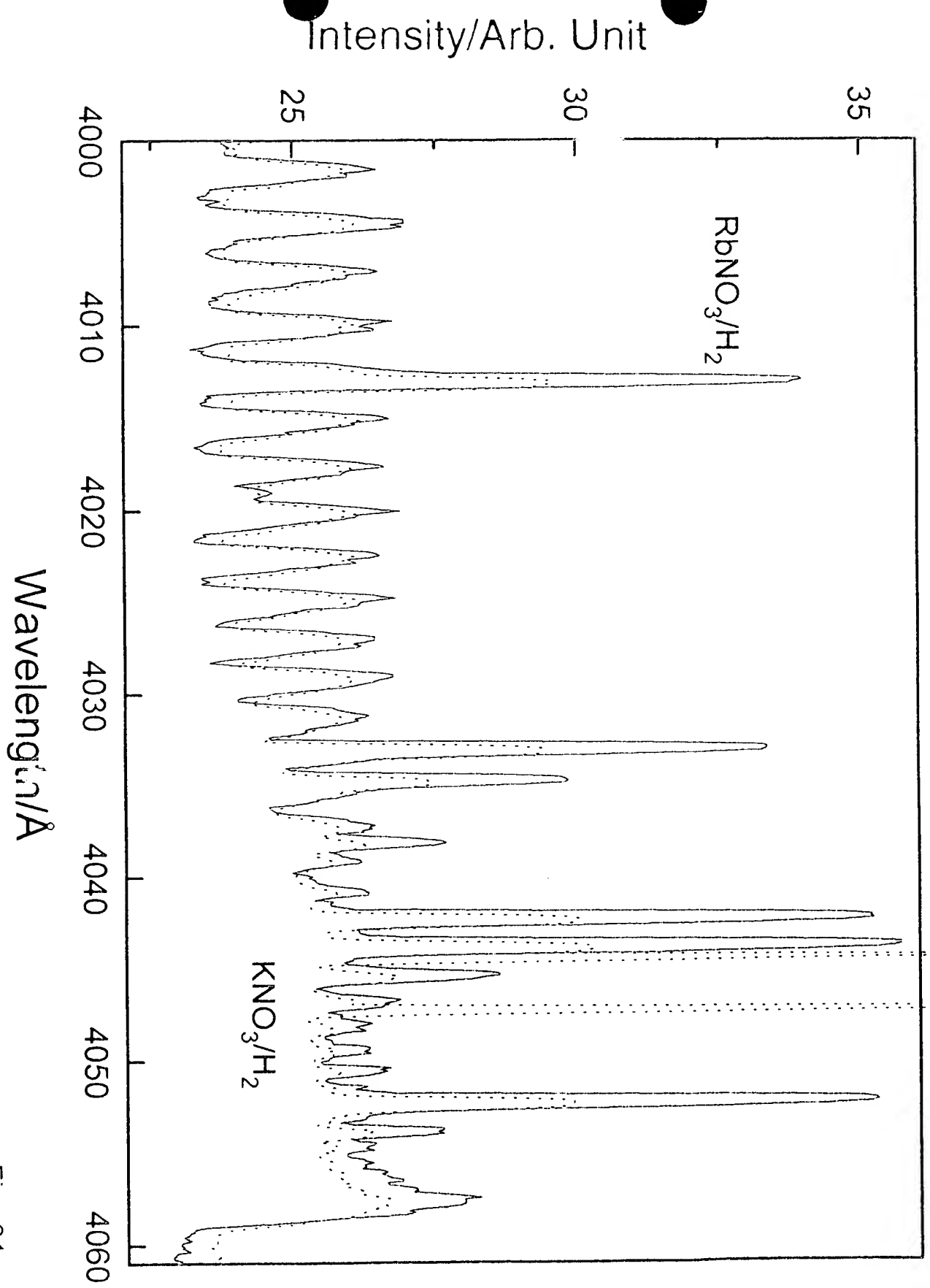Rb$^+$
Rb$^+$
Rb$^+$
Rb$^+$
Rb^{2+}

Wavelength/Å
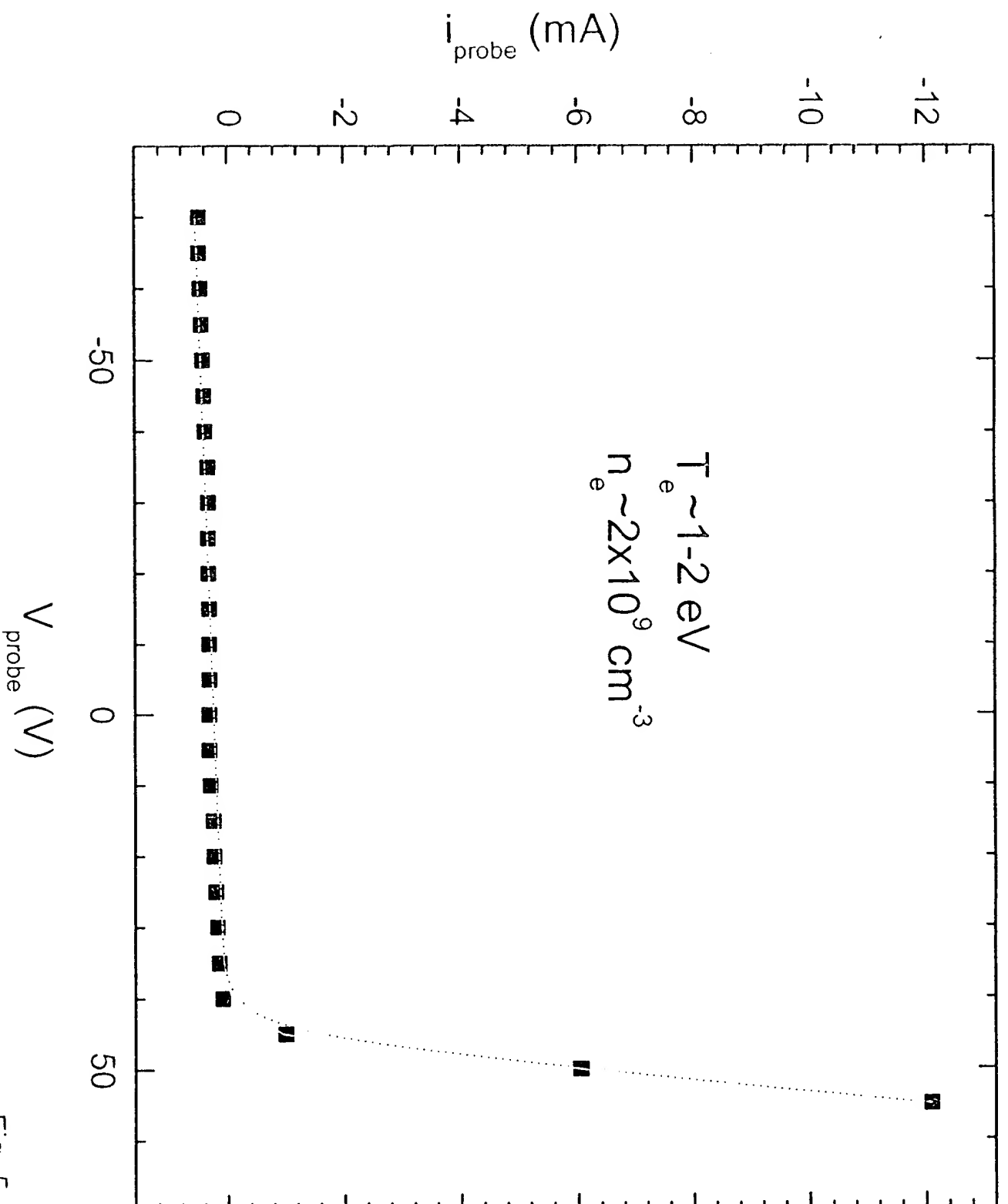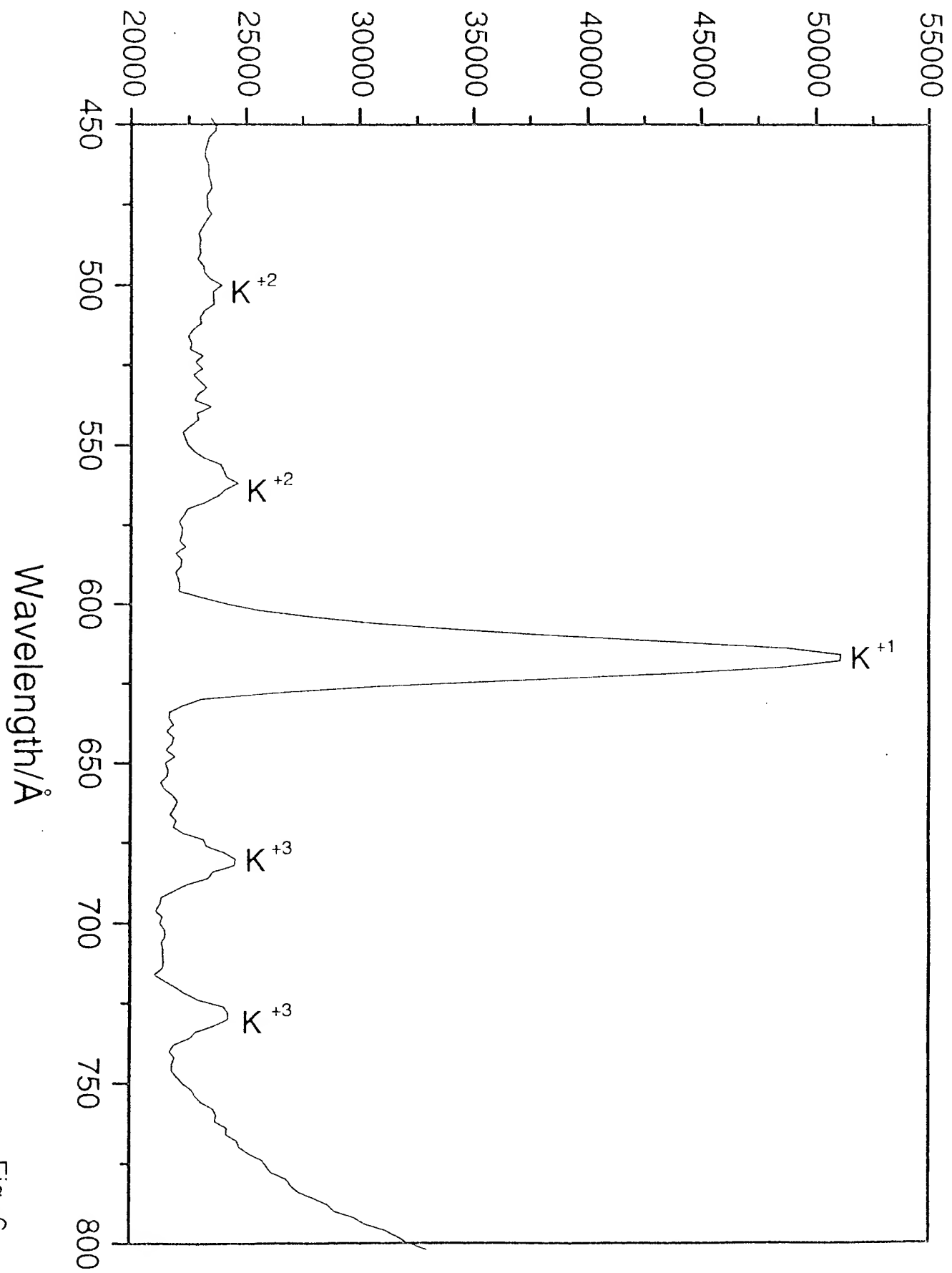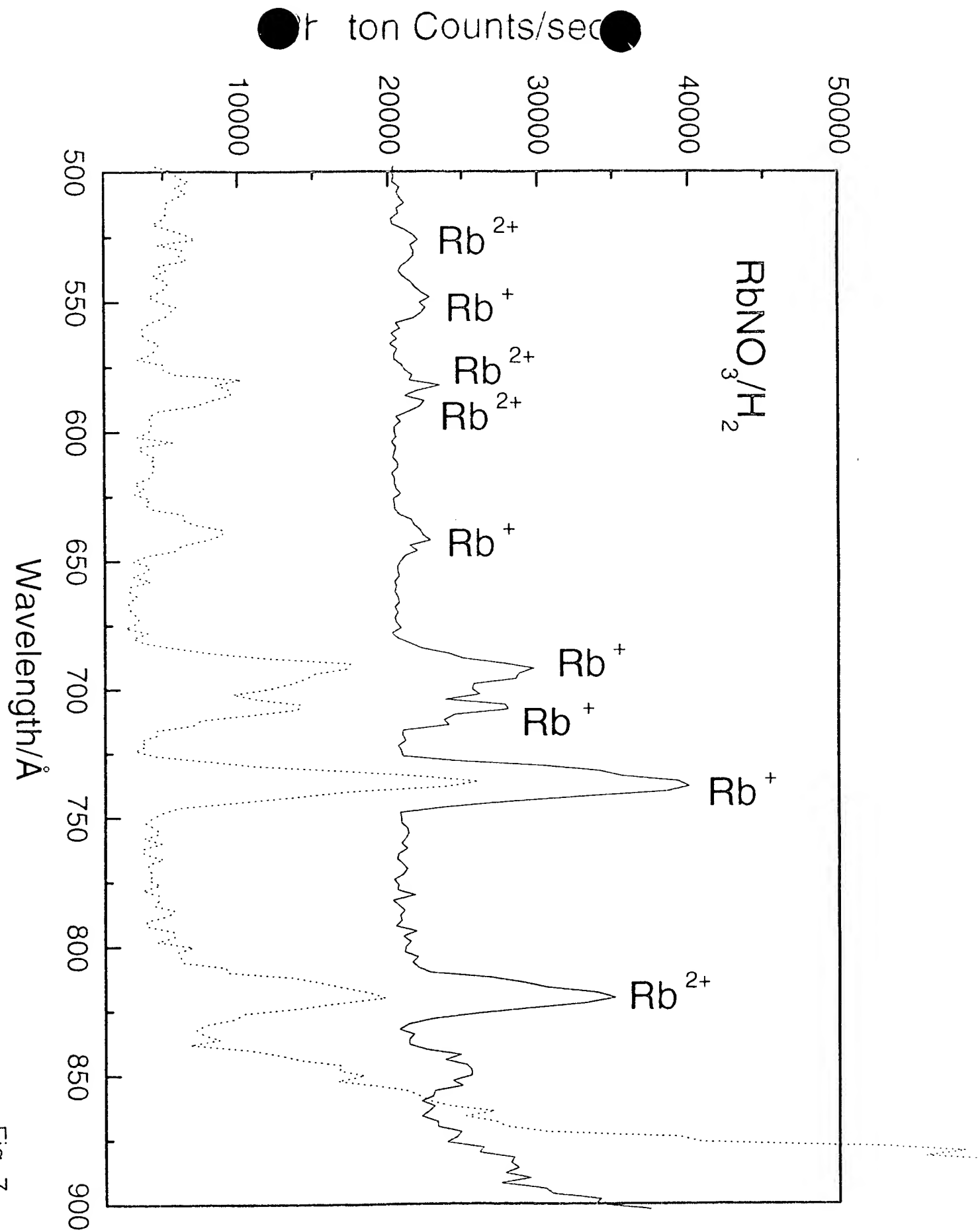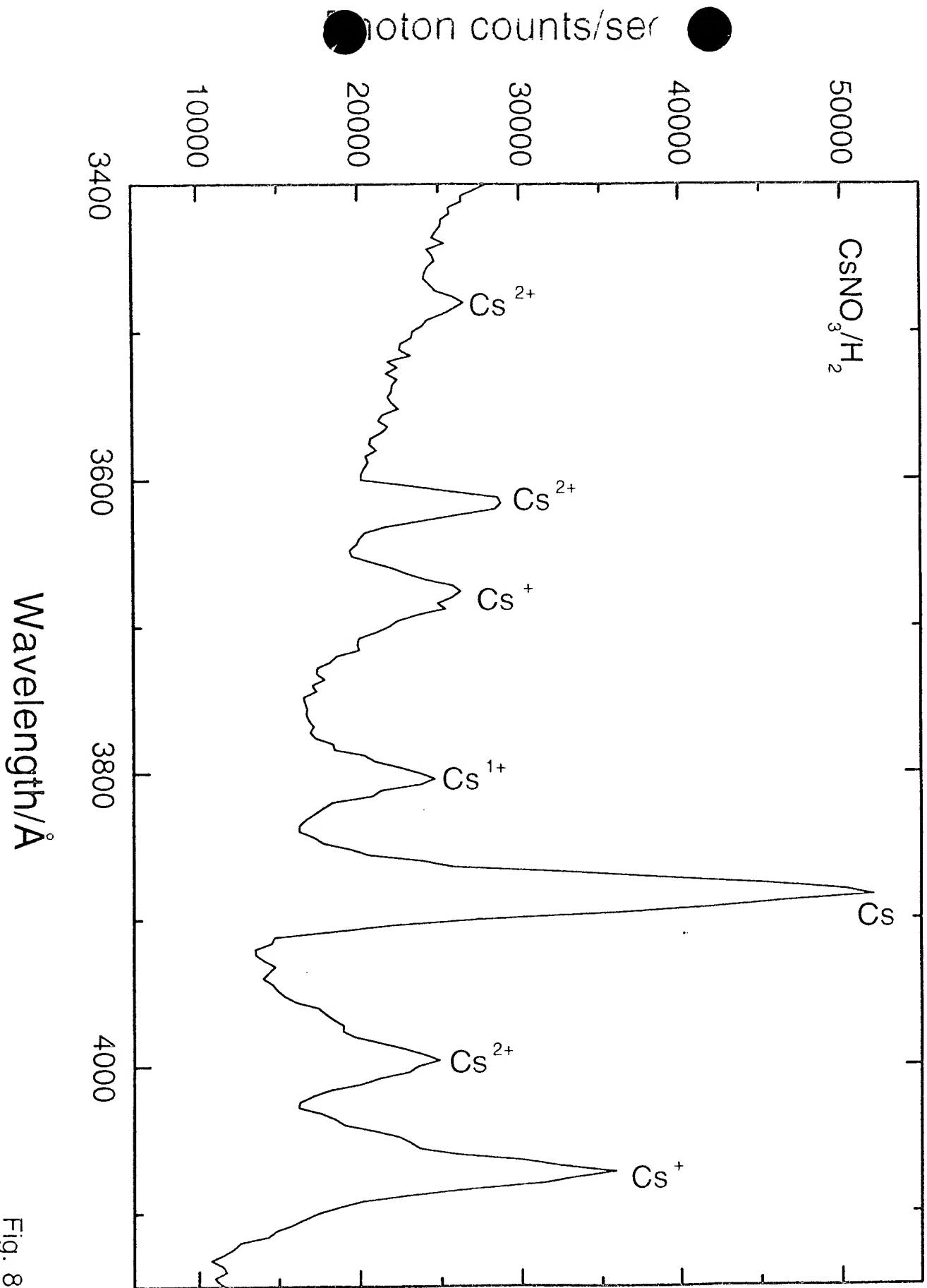
Fig. 8
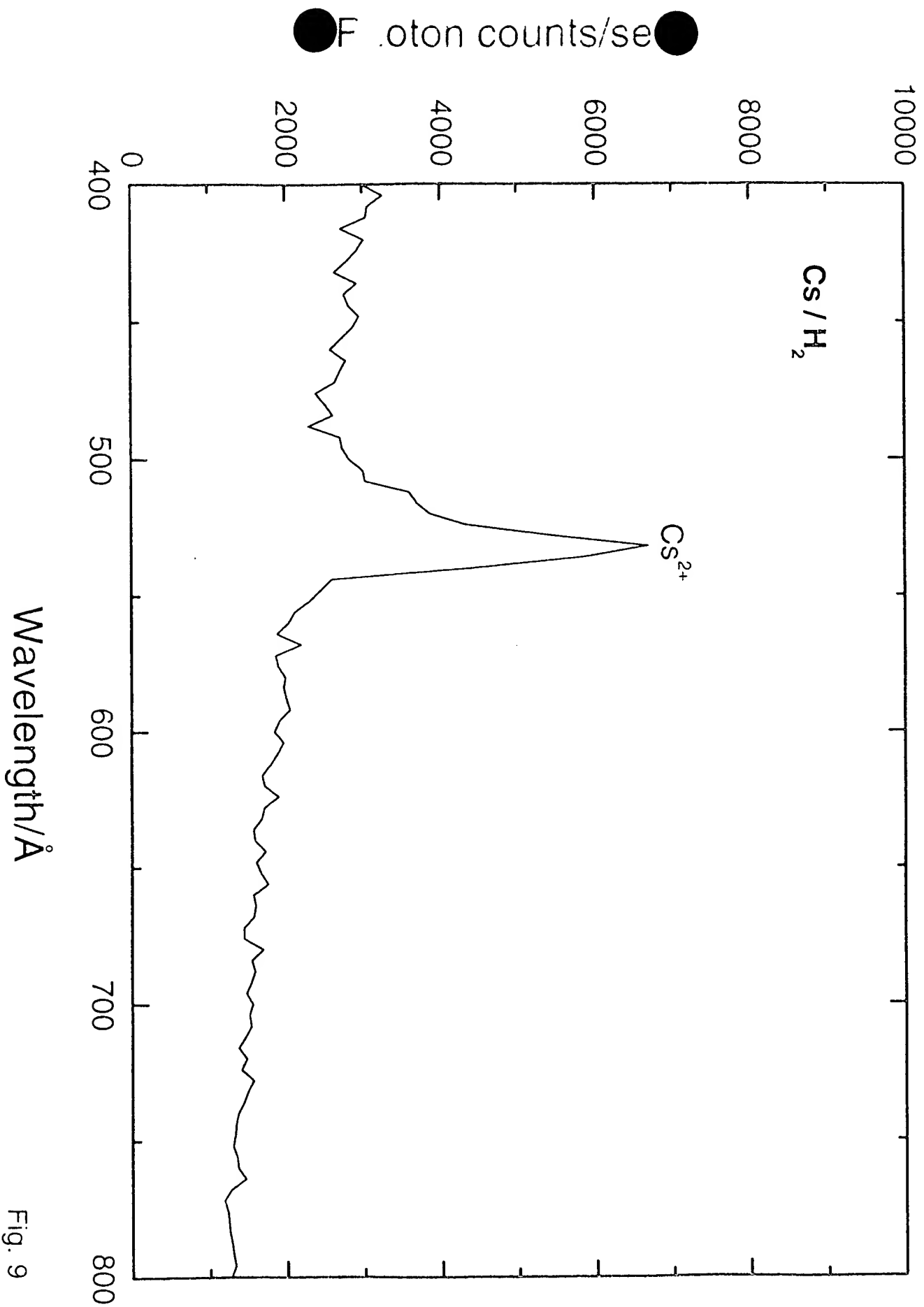
Fig. 9
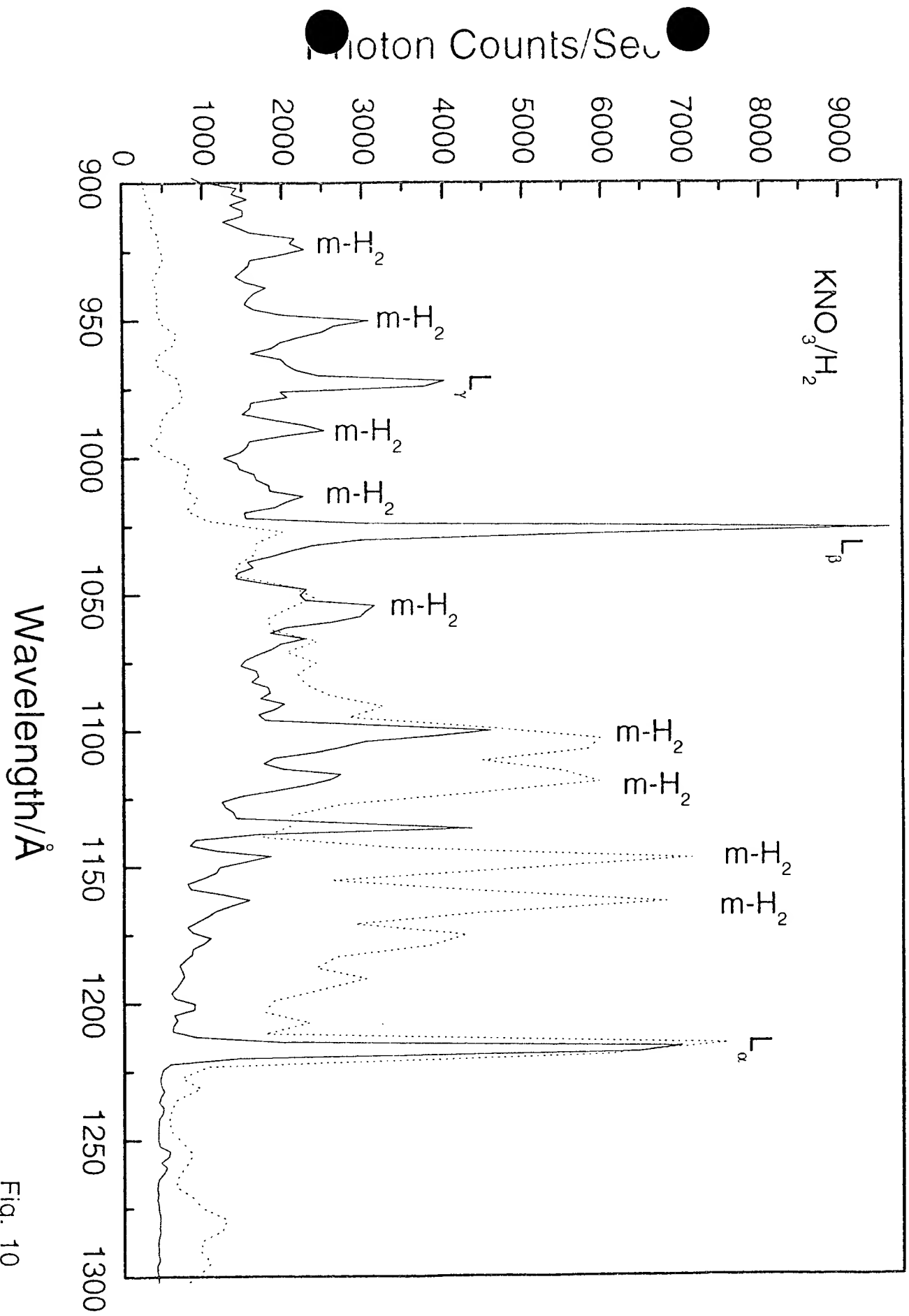
Fig. 10
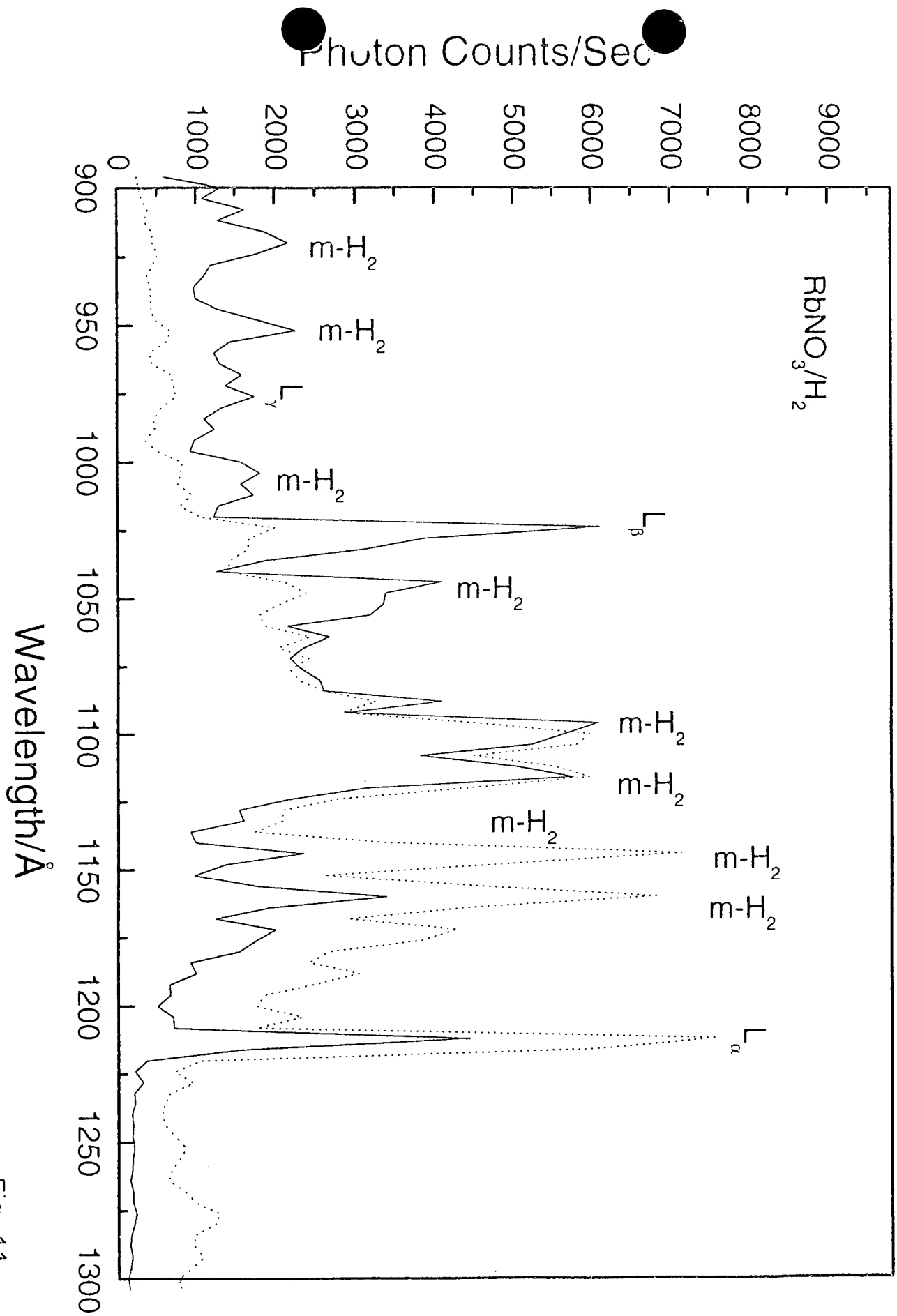
Fig. 11
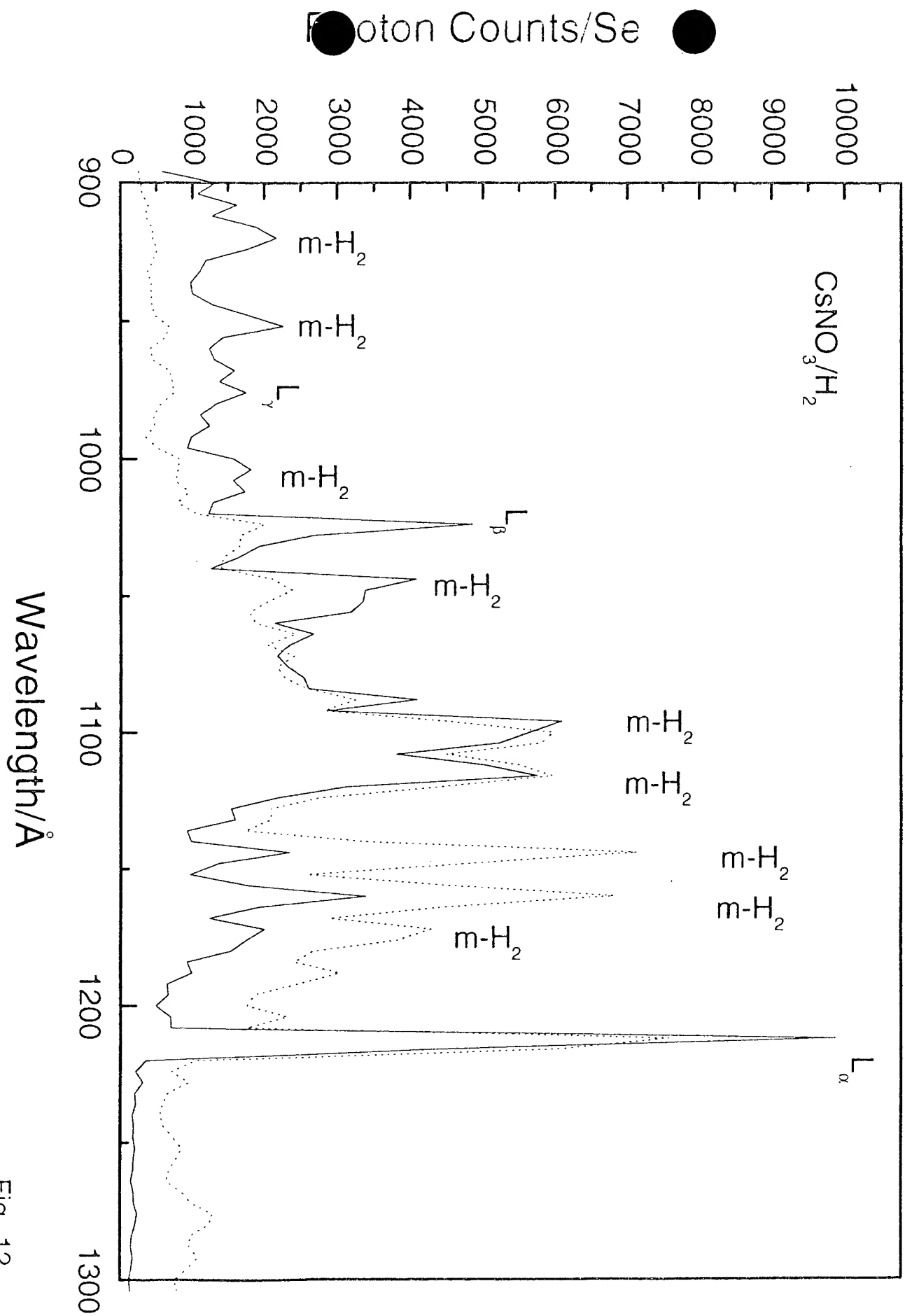
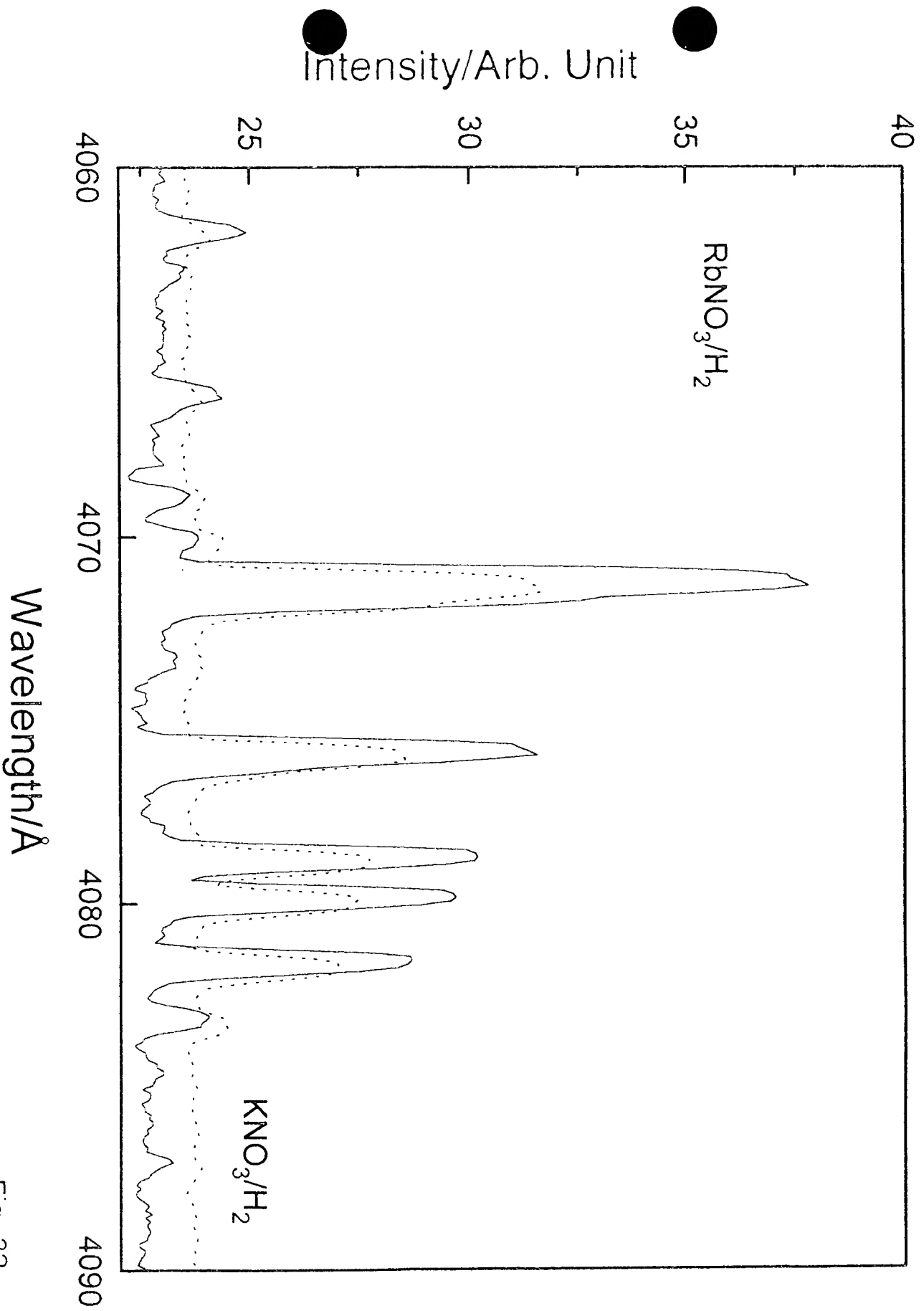Fig. 12
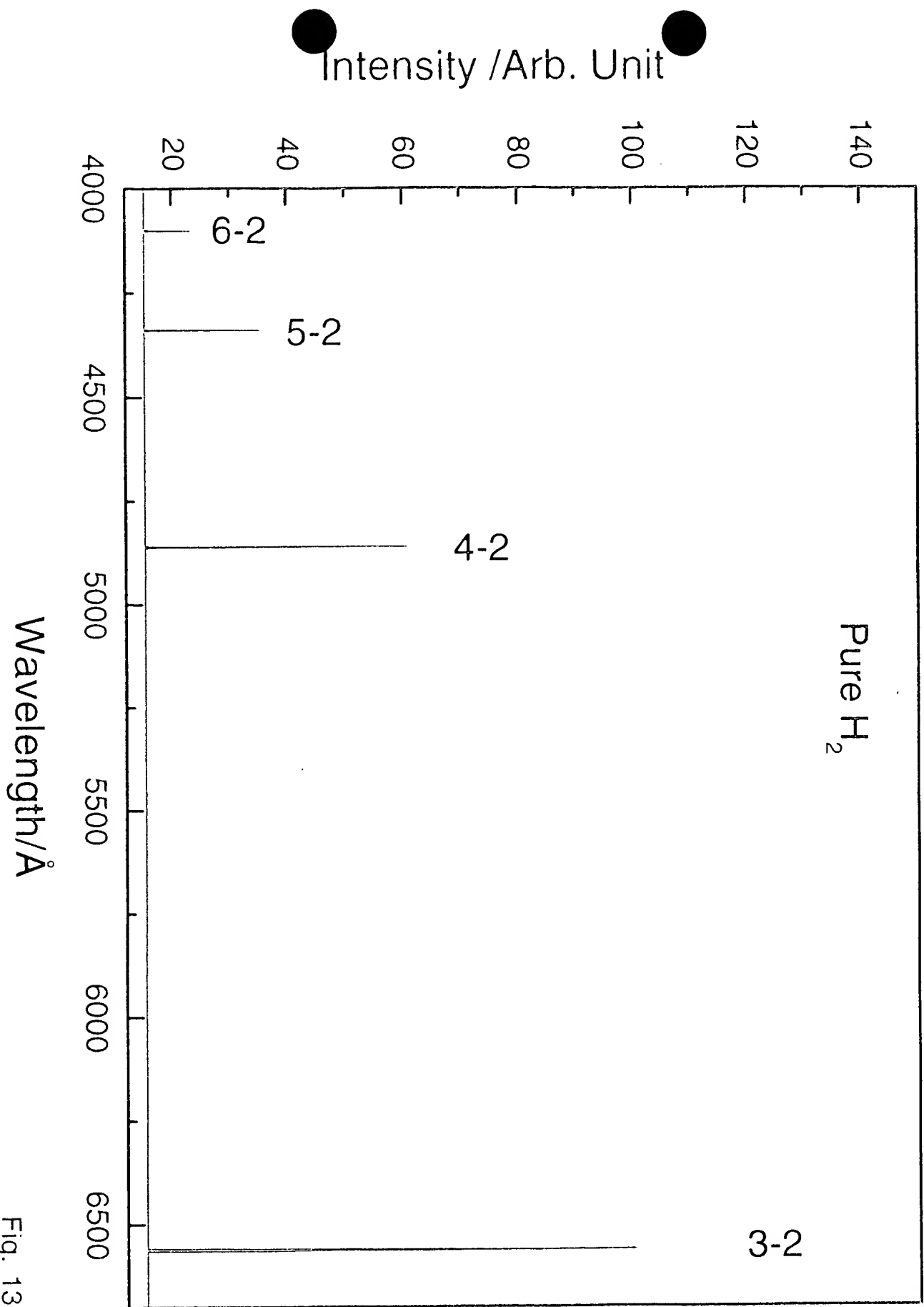
Fig. 13
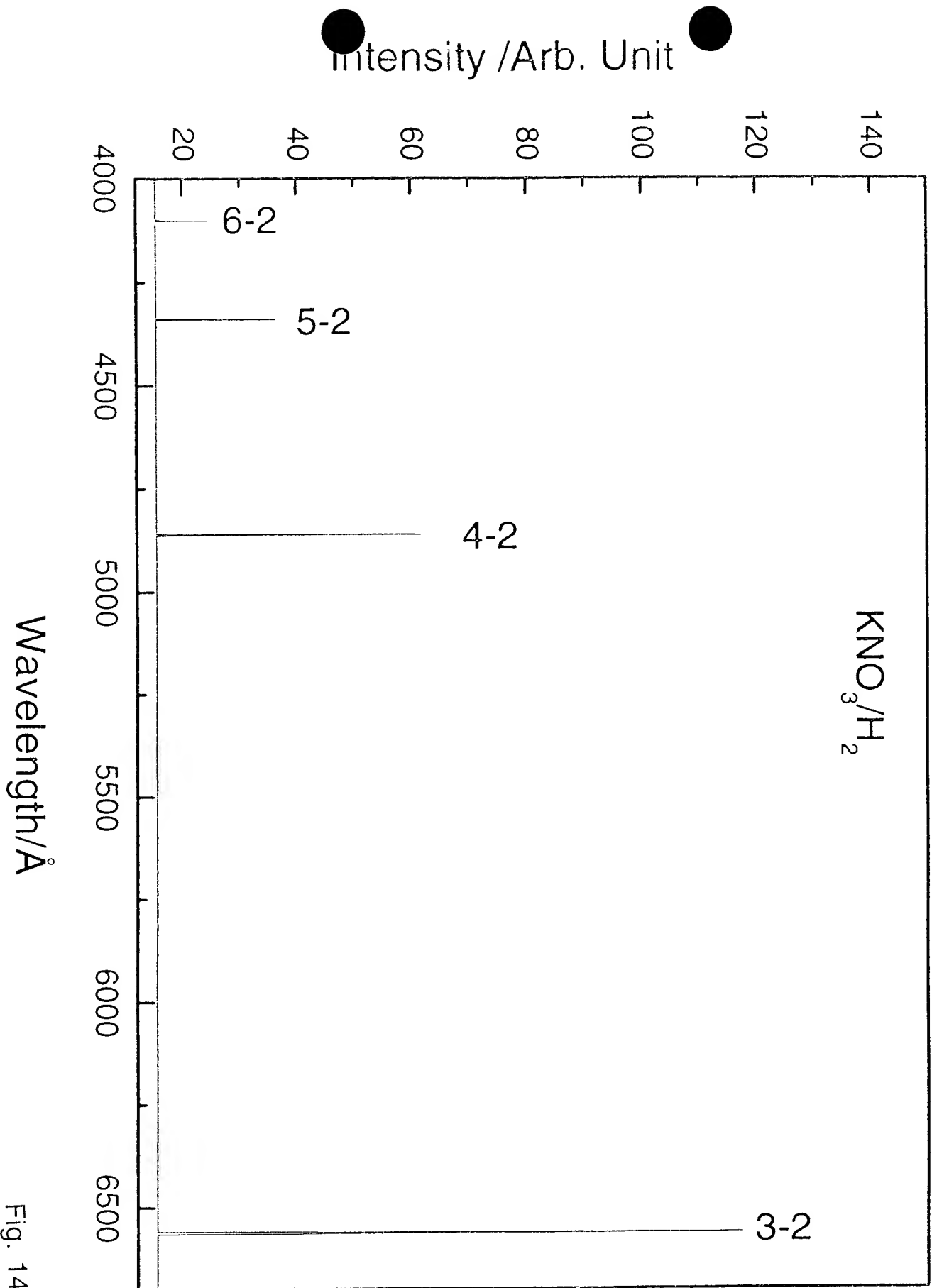
Fig. 14
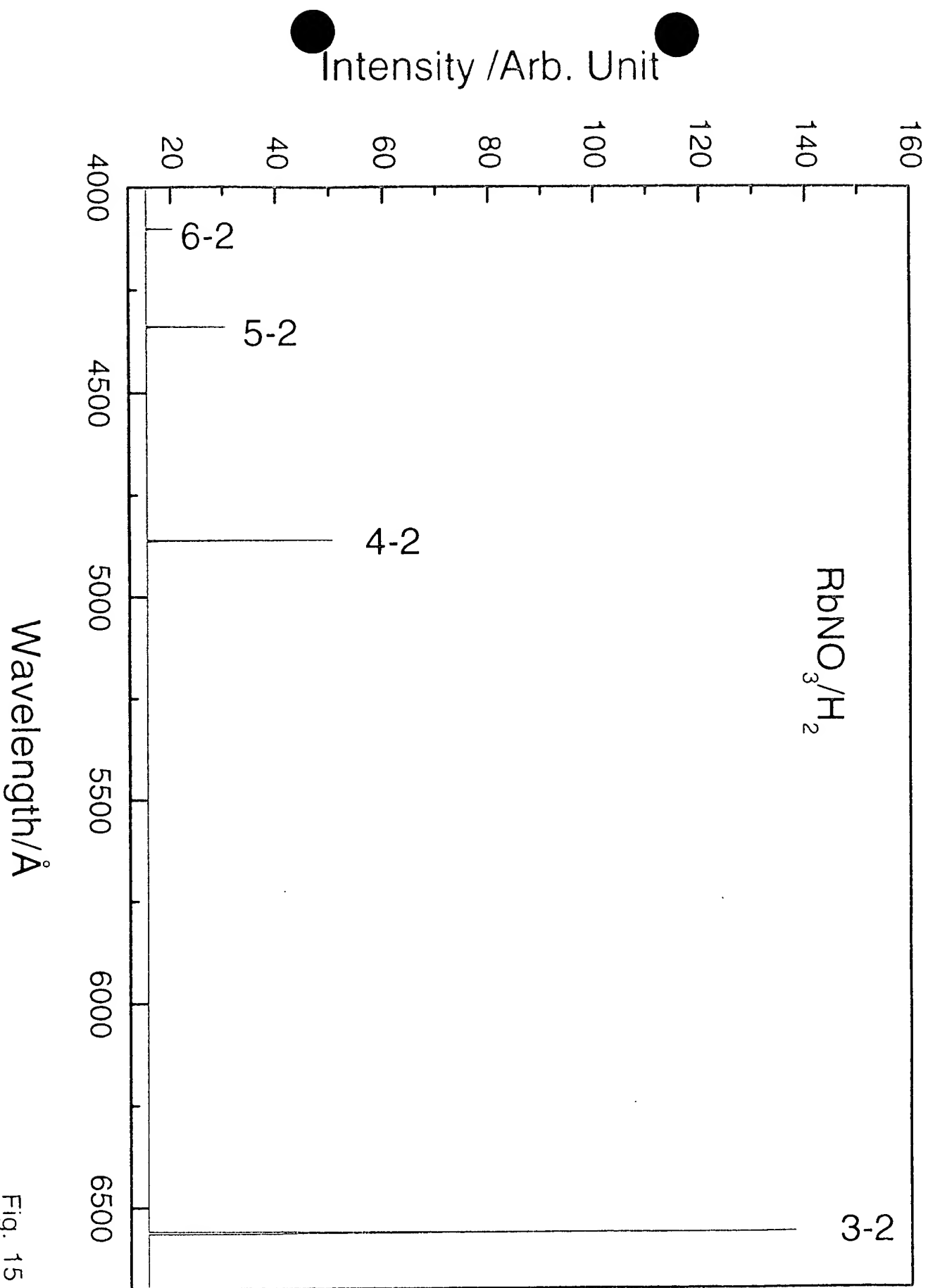
Fig. 15
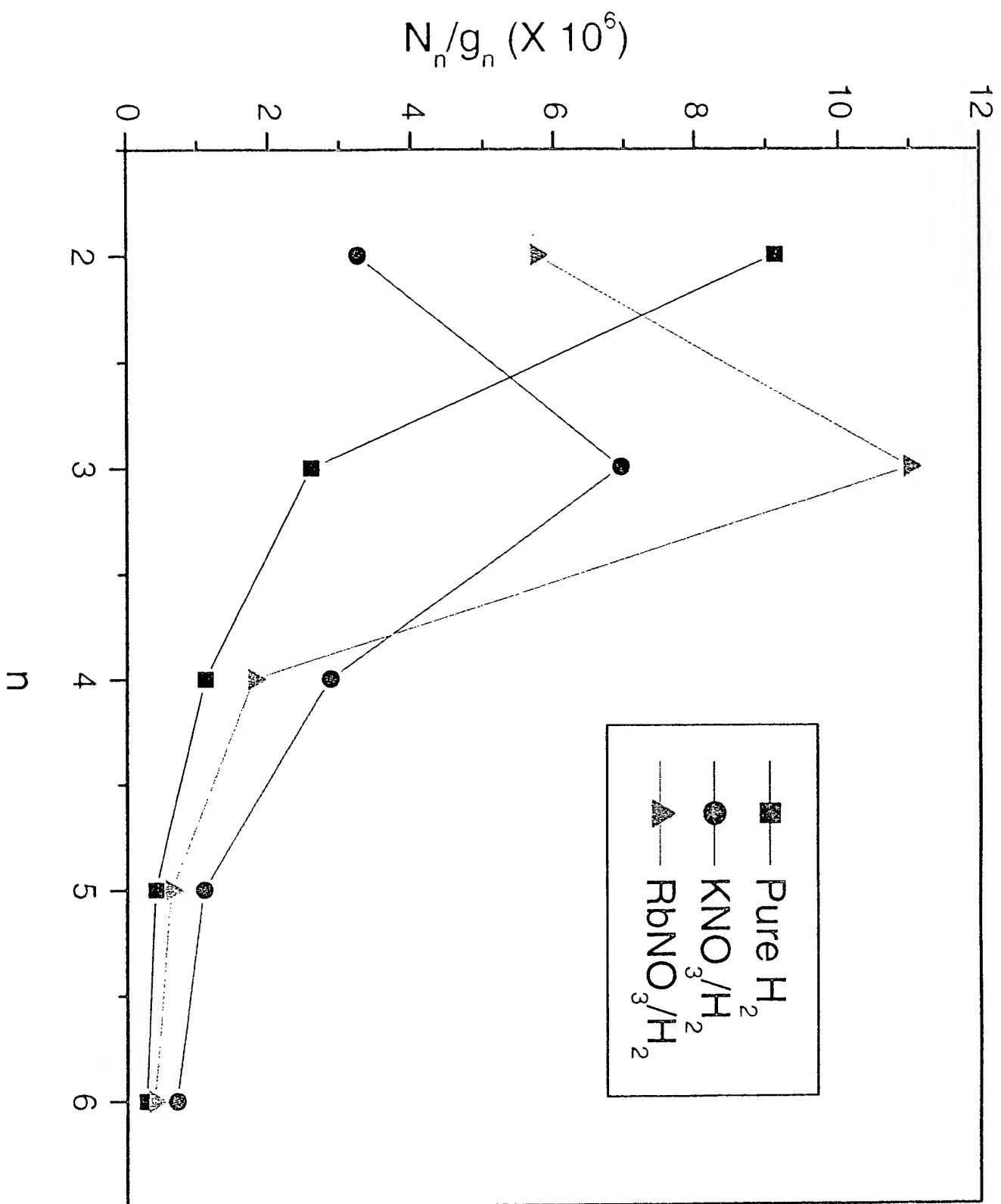
Fig. 16
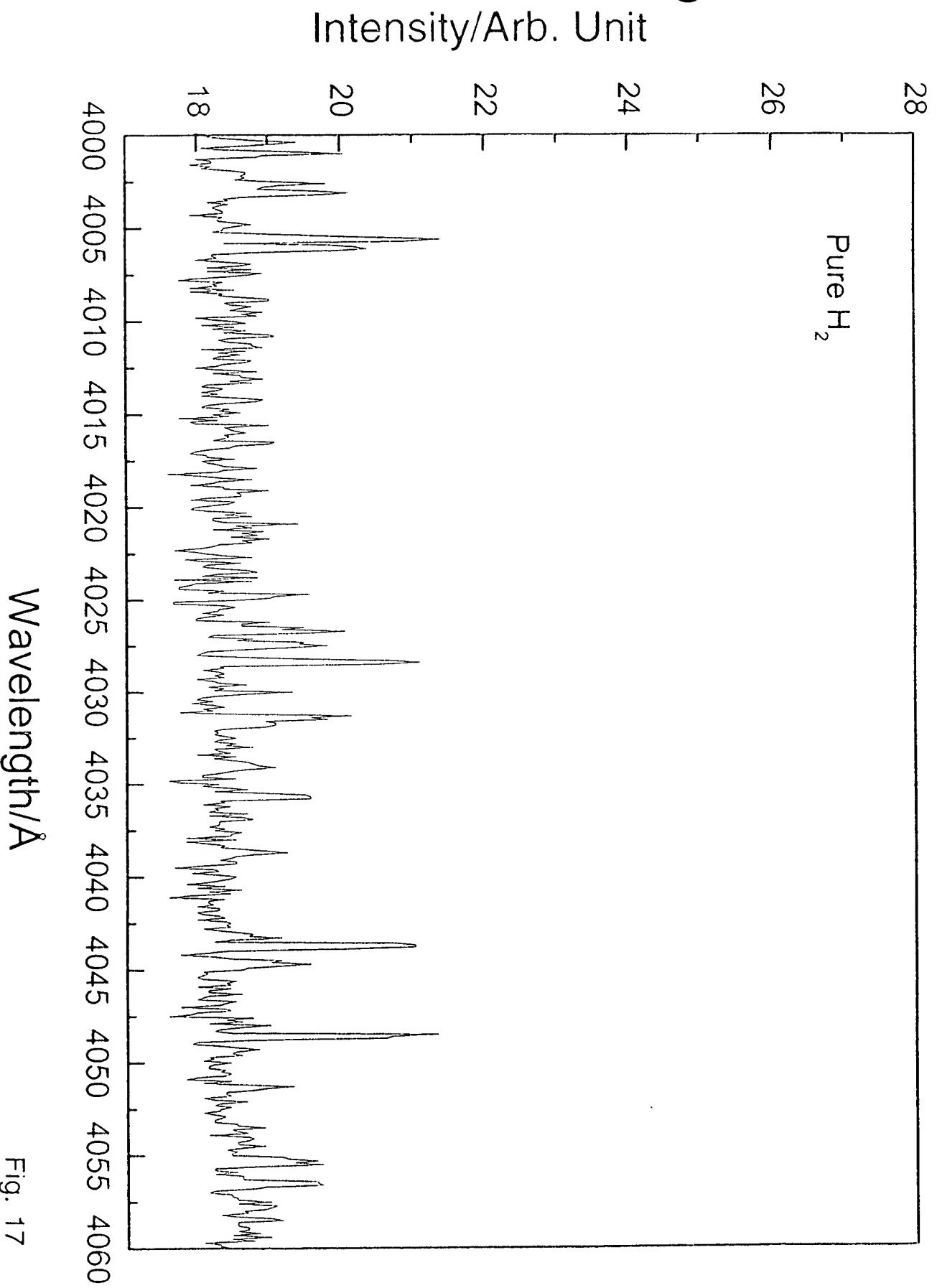
Fig. 17
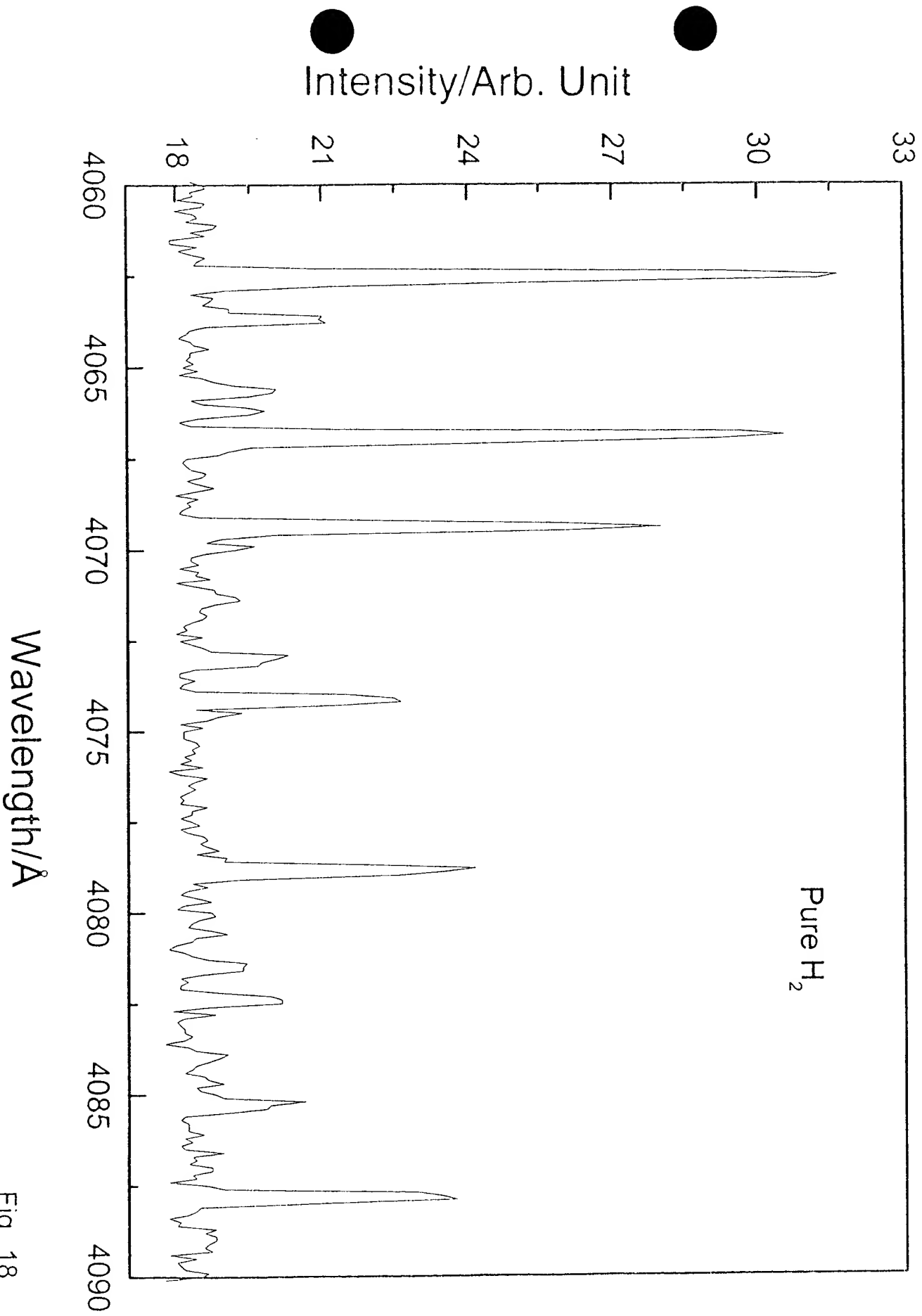
Fig. 18

Fig. 19

Fig. 20

Fig. 21

Fig. 22

Peak Positions:
4068.955 Å
4070.111 Å
4071.060 Å
4071.472 Å
4071.961 Å

Fig. 23

Fig. 24

Intensity/Arb. Unit

Wavelength/Å

KNO₃/H₂

Pure H₂

3E 2 - 2B 1
3E 2 - 2B 1
3 D2 - 2B 1
4D 0 - 2B 2
3D 2 - 2B 1
3E 2 - 2B 1
4D 0 - 2B 2
3D 2 - 2B 1
Z 2 - 2B 1
3D 2 - 2B 1
Z 2 - 2B 1
3D 2 - 2B 1
Z 2 - 2B 1

Fig. 25

Fig. 26

Fig. 27

Intensity/Arb. Unit

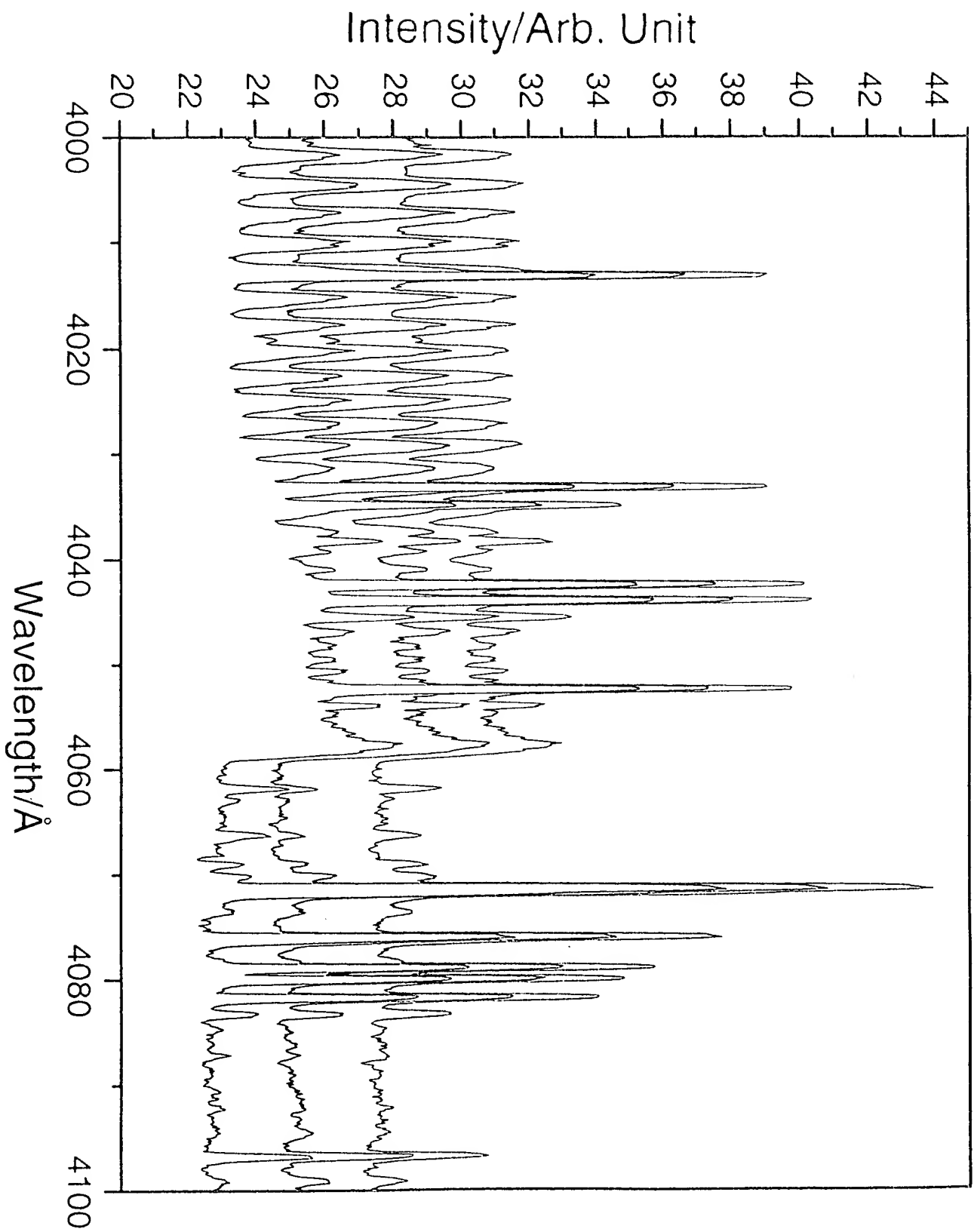Wavelength/Å

KNO_3/H_2

3996.3

K (4044.1)

K (4047.2)
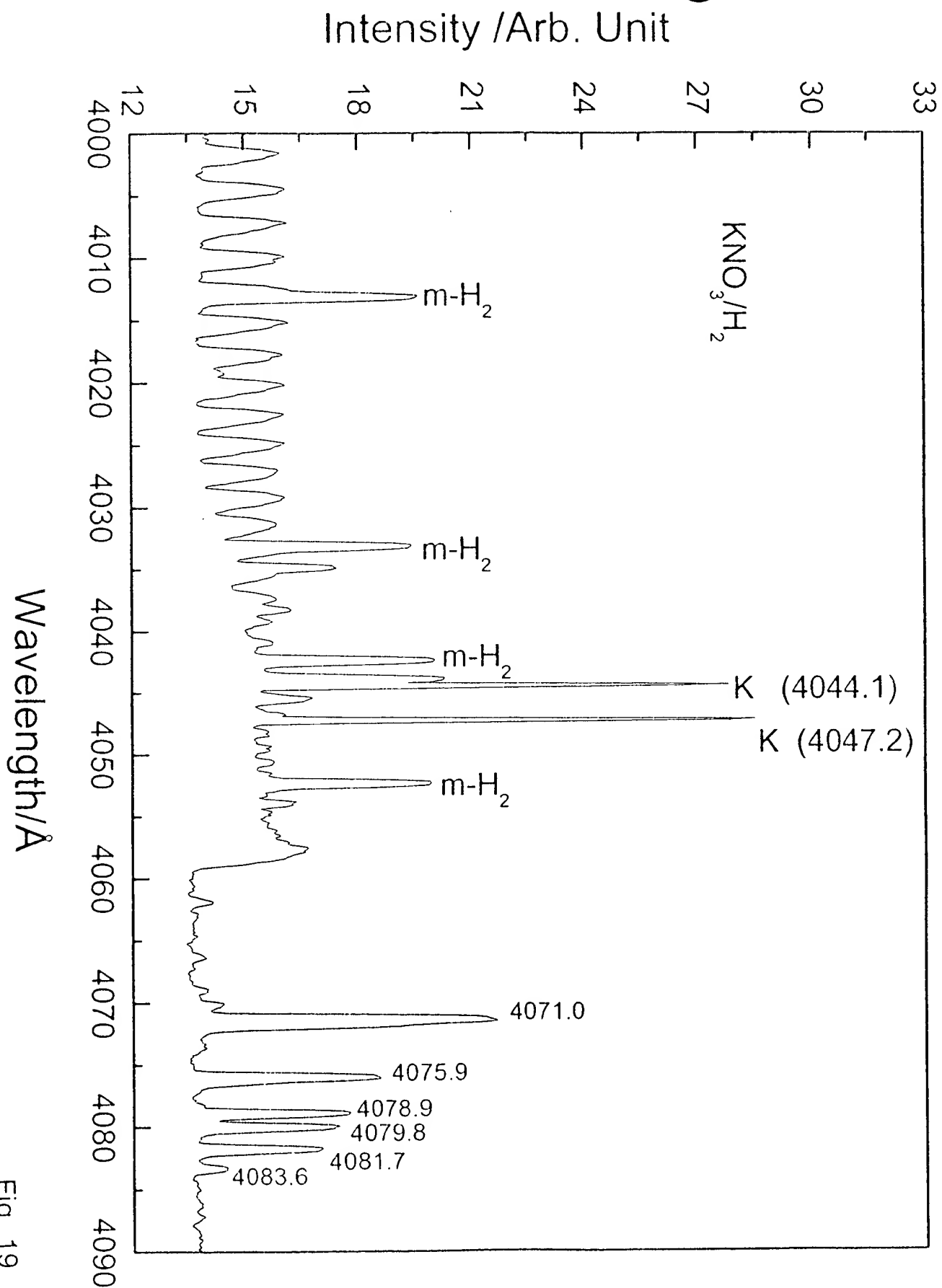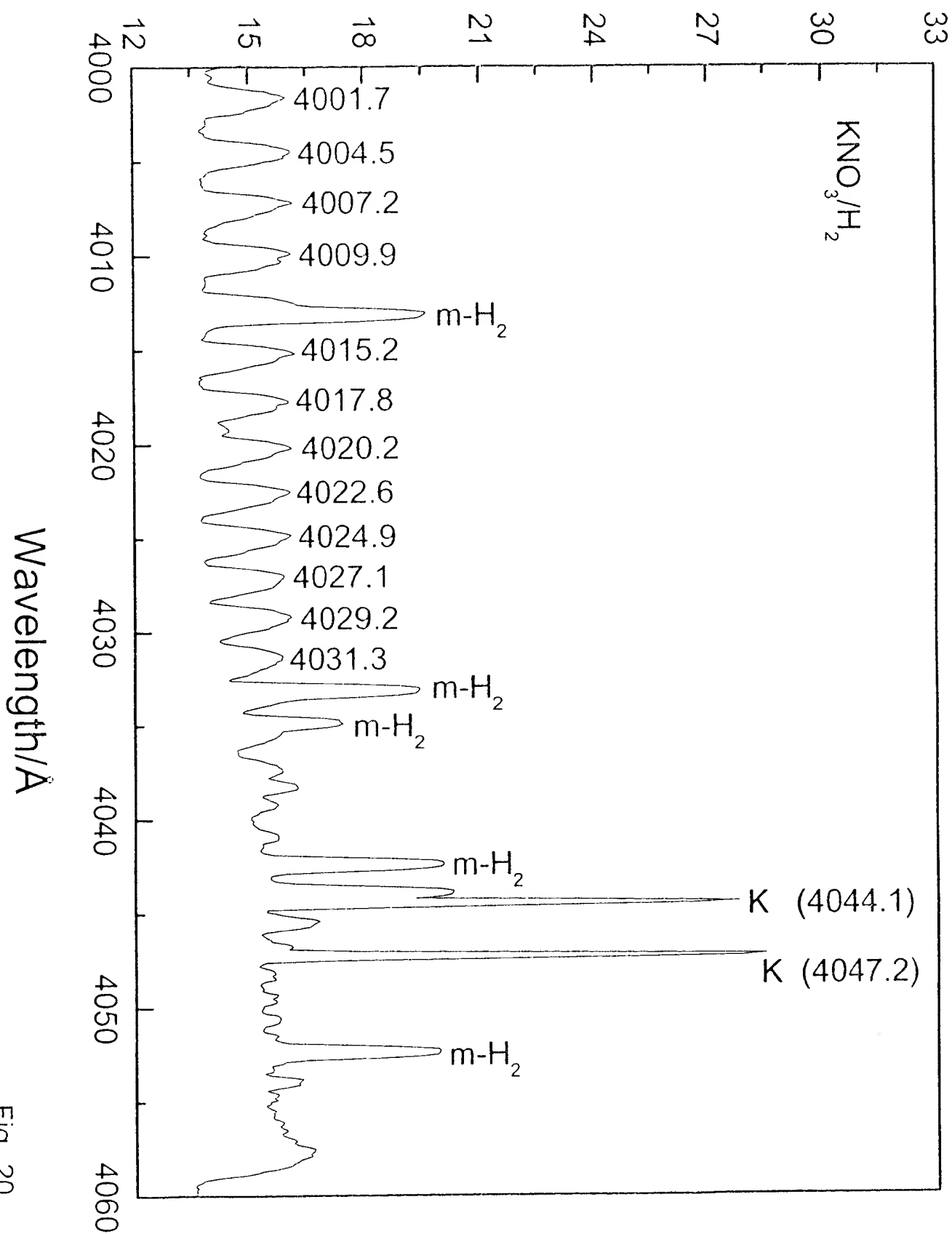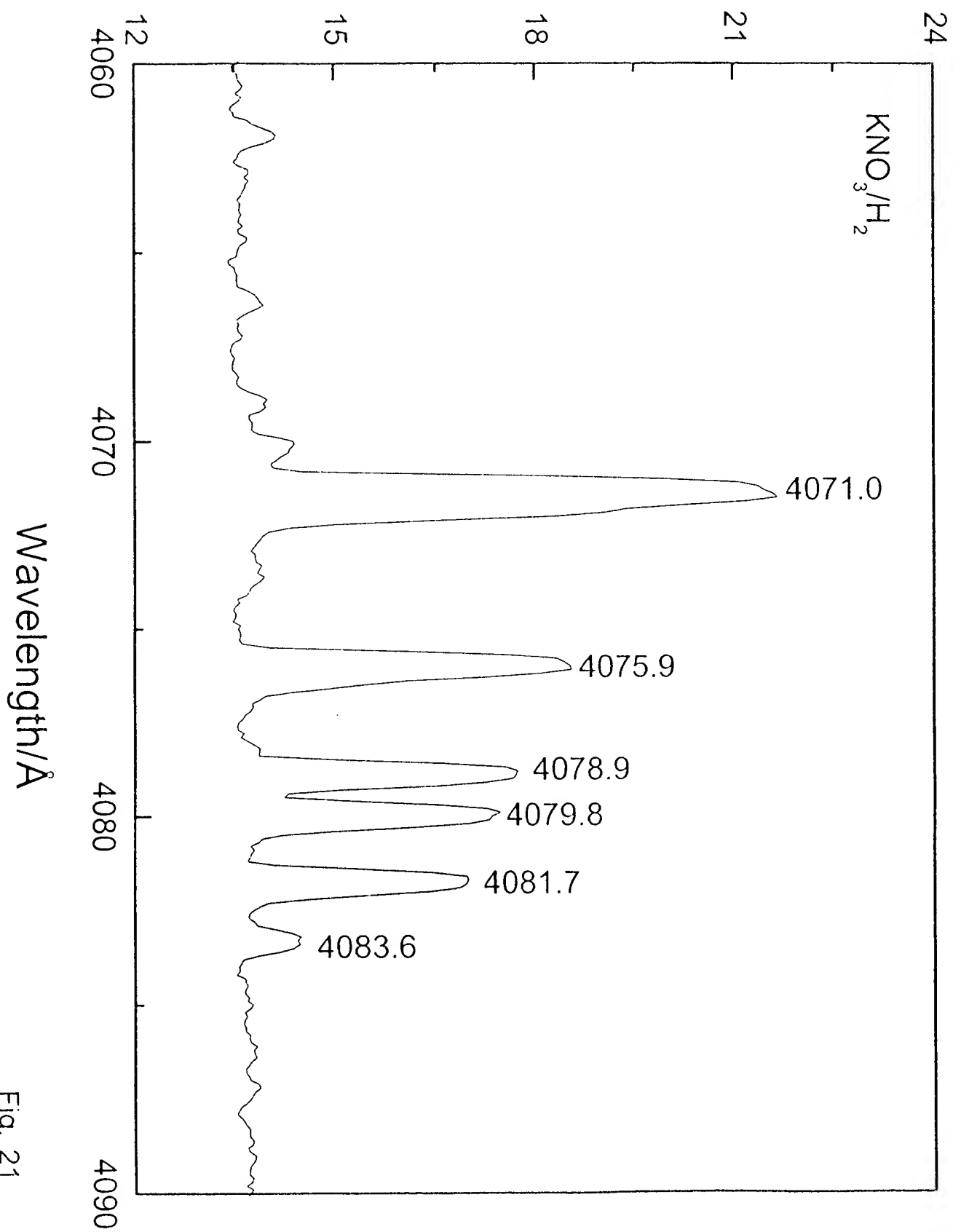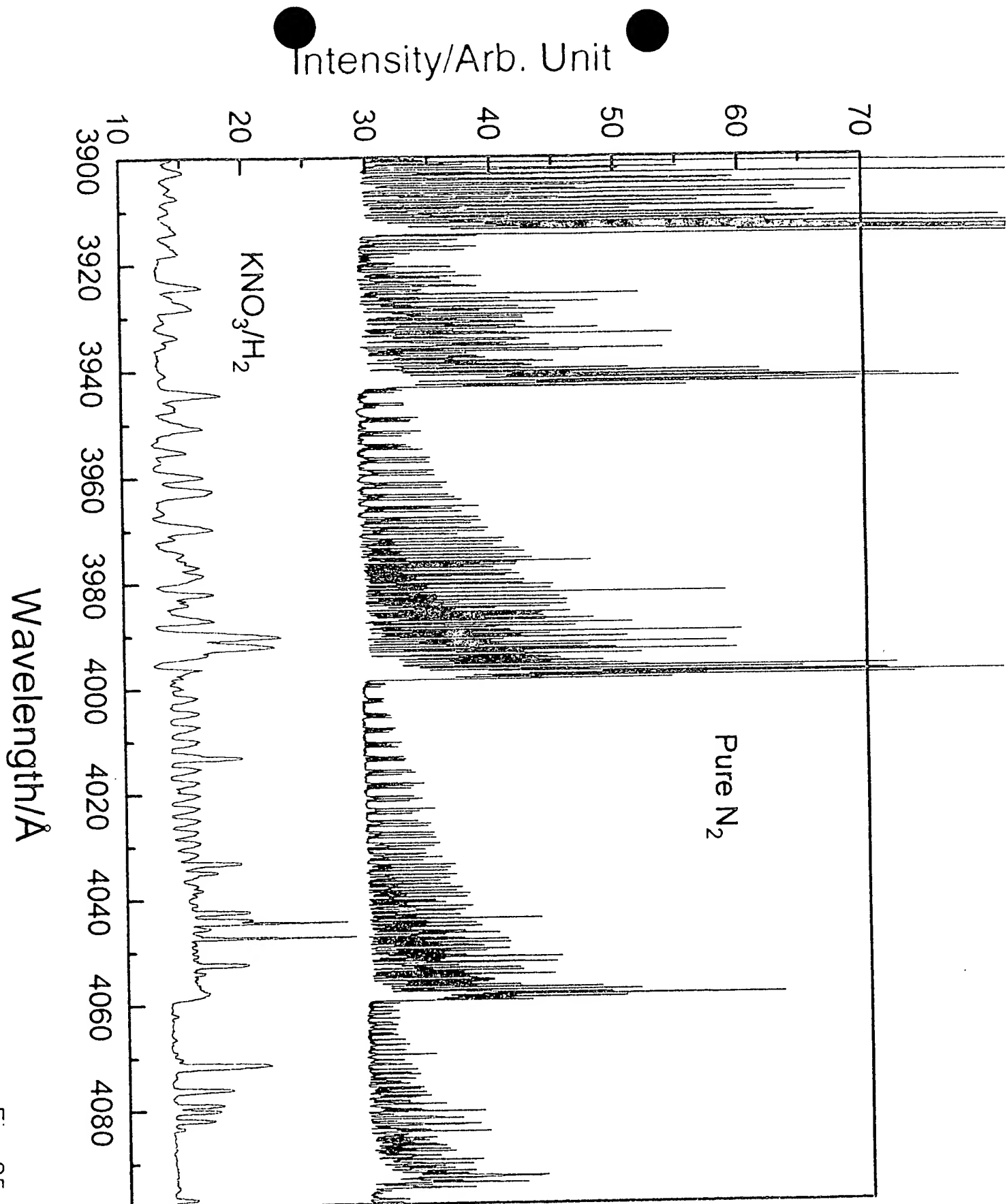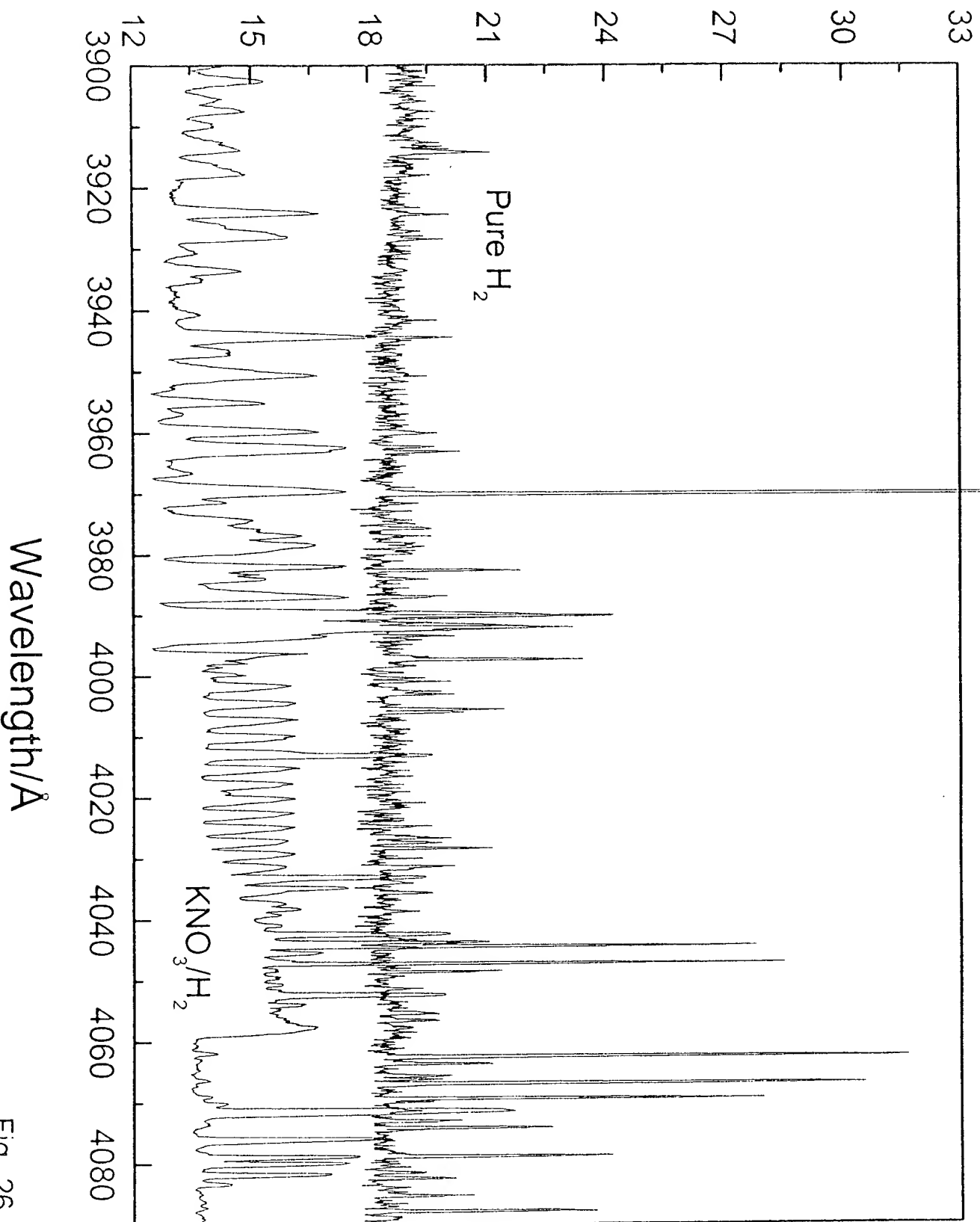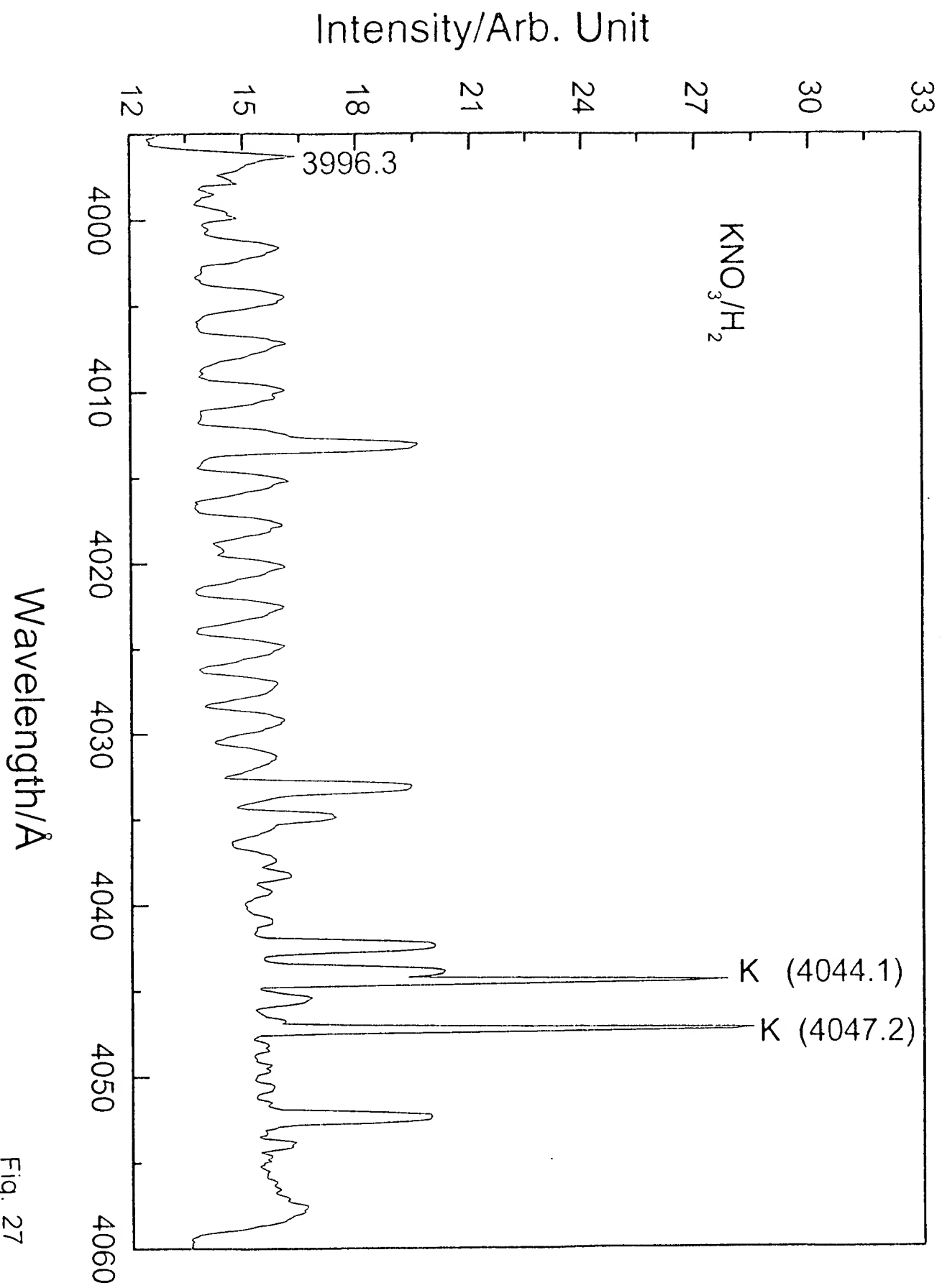
Fig. 28

Fig. 29

Fig. 30

Fig. 31

Fig. 32

Fig. 33

Fig. 34

Fig. 35

Fig. 36

RbNO$_3$/H$_2$

Chi^2	=	0.01241
R^2	=	0.99445

y0	23.44929
xc1	4009.76219
w1	0.67557
A1	2.6545
xc2	4010.22135
w2	0.239
A2	0.42925
xc3	4010.54543
w3	0.35272
A3	0.85694